Optimization-based Design and Analysis of Concentrating Solar Power with Thermochemical Energy Storage

By

Xinyue Peng

A dissertation submitted in partial fulfillment of
the requirements for the degree of

Doctor of Philosophy
(Chemical Engineering)

at the
UNIVERSITY OF WISCONSIN-MADISON
2019

Date of final oral examination: 10/21/2019

The dissertation is approved by the following members of the Final Oral Committee:

Christos T. Maravelias, Professor, Chemical and Biological Engineering
Thatcher W. Root, Professor, Chemical and Biological Engineering
Victor M. Zavala, Associate Professor, Chemical and Biological Engineering
Ross E. Swaney, Associate Professor, Chemical and Biological Engineering
Franklin K. Miller, Associate Professor, Mechanical Engineering

Abstract

Concentrating solar power (CSP) with thermal energy storage has the potential for grid-scale dispatchable power generation. Thermochemical energy storage (TCES), that is, the reversible conversion of solar-thermal energy to chemical energy, has high energy density and low heat loss over long periods. In this work, we develop optimization-based models for the design and analysis of CSP with different fluid-phase and solid-gas TCES systems. By proposing various TCES process strategies, evaluating their system performance, and identifying key areas of improvement, we hope that our study will help accelerate TCES development and solar power deployment.

Specifically, we first develop a general process model for CSP plants employing fluid-phase TCES systems. We illustrate our model applicability by using ammonia and methane TCES systems. The analysis allows us to identify pressure vessels for aboveground gas storage as the main cost driver and compressor electricity consumption as the main energy driver. The overall energetic and economic performance can be significantly improved if cheap underground gas storage is available.

We then propose an optimization-based framework for process synthesis under variability in two frequencies. We introduce scenarios and modes to represent low and high frequency variability respectively, and formulate the synthesis problem as a multimode two-stage stochastic programming model. The proposed approach is well suited to address the synthesis of renewable energy systems where the energy resource (e.g., solar, wind) often exhibits variability in two scales.

Next, we develop an optimization model for the design and operation of CSP plants employing solid-gas TCES systems. Special emphasis is placed on the modeling of fixed-bed reactors that operate in a cyclic batch mode, which are modeled using partial differential equations in time and space. Finally, we provide a system-level analysis for CSP employing various solid-gas TCES strategies, that is, different combinations of chemical reactions and process configurations. Six process configurations are proposed and three types (carbonate, hydroxide, and redox) of reactions are studied. Results show that, six out of the nine strategies have the potential to improve energy efficiency and reduce costs at the same time over two-tank molten salt storage. We also analyze the impacts of key reaction properties and process parameters on system performance.

Acknowledgment

This Ph.D. thesis would have been impossible without the generous help and support from many people in the past five years. First, I would like to express my sincere gratitude to my advisors, Professor Christos Maravelias and Thatcher Root, for guiding me through the Ph.D. journey and having a profound influence in my life. Christos has provided me with significant guidance on conducting research, presenting results, and most importantly, being a dedicated researcher. Thatcher has brought me many new ideas and useful challenges in our discussions, which teaches me to be a critical thinker. The experience of being co-advised has been immensely stimulating and I am grateful for the project opportunities I have had. Thanks to Dow Chemical Company and U.S. Department of Energy Great Lakes Bioenergy Research Center for their financial support.

Next, I want to thank my dissertation committee members, Professors Victor Zavala, Ross Swaney, and Franklin Miller, for their time reading my thesis, attending my defense, and more importantly, giving me valuable feedbacks.

Many thanks to former and current members of the Maravelias Group for creating an inclusive and learning-friendly environment. Special thanks to my peers and best friends Lingxun Kong, Ho Jae Lee and Shalaka Burlawar, who have been tremendously supportive and helpful along the way.

Lastly, I would like to thank my parents for their endless support and encouragement, which guides me through all the hard times. Their education has cultivated my personality and shaped who I am today. Specially, I would like to thank Xianyang for his patience, understanding, and unyielding love. Thank you for always being there when I need and creating lots of beautiful moments in my life. To our future journeys together, thank you.

Table of Content

List of Figures

List of Tables

Chapter 1

Introduction[1]

The 21st century has witnessed a growth of renewable energy as a green substitute for fossil-based electricity. Today, renewable sources account for 23% of the world electricity generation. Solar power, especially, maintains an annual growth of 51% in installed capacity for the last 10 years.[1] Solar energy serves as a clean and renewable energy source. However, the wider adoption of solar energy is considerably hindered by its intermittent, variable and uncertain nature.[2] Moreover, the mismatch between solar availability and electricity consumption (see **Figure 1-1**) leads to surplus solar electricity curtailments during the day and insufficient supply during the night. As a result, integrating solar power with grid-scale energy storage to enable dispatchable power generation is necessary in pursuit of a 100% renewable infrastructure.[3]

Concentrating solar power (CSP) integrated with thermal energy storage (TES) is considered to be a promising option to deliver cost effective renewable power while providing important attributes (i.e., dispatchability, reliability and stability) to the grid.[4–6] Today, more than 13GWh of TES in CSP are operational and most new CSP plants are incorporating TES.[7] According to IEA, under a high renewable energy scenario, 11% of electricity generation will come from CSP in 2050, with 954 GW of installed capacity.[8]

In this chapter, we provide a critical review of the CSP technology (**Section 1.1**), different types of TES (**Section 1.2**), and thermochemical energy storage (TCES) (**Section 1.3**), which is the reversible conversion of solar-thermal energy to chemical energy.

---

[1] The contents of this section appear in Peng, Root and Maravelias, *Green Chem*. **2017**

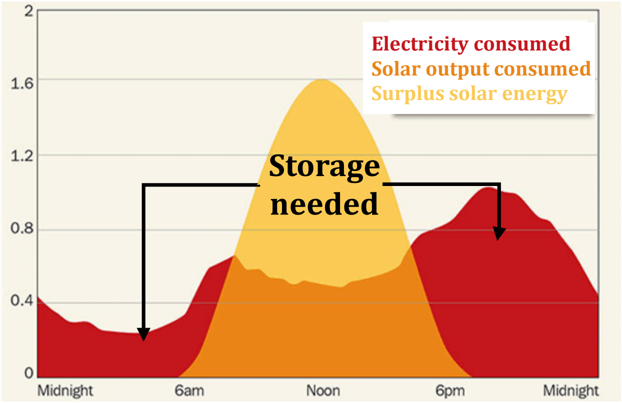

Figure 1-1. Electricity consumption and solar power production.[9]

1.1 CSP with thermal energy storage

Concentrating solar power is a renewable energy technology that has the capability of grid-scale dispatchable power generation. **Figure 1-2**A illustrates the working principle of a CSP plant: the collector focuses sunlight onto a receiver, where photons are absorbed and converted into heat. Part of the heat is delivered to a turbine for power generation while the other part is stored in a thermal energy storage system for night use. Two common types of commercial CSP plants[10], classified by collector configurations, are the "line-focused" parabolic trough (**Figure 1-2**B) and the "point-focused" power tower (**Figure 1-2**C).

Using heat or chemical as an intermediate, rather than converting sunlight directly to electricity as is done in photovoltaics (PV), provides CSP the opportunity to incorporate simple, efficient and low cost TES.[11] A typical TES system in a CSP plant costs around $75/kW with a round-trip efficiency of 98%, compared to $300/kW and 75% efficiency[12] that can be achieved using batteries for electricity storage in a PV plant. Therefore, although PV is more cost-effective than CSP for electricity generation, CSP with TES systems remain cheaper than PV with battery systems for solar power generation requiring more than 6 hours of storage.[13] Today, TES systems are utility scale and operating all around the world.[14] **Figure 1-2**C is Crescent Dunes, a 110 MW CSP plant in Nevada, USA, which became operational in 2015[15]. Crescent Dunes is coupled with 10-hour full load two-tank molten salt TES (1.1 GWh), which is comparable to the total capacity of batteries connected to the grid (1.5 GWh).[14]

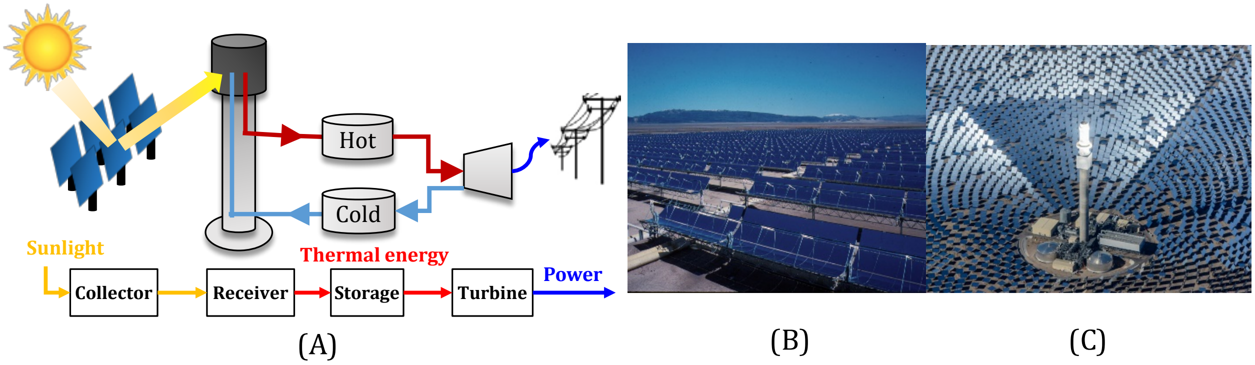

Figure 1-2. CSP plants with TES systems. (A) Schematic diagram (B) SEGS, a 354 MW parabolic trough plant in California, USA[16] (C) Crescent Dunes, a 110 MW power tower plant in Nevada, USA.[15]

1.2 Thermal energy storage

TES systems for CSP can be classified into three types: sensible heat storage, latent heat storage and thermochemical energy storage. The characteristics of each type are given in **Table 1-1**. Sensible heat storage is the simplest system. The only TES for CSP in operation today is the two-tank molten salt system, where one tank stores heated high-temperature salts coming from the receiver and the other tank holds the cooled down salt after turbine steam generation. A limitation of the current two-tank system is that molten salts decompose above 600℃ and freeze below 200℃, which leads to low turbine efficiency and needs auxiliary heating to prevent freezing during night.

An alternative option is latent heat storage which has the advantage of isothermal operation. This method, however, suffers from poor heat transfer and low exergetic efficiency. Finally, thermochemical energy storage (TCES), which stores and releases energy by breaking and reforming chemical bonds, has the advantages of higher energy density, operation over a wider temperature range, and longer storage periods. These desirable features make TCES, potentially, a better fit for the next generation CSP plants, where plant efficiency is improved through the use of high operating temperatures and more advanced power cycles (e.g., supercritical CO_2 cycle).[17] However, compared to other forms of TES, TCES is still at an early stage of development due to its system complexity.

Table 1-1. Comparison of three types of TES systems.

	Sensible storage	Latent heat storage	Thermochemical energy storage
Example system	Molten salt	$NaNO_3$	$CH_4 + H_2O \leftrightarrow CO + 3H_2$
Energy density	0.11 kWh/kg	0.05 kWh/kg	2.04 kWh/kg
Temperature range	265-565℃	306℃	20-1000℃
Storage period	Limited	Limited	Theoretically unlimited
Complexity	Simple	Medium	Complex
Maturity	Commercial	Pilot scale	Mainly lab scale

1.3 Thermochemical energy storage

An important consideration for TCES system is the selection of the reversible reaction. Important selection criteria include suitable reaction turning temperature, large reaction enthalpy (ΔH), and reversibility.[18] The concept of turning temperature (T*), defined as the temperature at which the reaction equilibrium constant K equals to 1, is useful for quick screening of reactions in the desired temperature range (ideally 500-1000℃ for high turbine efficiency). Previously, several reaction types have been studied as candidates, including dissociation of ammonia, hydrides, carbonates, oxides, hydroxides and methane reforming. **Table 1-2** is a summary of reversible reactions studied for TCES systems.[19,20]

Among these types, fluid-phase TCES systems based on ammonia synthesis[21] and methane reforming[22] have been investigated for 40 years and reached prototype status. However, our analyses in **Chapter 2** for fluid-phase TCES systems show that they suffer from low energy efficiency and high costs due to the need to store large amount of reaction gas. Recently, solid-gas reactions have started to receive more attention because they require less gas storage, have higher reaction temperature and easier product separation.[23,24] Thus, in **Chapter 4 and 5**, we focus our study on solid-gas TCES, which we review in more detail below.

Table 1-2. Summary of reversible reactions for TCES systems.

Phase	Reaction types	Example	Energy density		T^* (℃)	Advantages	Disadvantages
			kWh /kg	kWh /m^{3*}			
Fluid phase	Ammonia	$NH_3 \leftrightarrow 0.5N_2 + 1.5H_2$	1.09	745 (l)	200	Liquid NH_3 for storage	Low T^*
	Methane	$CH_4 + H_2O \leftrightarrow CO + 3H_2$	2.04	7.8 (g)	700	High ΔH	Side reaction
Solid-gas phase	Metal hydride	$MgH_2 \leftrightarrow Mg + H_2$	0.80	580 (s)	302	Good reversibility	Slow kinetics
	Carbonate	$CaCO_3 \leftrightarrow CaO + CO_2$	0.49	692 (s)	860	Cheap material	Poor reversibility
	Hydroxide	$Ca(OH)_2 \leftrightarrow CaO + H_2O$	0.39	437 (s)	525	No catalyst	Sintering, low conductivity
	Oxide	$Co_3O_4 \leftrightarrow 3CoO + 0.5O_2$	0.24	295 (s)	935	Good reversibility	Costly & toxic

* Energy density based on the volume of specific reactant phase: l: liquid; g: gas; s: solid;

Research on solid-gas TCES systems has focused on three different areas: (1) reaction studies, (2) reactor studies and (3) system-level studies. In **Table 1-3**, we summarize previous studies on three types (carbonate, hydroxide and redox types) of TCES systems. For convenience, each solid-gas reaction $A\ (s) \longleftrightarrow B\ (s) + C\ (g)$ is referred to as A/B hereinafter. While this work focuses on system-level studies, we review each of the three research areas in the following subsections.

Table 1-3. Reaction candidates and previous works on three types of solid-gas TCES systems.

Type	Candidates	Reaction studies	Reactor studies	System-level studies
Carbonate	$CaCO_3/CaO$ $SrCO_3/SrO$ $MgCO_3/MgO$	Thermodynamics[25] Kinetics[26,27] Stability[25,28–30]	Fixed bed[31] Rotary kiln[32–34] Fluidized bed[35] Cyclone[36,37]	Process design[38–41] Techno-economic[42]
Hydroxide	$Ca(OH)_2/CaO$ $Ba(OH)_2/BaO$ $Sr(OH)_2/SrO$	Thermodynamics[43] Kinetics[43,44] Stability[45,46] Screening[47]	Fixed bed[48–51] Moving bed[52] Fluidized bed[53–56]	Thermodynamic analysis[57] Process design[58,59] Techno-economic[42,60,61]
Redox	BaO_2/BaO Co_3O_4/CoO Mn_2O_3/Mn_3O_4 Perovskites	Thermodynamics[62–65] Kinetics[62,66] Stability[66–68] Screening[69]	Honeycomb[70–72] Rotary kiln [73,74] Moving bed[75]	Thermodynamic analysis[76,77] Techno-economic[42,78]

1.3.1 Reaction studies

Reaction studies include identifying suitable reversible reactions and studying their thermodynamics, kinetics and cycling stability.

Carbonate system

The general form of a carbonate reaction is:

$$M_x(CO_3)_y\ (s) \leftrightarrow M_xO_y\ (s) + y\ CO_2\ (g)$$

Many carbonate reactions have been studied for CO_2 capture.[79–81] In the context of CSP-TCES, $CaCO_3/CaO$ is the most investigated one due to its high operating temperature (885 ℃ at 1 bar CO_2 partial pressure), high energy storage capacity (692 kWh/m[3] $CaCO_3$) as well as the abundant and cheap limestone feedstock.[38] However, CaO particles progressively deactive to ~20% over repeated cycles due to sintering.[82] The material stability can be enhanced by using calcium and magnesium acetate as CaO precursors.[30] $SrCO_3/SrO$ has also been studied for TCES because it offers the ability to store and release energy at higher temperature (~1200 ℃).[83] Carbonation conversion of SrO remains stable over the first 15 cycles and then decreases to 87% over 45 cycles. $MgCO_3/MgO$ has also been widely studied but mainly for applications at lower temperature (e.g.,

Hydroxide system

The general form of a hydroxide reaction is:

$$M_x(OH)_y\ (s) \leftrightarrow M_xO_{y/2}\ (s) + y/2\ H_2O\ (g)$$

The hydroxide reactions proposed for TCES systems are $Ca(OH)_2/CaO$, $Ba(OH)_2/BaO$, and $Sr(OH)_2/SrO$ reactions. Among them, $Ca(OH)_2/CaO$ reaction receives the most attention due to its high reaction enthalpy as well as the abundancy and low cost of $Ca(OH)_2$. However, $Ca(OH)_2$ materials have poor mechanical properties that may lead to attrition and agglomeration over reaction cycles.[46] Several material modifications have been proposed to enhance its mechanically stability, including adding nanoparticles[45] and synthesizing composite material[46].

Redox system

The general form of a redox reaction is:

$$M_xO_y\ (s) \leftrightarrow M_xO_z\ (s) + (y-z)/2\ O_2\ (g)$$

In order to search candidates for redox TCES systems, Wong et al.[69] screened 74 pure metal oxides based on thermodynamic calculations and identified 6 suitable redox reactions. In particular, Co_3O_4/CoO,BaO_2/BaO and Mn_2O_3/Mn_3O_4 reactions are thermodynamically favorable at 700-1000°C temperature range and found to be the most attractive candidates for TCES.

Co_3O_4/CoO has high reaction enthalpy and long-term cyclic stability.[84] The material remains stable over 500 cycles.[73] Mn_2O_3 and BaO_2 have been studied because they have lower material cost and toxicity than Co_3O_4. Carillo et al.[66] tested the Mn_2O_3/Mn_3O_4 over 30 oxidation-reduction cycles and found that the particle size had dramatic influence on the material cyclabililty. The feasibility of using $\mathrm{BaO_2/BaO}$ for TCES has been demonstrated by Fahim and Ford[62], but more work needs to be done to improve the cycling stability of this system. Beyond pure oxides, mixed oxides and perovskites ($\mathrm{ABO_3/ABO_{3-\delta}}$) were recently investigated as promising high temperature TCES candidates due to their potential to increase oxygen exchange capabilities.[64,78]

1.3.2 Reactor studies

Different solar reactors have been developed for solid-gas TCES systems and tested at laboratory/pilot scale. These reactors can be classified into stacked, fluidized and entrained reactors based on the reactor flow pattern.[85,86] Stacked reactors can be further classified into fixed bed, rotary kiln and moving bed. The advantages and disadvantages of each reactor type are summarized in Table 2. Fixed-bed reactors are easy to design, construct and operate but typically have slow heat transfer due to low thermal conductivity of porous bed.[51,87] The other two types of stacked reactors, rotary kiln and moving bed, enhance the heat transfer by rotating the reactor or moving the bed, at the cost of higher parasitic energy consumptions. Fluidized beds keep reacting particles in suspension, which increases gas-solid contact and particle residence time, but at the same time, also leads to high pressure drop and erosion of reactor vessels. Finally, cyclone reactors are worth considering if further separation between solid and gas is needed.[85]

Table 1-4 summarizes the solar reactors that have been experimentally tested for the three types of solid-gas reactions. Carbonate reactions have been implemented in fixed beds[31], rotary kilns[32–34], fluidized beds[35], and cyclone reactors[36,37]. Hydroxide reactions have been implemented in fixed bed[48–51], moving bed[52] , and fluidized beds[53–56]. Redox reactions have been implemented in powder-coated honeycomb reactors[70–72], rotary kilns[73,74], and moving beds[75]. Among all 68 reported solid-gas solar reactors, fixed bed is the most frequently adopted reactor type (50%), followed by fluidized bed (21%) and rotary kiln (15%).[88]

Table 1-4. Comparison among different types of solid-gas solar reactors.

Type	Reactor	Advantage	Disadvantage
Stacked	Fixed bed	Low cost, low parasitic energy Easy design, construction and operation, extensively studied	Slow heat and mass transfer Difficult to be implemented for continuous commercial process
	Rotary kiln	Fast heat and mass transfer Versatility, long life components	Difficult to be scaled up High parasitic energy demand
	Moving bed	Direct heat transfer High heat transfer coefficient	Non-uniform irradiance distribution Need to control the residence time
Fluidized	Fluidized bed	Minimize hot spots and thermal instability; fast heat transfer	High pressure drop and parasitic energy Complex reactor hydrodynamics, erosion
Entrained	Cyclone	Continuously feed and separate solid and gas products	Solid deposition on the reactor walls Reactor window eroded by solids

1.3.3 System-level studies

System-level studies include energy/exergy analysis, process design, and techno-economic analysis. **Table 1-5** summarizes 12 system-level studies available in the literature for solid-gas TCES systems. We observe that all previous works have at least one of the following limitations:

(1) Assumed ideal reactors which always reach thermodynamic equilibrium. However, neglecting the kinetics or heat transfer limitations, especially in fixed-bed reactors, may lead to unrealistic reactor designs and underestimated reactor costs.

(2) Studied the system performance based on one (e.g., annual average) solar condition. However, in real operation, CSP plants are subject to variability in solar irradiance.

(3) Assessed the plant performance solely based on energy efficiency, that is, did not analyze economic feasibility.

Table 1-5. Summary of system-level studies on solid-gas TCES in the literature.

Ref.	TCES reaction	Scope	Reaction kinetics	Power cycle	Energy analysis	Cost analysis	Design optimization	Solar seasonal variability
27	$CaCO_3/CaO$	CSP	Yes	CO_2 Brayton	Yes	No	No	No
40	$CaCO_3/CaO$	CSP	No	Steam Rankine	Yes	No	No	No
40	$CaCO_3/CaO$	CSP	No	Air Brayton	Yes	No	No	No
57	$Ca(OH)_2/CaO$	CSP	No	Steam Rankine	Yes	Yes	No	No
58	$Ca(OH)_2/CaO$	TCES	Yes	Steam Rankine	Yes	No	No	No
59	$Ca(OH)_2/CaO$	TCES	Yes	Steam Rankine	Yes	No	No	No
60	$Ca(OH)_2/CaO$	CSP	No	Steam Rankine	Yes	Yes	No	No
61	$Ca(OH)_2/CaO$	CSP	Yes	Steam Rankine	Yes	Yes	Yes	Yes, 4 seasons
76	Perovskites	CSP	No	s-CO_2 Brayton	Yes	No	No	No
77	Co_3O_4/CoO	TCES	No	Air Brayton	Yes	Yes	No	No
78	Perovskites	CSP	Yes	Air Brayton	Yes	Yes	No	No
42	17 reactions	TCES	No	Various cycles	Yes	Yes	No	No
Thesis	$CaCO_3/CaO$ $Ca(OH)_2/CaO$ Mn_2O_3/Mn_3O_4	CSP	Yes	s-CO_2 Brayton	Yes	Yes	Yes	Yes, 6 scenarios

Accordingly, in this thesis (**Chapter 5**), we address these challenges by (1) adopting accurate reactor models, which include reaction kinetics and consider heat transfer in fixed-bed reactors using partial differential equations in time and space, (2) using a stochastic programming model to evaluate plant performance under seasonal solar variability, and (3) providing both energy efficiency and cost analyses. Moreover, our study has three additional advantages. First, we evaluate the integrated plant performance, taking into account the interactions between TCES system and other plant components. Second, we adopt supercritical CO_2 (s-CO_2) Brayton cycle, which has superior performance at high turbine inlet temperature than traditional steam Rankine cycle. Third, we develop and use a process model to simultaneously optimize the design and operation of CSP-TCES systems.

1.4 Thesis scope and outline

We aim to develop optimization-based models for the design and analysis of CSP with TCES systems and identify key areas of improvement for future TCES development.

The remainder of this thesis is structured as follows. In **Chapter 2**, we develop a general process model for CSP with fluid-phase TCES systems and apply it to ammonia and methane TCES systems with two gas storage options. Then, in **Chapter 3**, we propose an optimization-based framework for process synthesis under variability in two frequencies. In **Chapter 4**, we model CSP plants with fixed-bed reactors for solid-gas TCES systems, with special emphasis placed on the modeling of fixed-bed reactors using partial differential equations (PDEs) in time and space. In **Chapter 5**, we provide a system-level analysis for CSP employing various solid-gas TCES strategies, that is, different combinations of three chemical reactions and six process configurations. Finally, in **Chapter 6**, we conclude this study and discuss future directions.

Chapter 2

Process Modeling and Fluid-phase TCES[2]

This Chapter presents an integrated process and a general process model we develop for CSP plants with fluid-phase TCES systems. We illustrate our model applicability by using ammonia and methane TCES systems with aboveground and underground gas storage. The analysis allows us to identify critical issues as well as key targets for fluid-phase TCES systems.

2.1 General structure of TCES systems

We consider a general TCES system including the following five tasks (shown in **Figure 2-1**):

(1) **Reaction**: includes an endothermic reaction driven by concentrated sunlight and the reverse exothermic reaction generating heat for power generation.

(2) **Storage**: The products of the endothermic reaction are stored in a "hot" tank for night use, while exothermic reaction products are stored in a "cold" tank. Note that the "Hot" and "cold" are not defined with respect to storing temperature. In general, gaseous products are stored at low temperature to reduce storage volume while solid products can be stored at high temperature to fully utilize the sensible heat in addition to the reaction heat.

(3) **Separation** (optional): Unreacted reactants for both the endothermic and exothermic reactions are separated from products, so that higher conversions can be achieved and the purity in storage tanks is increased. However, when the separation is challenging, the separation cost may outweigh the benefits, in which case a process without separation is preferred.

---

[2] The contents of this chapter appear in Peng, Root and Maravelias, *Green Chem*. **2017**

(4) **Material handling**: maintain material flows in the process (e.g. pumps and compressors)

(5) **Heat recovery**: use a heat exchanger network to satisfy heat and cooling requirements

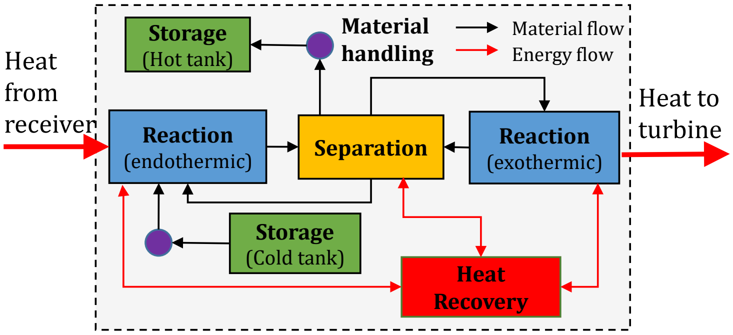

Figure 2-1. General structure of TCES systems.

Each task can be carried out using a variety of technologies, some of which are shown in **Figure 2-2**. For example, the metal hydride-based reaction ($M_xH_y \leftrightarrow xM + 0.5yH_2$) could take place in a fluidized bed or packed bed reactor, while the hydrogen generated could be stored in aboveground pressure vessels, underground caves or absorbent materials. **Figure 2-2** indicates that technologies used in fluid phase reactions differ from those used by gas-solid reactions. In this chapter, we focus on the well-studied fluid phase TCES systems, though the proposed model can be extended to study other TCES systems (e.g., solid-gas phase TCES).

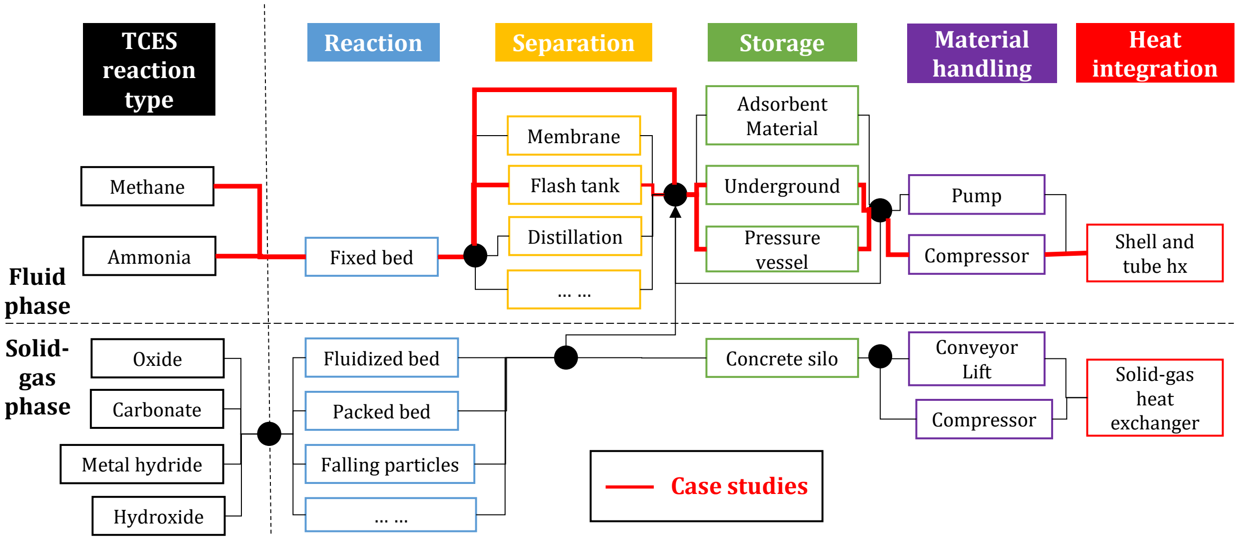

Figure 2-2. Technology alternatives for TCES tasks.

2.2 Optimization model

We develop an optimization-based CSP plant model. We first introduce three basic sets:

(1) Units $i \in \mathbf{I}$, with subsets $\mathbf{I}^{\mathbf{R}}$ (reactors), $\mathbf{I}^{\mathbf{SEP}}$(separation units), $\mathbf{I}^{\mathbf{TK}}$ (storage tanks), $\mathbf{I}^{\mathbf{C}}$ (compressors), and $\mathbf{I}^{\mathbf{E}}$ (heat exchangers).

(2) Streams $j \in \mathbf{J}$; each process unit, i, has inlet ($j \in \mathbf{J}_i^{\mathbf{IN}}$) and outlet ($j \in \mathbf{J}_i^{\mathbf{OUT}}$) streams.

(3) Components $k \in \mathbf{K}$, include reactants and products of the reversible reaction.

Figure 2-3 shows the important parameters and outputs of the optimization model, as well as main types of model equations. The complete list of parameters, variables and equations is given in **Appendix A1.1**.

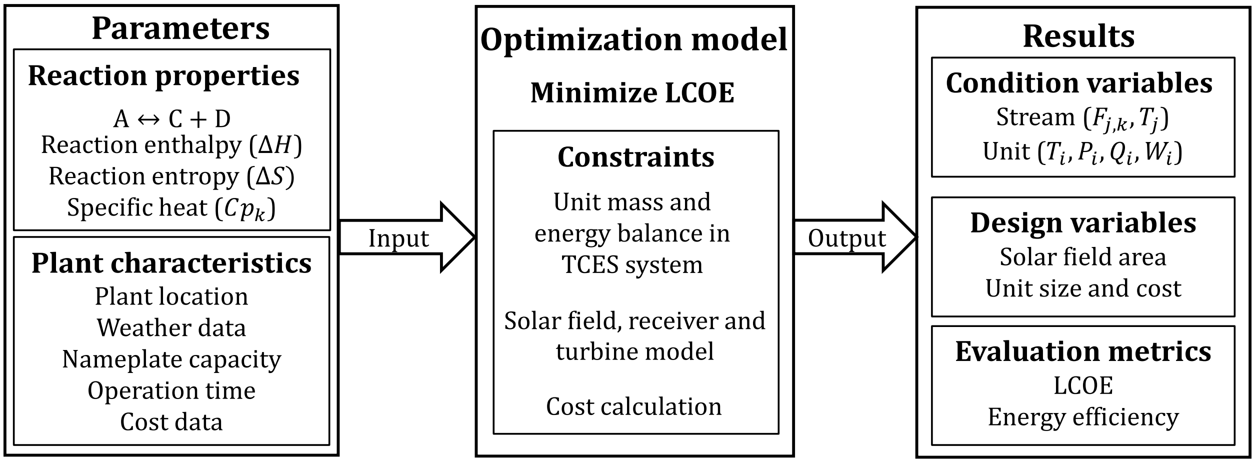

Figure 2-3. Optimization-based TCES process model.

The first type of input is reaction properties. The reversible reaction is expressed in a general form A+(B)↔C+D (for dissociation reactions, B does not exist). After selecting a specific reaction, its reaction enthalpy (ΔH) and entropy (ΔS), as well as the heat capacity for each component (Cp_k) are given as parameters. Other inputs are plant characteristics (e.g., location and weather) and plant specifications (e.g., size, operation time) as well as cost assumptions. For all base case analysis, the CSP plant is located in California, U.S. with an annual average of 10h sun-hours and 800W/m^2 direct normal irradiance (DNI). The plant has a nameplate capacity (P^{rate}) equal to 100 MW and operates 24 hours a day, with a nominal daytime operation time $t^{day} = 10h$ and storage time $t^{sto} = 14h$. All plant cost assumptions are based on the power tower configuration [89].

The main constraints of the optimization model are unit mass and energy balances (further explained in **Section 2.3.2**). Other constraints include the performance models of the solar field, receiver and turbine. Finally, the objective function is to minimize the plant LCOE. The output of the optimization model includes the plant LCOE and efficiency, as well as the corresponding process variables, including component flow rates ($F_{j,k}$), stream temperatures (T_j) and the operational conditions of each unit (unit temperature (T_i), pressure (P_i), heat duty (Q_i) and work load (W_i)). The design variables are the solar field area and the sizing of all units.

2.3 Modeling of fluid-phase TCES

2.3.1 Process flowsheets

Based on the TCES general structure (**Figure 2-1**), a process flowsheet for fluid phase TCES systems, with and without separation, is developed (**Figure 2-4**). Unlike traditional chemical plants, CSP plants operate in two different "modes", day and night. Some units, such as the reactor for the endothermic reaction (R1), operate only during the day; while some units, such as the reactor for the exothermic reaction (R2), run both during the day and during the night. To model two modes, a unit is represented as two units to refer to its day and night operational modes.

Figure 2-4A is the general process flowsheet of TCES with separation. During the day, stream 12 from the cold storage tank (TK2) and stream 11 from the bottom of separation unit (V1) are mixed to feed R1, where an endothermic reaction is driven by concentrated sunlight. The hot outlet stream 2, with major components C and D, is used to preheat the feeds of R1 and R2. Stream 5, from the top of separator V1, splits into stream 6, for day use, and stream 15, stored in the hot storage tank (TK1) for night use. In R2, the heat of exothermic reaction increases the temperature of the reactor effluent (stream 8). Heat is transferred from stream 8 to the turbine working fluid in heat exchanger (E4). During the night, stream 17 is sent from TK1 to R2 for power generation. Stream 22, from the top of V1 is recycled back to R2, while the bottom stream 23 is sent to TK2 for storage. Compressors C1 and C2 are used for the charging and discharging of TK1 and TK2.

A TCES system without separation (**Figure 2-4**B) has a simpler process. Stream 7 is cooled down for storage while stream 3 is directly sent to R2 to utilize both the sensible and reaction heat. The turbine is driven mostly by sensible heat during the day and reaction heat during the night.

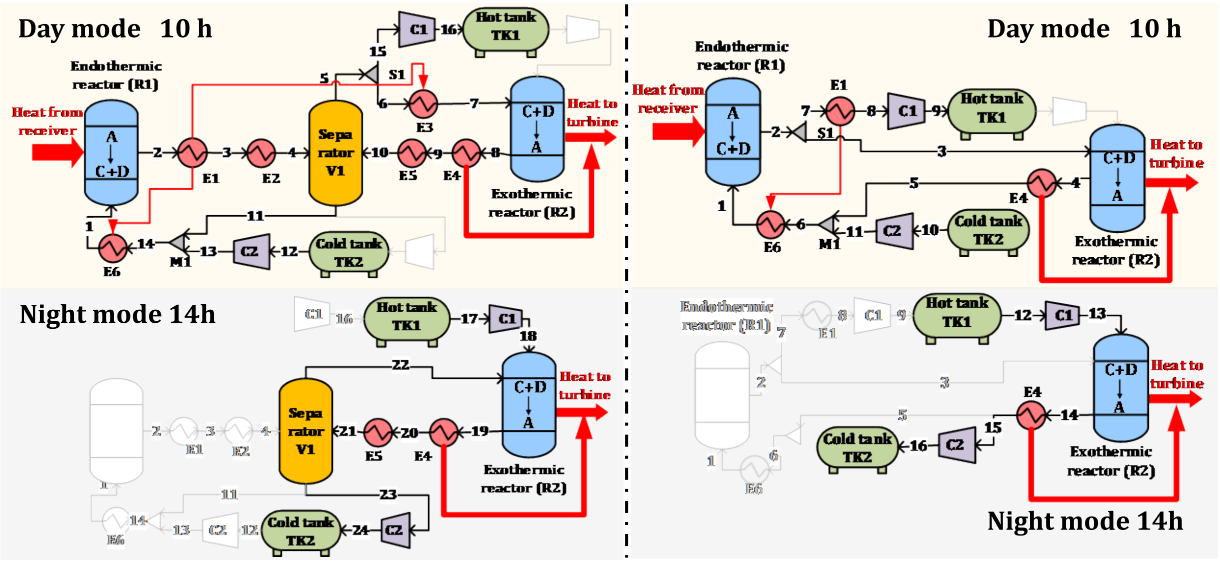

(a) (b)

Figure 2-4. Process flowsheets of TCES systems (A) with separation (B) without separation.

2.3.2 Unit models

The mass and energy balances are based on models for all units and connectivity equations through process streams. Next, we demonstrate the modeling approaches for the five types of units presented in **Section 2.1**.

Reaction

For a reactor ($i \in \mathbf{I}^{\mathbf{R}}$) with an inlet stream and outlet stream, **Figure 2-5** shows the related process variables and reaction parameters.

Both R1 and R2 are assumed as equilibrium reactors satisfying the Gibbs free energy equilibrium constant equation. The model can be readily extended to account for side reactions, if they also reach equilibrium, by simply adding their corresponding equilibrium equations. The Gibbs free energy (ΔG) can be calculated from the reaction enthalpy and reaction entropy at the reactor temperature (T_{OUT})

$$\Delta G = \Delta H_i - T_{OUT} \cdot \Delta S_i \quad i \in \mathbf{I^R} \tag{2-1}$$

and the equilibrium constant K_{eq} can be expressed as

$$K_{eq} = \prod_k \left(\frac{F_{OUT,k} \cdot P}{F_{OUT}^T \cdot P^{atm}}\right)^{v_k} \quad i \in \mathbf{I^R} \tag{2-2}$$

where P is the process pressure, P^{atm} = 1 atm, $F_{OUT,k}$ is the component molar flow rate of the reactor outlet stream *and* F_{OUT}^T is the total molar flow rate.

For the energy balance calculation, the reactor heat duty (Q_i) is equal to the enthalpy difference between the outlet stream and inlet stream. This enthalpy difference is the result of both component change and temperature change.

$$Q_i = \Delta H_i \cdot \left(F_{IN,A} - F_{OUT,A}\right) + (T_{OUT} - T_{IN}) \cdot \left(\sum_k F_{IN,k} \cdot Cp_k\right) \quad i \in \mathbf{I^R} \tag{2-3}$$

The heat absorbed by the solar receiver Q_{R1} is used to break chemical bonds and heat up the feed stream. In the exothermic reactor R2, the reaction heat increases the temperature of the reactor effluent, thereby delivering heat to the turbine at high temperature. The sensible heat is then used to generate steam in heat exchanger E4.

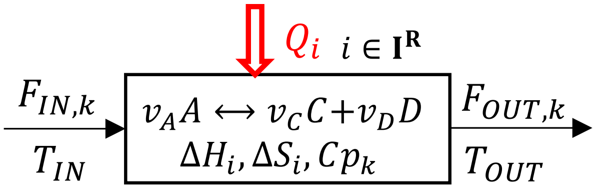

Figure 2-5. General reaction unit.

Separation

For a separation unit ($i \in \mathbf{I}^{\boldsymbol{SEP}}$), each component k is assigned a split fraction $\zeta_{j,k}$ for each outlet stream j. The mass balance of the separation unit can then be expressed as,

$$F_{j,k} = \zeta_{j,k} \cdot \sum_{j' \in \mathbf{J}_{\mathrm{i}}^{\mathbf{IN}}} F_{j',k} \quad i \in \mathbf{I}^{\boldsymbol{SEP}}, j \in \mathbf{J}_{\mathrm{i}}^{\mathbf{OUT}}, k \in \mathbf{K} \tag{2-4}$$

where $\zeta_{j,k}$ is a function of the separation technology, operating condition and feed compositions $F_{j',k}$. To calculate $\zeta_{j,k}$, we can either develop a complex first-principles separation model or a surrogate model from existing experimental or simulation data [90]. In **Appendix A1.2**, we demonstrate how to use the commercial process simulator ASPEN PLUS to generate a surrogate model for a flash tank used to separate $\mathrm{H_2}$ and $\mathrm{N_2}$ from $\mathrm{NH_3}$.

Storage

The mass balance for the two storage tanks TK1 and TK2 is,

$$F_{j',\boldsymbol{k}} \cdot t^{day} = F_{j,\boldsymbol{k}} \cdot t^{sto} \qquad i \in \mathbf{I}^{\mathbf{TK}}, j \in \mathbf{J}_{\mathbf{i}}^{\mathbf{OUT}}, j' \in \mathbf{J}_{\mathbf{i}}^{\mathbf{IN}}, k \in \mathbf{K} \tag{2-5}$$

where $t^{day} = 10\ hr$ is the day operation time and $t^{sto} = 14\ hr$ is the storage time.

To support a 100 MW plant running for 14 hours during the night, substantial amount of gas needs to be stored (see specific numbers in **Section 2.4**). Two gas storage options are considered:

(1) **Aboveground storage**: Using a series of 100 m^3 pressure vessels with maximum operating pressures of 700 bar[91], unit capital cost of 5700 $\$/m^3$, and a pressure factor of 0.44 [92].

(2) **Underground storage**: Compressed gas is stored in underground cavities with unit capital cost of 50 $\$/m^3$ and maximum pressure of 300 bar. Abundant industrial experience in natural gas underground storage since 1916[93] and multiple studies for hydrogen underground storage [94] suggest that this might be a feasible approach for TCES systems.

Although the capital cost of underground storage is notably lower, not all CSP plants can be located near an underground cave, so we study both alternatives (see **Appendix A1.4** for a geological map displaying locations with potential underground storage).

Material handling

Let P be the process pressure, P^H the maximum storage pressure, and P^L the minimum (cushion) storage pressure. Every 24 hours, each storage tank goes through the following four phases (**Figure 2-6**):

(1) Charging from P^L to P: gas flows into the tank without compression until the tank pressure reaches P;

(2) Charging from P to P^H: gas is compressed into the tank until the tank pressure reaches P^H at the end of the charging process (point B).

(3) Discharging from P^H to P: gas flows out of the tank without compression until tank pressure drops to P;

(4) Discharging from P to P^L: gas is compressed out of the tank until the tank pressure drops to the cushion pressure P^L at the end of the discharging process (point A).

Using these three pressure variables (P, P^H and P^L), we calculate the storage tank size, compressor size and electricity consumption. The size of the storage tank (V^{tank}) is calculated via,

$$V_i^{tank} = F_{IN}^T \cdot Z_{IN} \cdot t^{day} \cdot R \cdot T_{IN}/(P_\mathrm{i}^H - P_\mathrm{i}^L) \quad i = TK1 \tag{2-6}$$

where F_{IN}^T is the total molar flow rate of storage tank inlet stream (Stream 16), and Z_{IN} is the average compressibility factor of the inlet stream (a detailed calculation of Z is provided in **Appendix A1.6**).

In **Figure 2-6**, the blue line shows how compression power varies with time. Point A and B are compression power peaks during (discharging) phase 4 and (charging) phase 2. The compressor rated power (PWR) is the highest power needed between these two peaks,

$$PWR_i \cdot \eta^{comp} = \max\left\{FCp_{IN} \cdot Z_{IN} \cdot T_{IN} \cdot [\left(\frac{P^H}{P}\right)^{\frac{\gamma-1}{\gamma}} - 1]; FCp_{OUT} \cdot Z_{OUT} \cdot T_{OUT} \cdot [\left(\frac{P}{P^L}\right)^{\frac{\gamma-1}{\gamma}} - 1]\right\} \quad i = TK1 \qquad (2\text{-}7)$$

where FCp_{IN} is the flow heat capacity, γ is the heat capacity ratio, and η^{comp} is the compressor isentropic efficiency. Daily electricity consumption is calculated by integrating the compressor power over time.

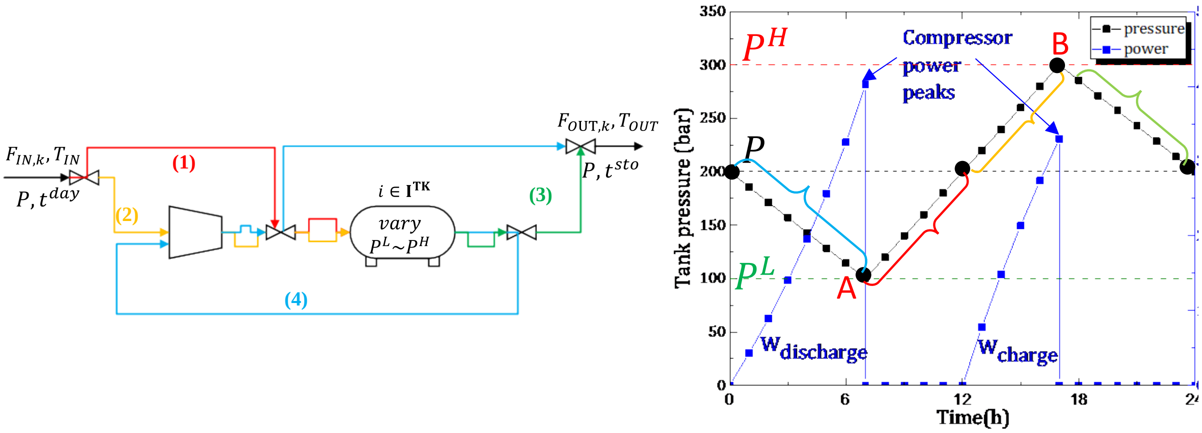

Figure 2-6. Tank pressure and compressor power changes in a day (TK1).

Heat integration

In general, the endothermic reaction occurs at high temperature but the gaseous reaction products are expected to be stored at low temperature to reduce gas storage volume. Recovering the sensible heat associated with this cooling process is necessary to achieve high energy efficiency. In our process, this heat is recovered by preheating the feeds of R1 and R2. The amount of exchanged heat is optimized accounting for both heat exchanger cost and gas storage cost. Besides product cooling, we also need to satisfy the heat duty for separation, which can be done through either utilities or process streams.

2.4 Results

The proposed model is used to analyze four CSP plants based on ammonia dissociation and methane dry reforming reactions, each with two gas storage options (**Table 2-1**). For each case, we present the energy efficiency and economics, as well as the main operational variables (complete results given in the **Appendix A1.3**). To compare the performance of TCES systems with sensible heat storage, the commercially developed molten salt two-tank system is chosen as the reference case. Please note that our analysis and conclusions are based on the relative comparison across all cases, not the absolute numbers. The major conclusions would remain the same if different plant operational and economic assumptions were used.

Table 2-1. Ammonia and methane reaction properties

TCES system	ΔH (kJ/mol)	ΔS $(J/\text{mol}\cdot K)$	C_p $(J/\text{mol}\cdot K)^*$				Gas storage option	
			A	B	C	D	Pressure vessel	Under ground
Ammonia dissociation $NH_3 \leftrightarrow 1.5\ H_2 + 0.5\ N_2$	55	117	72	-	30	33	Case 1	Case 2
Methane reforming $CH_4 + CO_2 \leftrightarrow 2CO + 2H_2$	260	284	67	62	30	33	Case 3	Case 4

* Temperature dependent heat capacities (given in **Appendix A1.5**) are used for all analyses.

2.4.1 Energy efficiency analysis

To evaluate the overall solar to electricity efficiency, we develop a simple model accounting for the efficiency of each CSP plant component based on the energy flows shown in **Figure 2-7**.

During the day, the heliostat reflects sunlight (E^{sun}) to a central receiver. Typically, this process has an average 40% energy loss [95] so we assume a constant collector efficiency (η^c) of 0.6.

Receiver efficiency (η^{r}) is defined as the ratio of heat absorbed in the endothermic reaction (Q_{R1}) to heat absorbed by the receiver. η^{r} decreases with increasing endothermic reaction temperature (T_{R1}), which leads to greater radiation and convection losses[96] (see **Figure 2-8**). The highest temperature of the heat delivered to the turbine from the TCES system ($Q_{R2} + Q_{E4}$) is at the exothermic reaction temperature (T_{R2}). Turbine efficiency (η^{p}) increases with T_{R2}.

Part of the turbine rated power output (P^{rate}) is consumed by compressors in the TCES system. The storage efficiency (η^{sto}) calculation accounts for both the heat loss in TCES and the compressor power consumption (W^{comp}, MWh/day), given as

$$\eta^{sto} = \frac{(Q_{E4}^{day}+Q_{R2}^{day})\cdot t^{day}+(Q_{E4}^{night}+Q_{R2}^{night})\cdot t^{sto}-\frac{W^{comp}}{\eta^{para}\cdot\eta^{p}}}{Q_{R1}\cdot t^{day}} \tag{2-8}$$

where $\eta^{para} = 0.9$ is the parasitic efficiency, considering a 10% parasitic load for the balance of plant.

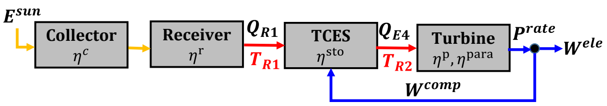

Figure 2-7. Energy flows and efficiency in a CSP plant.

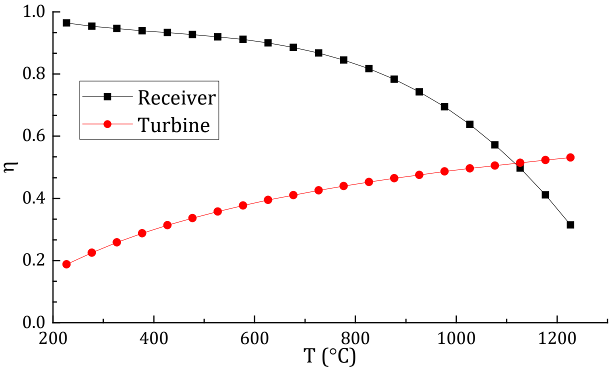

Figure 2-8. Receiver and turbine efficiency changing with temperature.

Finally, the solar to electricity conversion efficiency (η^{s-e}), defined as the ratio of daily net electricity output (W^{ele}) to total received solar energy, can be calculated by multiplying all block efficiencies,

$$\eta^{s-e} = \frac{W^{ele}}{E^{sun} \cdot t^{day}} = \eta^{c} \cdot \eta^{r} \cdot \eta^{sto} \cdot \eta^{p} \cdot \eta^{para} \tag{2-9}$$

Using the proposed energy model, we evaluate the energy efficiency of the four case studies, as shown in **Table 2-2**. Our analysis indicates that CSP plants employing fluid phase TCES systems have in general lower storage efficiency compared to plants with molten salt two-tank systems. The main reason is that in fluid phase TCES systems, compression is required during the charging and discharging process and this process consumes 17% of the generated power if pressure vessel is used for gas storage. Adopting underground gas storage, where products are stored at much lower pressure, could significantly reduce the compression power consumption and improve the overall energy efficiency and thus cost.

Table 2-2. Energy efficiency of CSP plant components.

Cases*	T_{R1}(°C)	T_{R2}(°C) day	T_{R2}(°C) night	Compression (% of P^{rate})	Separation cooling (% of Q_{R1})	η^{r}	η^{sto}	η^{p}	η^{s-e}
Reference	565	565	565	-	-	0.91	0.98	0.37	17.8%
1: NH_3, PV	386	539	399	17%	17%	0.94	0.70	0.32	11.2%
2: NH_3, UG	548	543	350	2%	14%	0.92	0.82	0.30	12.2%
3: CH_4, PV	1000	1000	645	18%	-	0.67	0.82	0.43	12.7%
4: CH_4, UG	919	919	692	3%	-	0.75	0.97	0.44	17.1%

* Reference: molten salt two-tank storage system, PV: pressure vessel, UG: underground.

Table 2-2 also shows that CSP plants employing ammonia based TCES systems have lower storage efficiency than those employing methane. This is because ammonia TCES systems are subject to heat loss for separation cooling. In Case 1 and Case 2, separation cooling is the secondary energy driver, consuming more than 17% of the heat flowing into TCES. To investigate whether separation is worthwhile, we design an ammonia TCES system without separation. The detailed results of Case 1, Case 1 without separation, and Case 3 are given in **Figure 2-9**, which shows the block flow diagrams of TCES systems with the optimized values of key process variables (e.g., mass and energy flows and unit operational conditions).

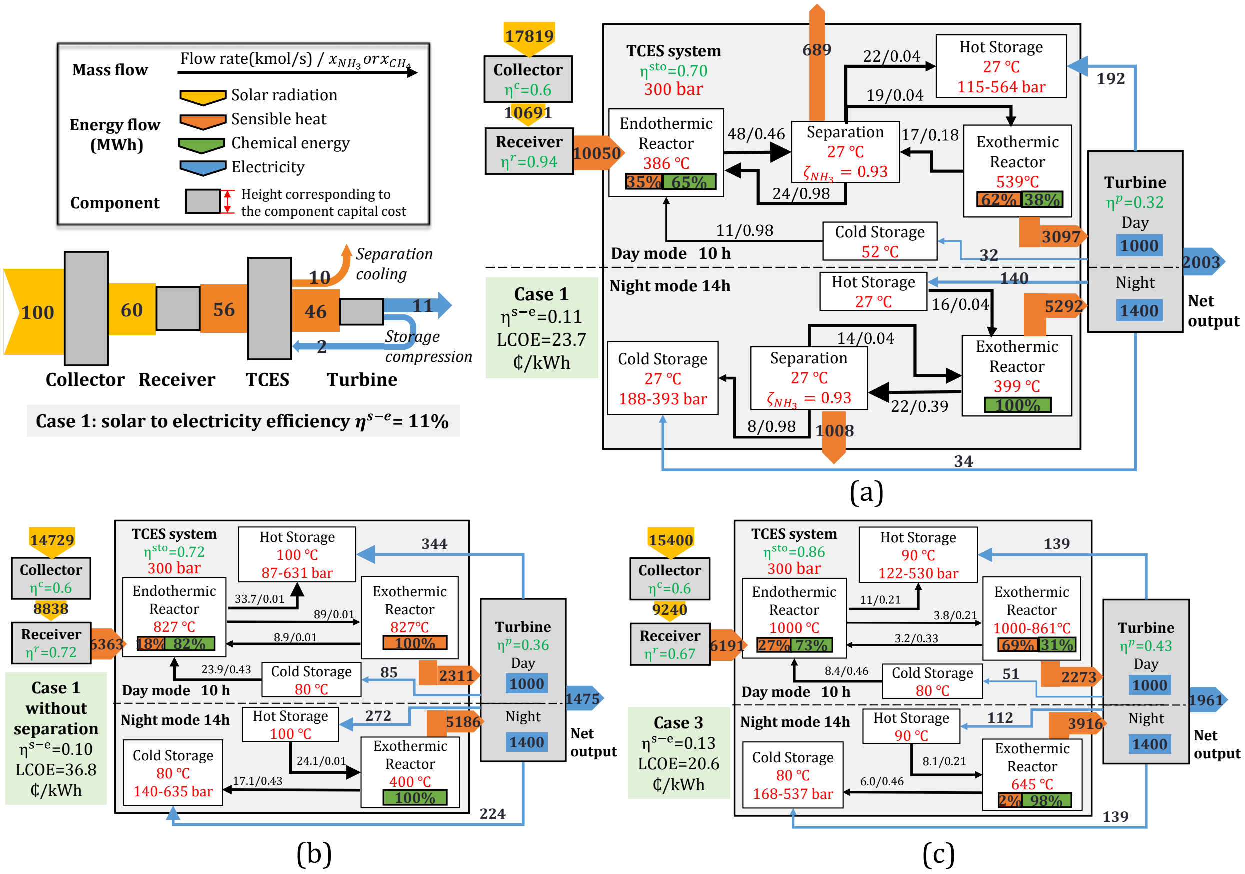

Figure 2-9. Block flow diagram of the CSP plant: (A) Case 1 (B) Case 1 without separation (C) Case 3.

Figure 2-9B shows that Case 1 without separation has no separation heat loss, but its storage efficiency is lower than that of Case 1 (**Figure 2-9**A), because the compression requirement doubles. Moreover, removing separation in Case 1 leads to an LCOE increase from 23.7 ₵/kWh to 36.8 ₵/kWh, primarily due to the increased gas storage cost and reduced electricity generation.

Separation is beneficial to ammonia TCES systems in three ways. First, after separation, reaction products are stored at lower temperature, which reduces the storage tank volume. Unreacted ammonia is cooled down to liquid phase and stored in the cold tank. Second, during the night, unreacted N_2 and H_2 are recycled back to the reactor from the separation unit, resulting in a smaller feed stream needed from the hot storage tank. Last, and the most important, separation can increase reaction conversions. Without separation, as shown in **Figure 2-9**B and C, the conversion of both the endothermic (Δx_{R1}) and exothermic (Δx_{R2}) reactions are equal to the difference between the equilibrium compositions at T_{R1} and T_{R2} (T_{R1} should be higher than T_{R2}). With separation, the inlet streams to both reactors contain practically pure components and T_{R1} could be lower than T_{R2}, as shown in **Figure 2-10**A. This also explains why ammonia TCES systems with separation has lower T_{R1} and higher receiver efficiency than methane systems without separation.

With respect to the turbine efficiency, methane TCES systems perform better than ammonia systems due to their higher T_{R2}. Results show that R2, where the exothermic reaction happens, is almost adiabatic, and T_{R2} can be estimated by,

$$T_{R2} = \frac{\Delta H \cdot \Delta x_{R2}}{\overline{C_p}} + T_{TK1} \tag{2-10}$$

where ΔH is the reaction enthalpy, $\overline{C_p}$ is the average stream heat capacity and Δx_{R2} is the reaction conversion (see **Figure 2-10**). The storage tank temperature (T_{TK1}) is 27°C in the ammonia system and 90°C in the methane system.

The high T_{R2} of methane TCES system results from its high $\Delta H/\overline{C_p}$, which is 6050 °C compared to 1570 °C for ammonia. Generalizing this analysis, high $\Delta H/\overline{C_p}$ is a good criterion for reaction selection.

With respect to the overall plant efficiency, methane TCES systems without separation are superior to ammonia systems. Underground gas storage leads to compression power reduction and higher plant efficiency. Case 4 has the highest storage efficiency, but its overall efficiency (η^{S-E}) is lower compared to the efficiency of two-tank molten-salt storage, due to the low receiver efficiency as a result of high T_{R1}.

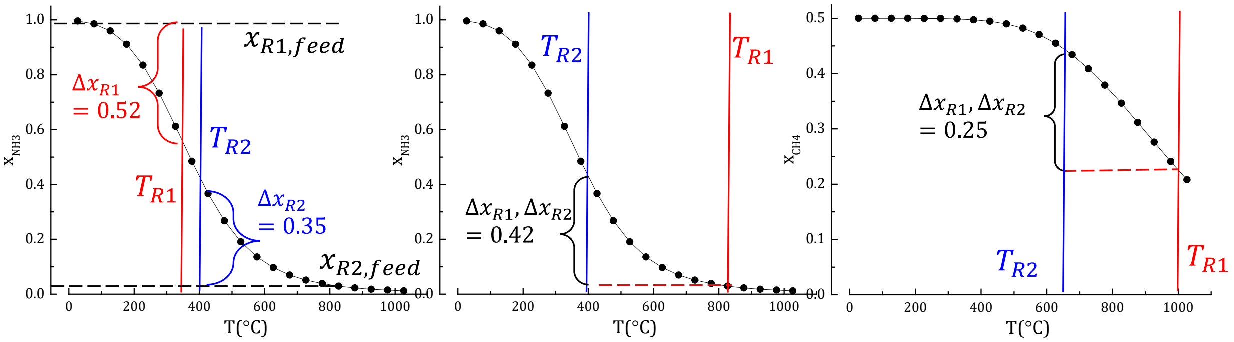

(a) (b) (c)

Figure 2-10. Equilibrium curves of ammonia dissociation and methane reforming reactions at 300 bar. (A) Case 1, (B) Case 1 without separation, and (C) Case 3. The optimum reaction temperatures and conversions of endothermic and exothermic reactions are shown as red and blue.

2.4.2 Economic analysis

To evaluate the economic feasibility of the studied systems, we use levelized cost of electricity (LCOE) as the primary metric, defined as,

$$LCOE = (CAPEX \cdot CRF + OPEX)/(365 \cdot W^{ele}) \tag{2-11}$$

where *CAPEX*, the total capital cost, includes four plant components: collector, receiver, storage and turbine. The storage cost accounts for all units in the TCES process flowsheets (**Figure 2-4**); and *CRF* is the capital recovery factor used to calculate the equivalent annual capital cost. Assuming a 9% interest rate and 30 years plant operation, *CRF* is 0.1; *OPEX* is the annual operation cost for utility use and plant maintenance; and W^{ele} is the daily net electricity output (detailed cost assumptions and calculations are given in **Appendix A1.1**).

The LCOE of the four case studies is shown in **Figure 2-11**. The processes employing pressure vessels (Case 1 and 3) have notably higher LCOE. This is because, even if reaction products are compressed and stored at around 550 bar, both ammonia and methane systems require 65,000 m^3 of gas storage at a vessel price of 8900 \$/m^3. Moreover, compression reduces the overall plant efficiency, which increases the unit cost of all subsystems. If underground gas storage is geologically available, in which case the storage unit price is 50 \$/m^3, TCES systems become more attractive.

Furthermore, CSP plants employing methane TCES systems have lower LCOE than those employing ammonia. Methane systems mainly benefit from the high ΔH which reduces the reactant storage demand. Overall, Case 4 has the lowest LCOE, achieving a 13% LCOE reduction over the two-tank molten salt CSP plants. In two-tank systems, the storage media (molten salt) dominates the storage system cost, while in TCES systems, storage media cost is significantly lower due to the low price of chemicals (ammonia and methane) and high storage density (see **Table 1-1**).

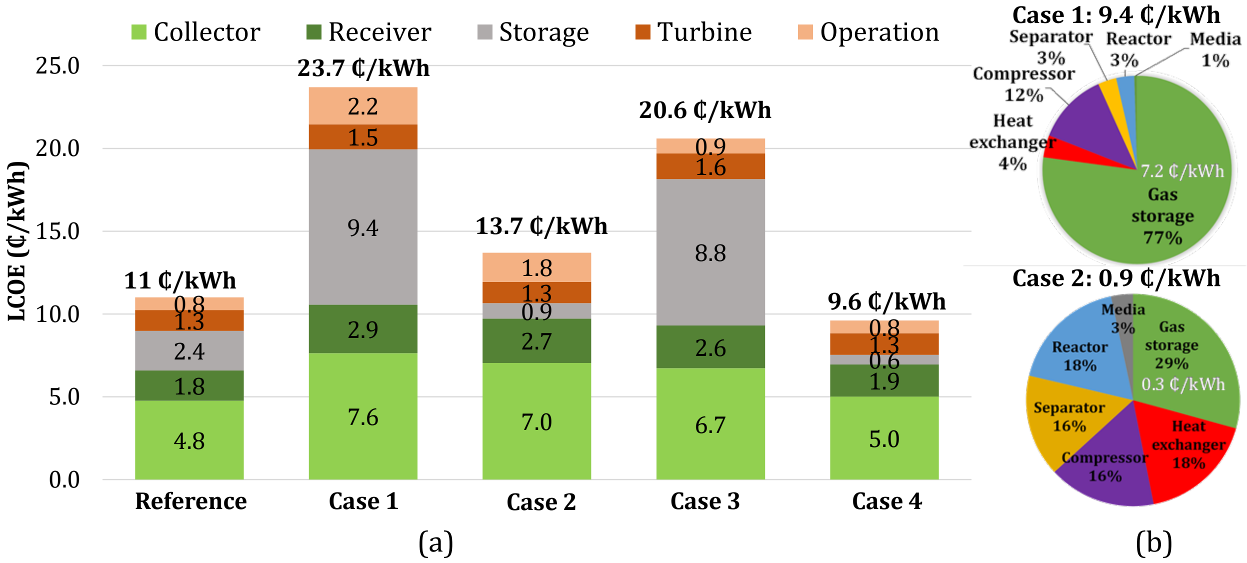

Figure 2-11. LCOE contributions of (A) CSP plants and (B) TCES systems.

2.4.3 Operational analysis

Operational conditions affect reaction conversions, plant efficiency, and consequently economics. In this subsection, we derive simple cost functions to describe the impact of reaction temperature and operating pressure. We also use optimization results to provide general insights.

Reaction temperature

The temperature of the endothermic (T_{R1}) and exothermic (T_{R2}) reaction influence the total CSP plant cost (C^{plant}), which consists of the solar collection cost and gas product storage cost:

$$C^{plant} = [\frac{\lambda^{collection}}{\eta^r \cdot \eta^p} + \lambda^{storage} \cdot F^{sto} + c1] \cdot P^{rate} \tag{2-12}$$

where $\lambda^{collection}$ is the solar energy collection cost, including collector and receiver costs; $\lambda^{storage}$ is the gas storage cost, including the cost of tanks and compression; and P^{rate} is the plant rated capacity. To simplify the cost expression, turbine and operation costs are lumped into constant $c1$.

Eqn. (2-12) shows that the collection cost is inversely proportional to the receiver efficiency (η^r) and turbine efficiency (η^p). Further, η^r decreases with increasing T_{R1} while η^p increases with T_{R2} (see **Figure 2-8**). Therefore, low T_{R1} and high T_{R2} lead to low collection cost. The storage cost is proportional to the gas flow rate (F^{sto}), which can be calculated from the heat balance of R2,

$$F^{sto} = P^{rate}/(\Delta x_{R2} \cdot \Delta H \cdot \eta^p) \tag{2-13}$$

where Δx_{R2} is the exothermic reaction conversion and its relation between T_{R1} and T_{R2} are described in **Figure 2-10**. As $T_{R1} - T_{R2}$ increases, Δx_{R2} increases thereby leading to lower storage cost, but at the expense of lower receiver and turbine efficiency. Eqn (2-13) also shows the benefit of high reaction enthalpy, which makes methane TCES systems more cost effective than ammonia systems.

Using our optimization model, we obtain the optimum T_{R1} and T_{R2}, 1000 °C and 645 °C respectively, while the reaction turning temperature (T^*) is 700°C. For the ammonia-based TCES system, T_{R1} (386°C) is lower than T_{R2} (399°C) and its T^* is 200°C. These results suggest that there are two approaches to dealing with the trade-off between collection cost and storage cost. First, T_{R1} and T_{R2} should be in the vicinity of T^* where the equilibrium composition changes fast with reaction temperature. Thus, maximum Δx_{R2} can be achieved with a small difference between $T_{R1}\ and\ T_{R2}$. Second, separation can increase the reaction conversion and allow $T_{R1} < T_{R2}$.

Operating pressure

The process pressure (P), maximum (P^H) and minimum (P^L) storage pressure determine the total gas storage cost, $C^{storage}$, which includes storage tanks, compressors, and electricity consumption,

$$C^{storage} = \lambda^{tank} \cdot \left(\frac{F^{sto}}{P^H - P^L}\right) + \lambda^{comp} \cdot \left(ln\frac{P^H}{P} + ln\frac{P}{P^L}\right) + LCOE \cdot \left(\frac{P^H}{P} + \frac{P}{P^L}\right) \qquad (2\text{-}14)$$

where λ^{tank} and λ^{comp} are the unit capital costs of storage tank and compressor. To calculate the cost of compression power consumption, $LCOE$ is used as an estimation of the electricity price.

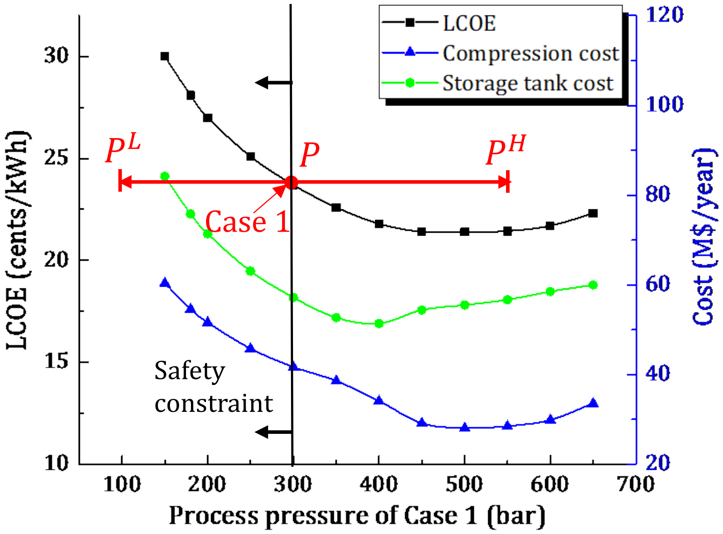

Figure 2-12. Impacts of process pressure on compression work and LCOE in Case 1.

Eqn (2-14) shows that the storage tank cost is inversely proportional to $P^H - P^L$, while the compression cost, including both the compressor and electricity cost, is proportional to P^H/P and $\mathrm{P/P^L}$. Thus, there is a trade-off between storage tank cost and compression cost.

To study this trade-off, we solve our model for several values of P from 150-600 bar. For each value, all other variables are optimized to yield the minimum LCOE. **Figure 2-12** shows how the storage tank cost, compression cost and LCOE change with P in Case 1. Staring at 150 bar, increasing P leads to a steep decrease in both compression and storage cost because, with the same ratio of P^H/P and P/P^L, higher P leads to larger $P^H - P^L$. However, when P exceeds 400 bar, storage cost rises with P. This is because P^H has an upper limit of 700 bar, so increasing P leads to higher P^L and thus smaller $P^H - P^L$. The optimum P is around 500 bar, but we used an upper bound of 300 bar for operation safety.

Figure 2-12 shows the corresponding $P^H(560\text{ bar})$ and $P^L(115\text{ bar})$ when P = 300 bar. Case 1 uses expensive pressure vessel storage with $\lambda^{tank} = 9250\ \$/\mathrm{m}^3$. The difference between P^H and P^L is large, reducing the storage volume at the expense of more compression power consumption. In Case 4, when cheap underground gas storage ($50\$/\mathrm{m}^3$) is employed, $P^H - P^L$ is only 40 bar, leading to smaller electricity consumption and larger storage volume. Moreover, unlike Case 1, LCOE is not sensitive to the variation of P in Case 4, which imparts the plant more operation flexibility.

2.4.4 Sensitivity analysis

To understand how various parameters affect the LCOE, we perform sensitivity analyses on Case 1 and Case 4 (**Figure 2-13**). We choose these two cases because Case 1, using well-developed ammonia and pressure vessel technologies, can be readily implemented in the near-term; while Case 4 is technically more challenging but has lower LCOE, so it can be implemented in the future.

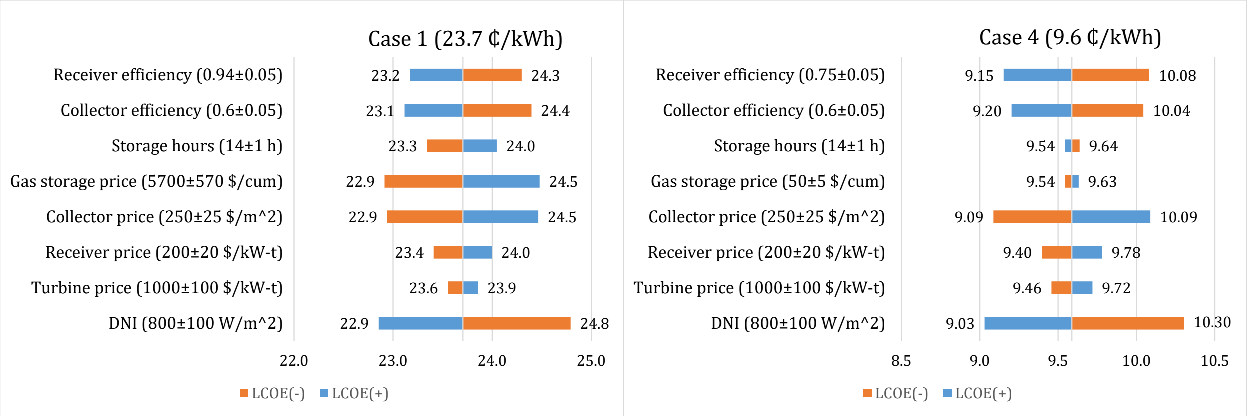

Figure 2-13. Tornado chart for various CSP characteristics in Case 1 and Case 4.

Improving collector and receiver efficiency has been a long-term goal for CSP research. Our analysis shows that a 2% increase of the collector or receiver efficiency could lead to a 1% LCOE decrease for both cases. With respect to solar resource evaluation, we observe that direct normal irradiance (*DNI*) plays an important role: a 12.5% decrease results in an increase around 1 ₵/kWh in LCOE. We next study the storage system size, denoted by storage hours. For Case 1, where the TCES system is expensive, LCOE increases by 0.3 ₵/kWh if the storage time increases to 15 hour; while for Case 4, the LCOE decreases slightly. The impact of other plant components is analogous to their LCOE contribution (collector > receiver > turbine). Finally, the gas storage price has a great influence on LCOE in Case 1, when pressure vessel is the main cost driver.

2.5 Conclusions

In this chapter, we established a framework for the systematic study of different TCES systems. We developed a general process for CSP plants employing TCES systems, formulated an optimization-based model of the process, and used this model to study four different systems and perform different types of analyses. We identified that, for fluid phase TCES systems, the main cost driver is the gas storage and the main energy driver is the electricity consumption for compressors. The overall efficiency and LCOE can be significantly improved if cheap underground gas storage is available. We also showed that careful design of separation system is critical. Finally, we discussed the impact of reaction temperatures and operating pressure. The proposed model can be used to study a wide range of systems, including solid-gas phase reactions, which will be the topic of future research. Finally, we hope that the proposed framework will be used not only for the evaluation of existing TCES systems, but also as a tool for the development of new CSP-TCES systems.

Chapter 3

Optimization-based Process Synthesis under Seasonal and Daily Variability[3]

In **Chapter 2**, the CSP plant was designed based on an annual average solar condition. To consider the seasonal and daily variability in solar irradiance, in this chapter, we propose an optimization-based framework for process synthesis under variability in two frequencies.

3.1 Introduction

Process synthesis under variability is a problem that is expected to receive considerable attention in the future due to the emergence of energy systems that are subject to variability in the availability of intermittent renewable sources. One common approach in handling variability is to

---

[3] The contents of this chapter appear in Peng, Root and Maravelias, *AIChE J*. **2018**

employ multiple scenarios/periods with different operating conditions and then formulate the synthesis problem as a multiscenario/multiperiod optimization problem [97]. This approach has been widely used for the synthesis of flexible processes, such as heat exchanger networks [98,99], separation systems [100,101], and energy systems [102–107]. This multiscenario approach is applicable when there is variability in one timescale. However, many systems, including systems employing renewable energy sources and buildings, involve variability in multiple scales. For example, the ambient temperature (important in building energy optimization) exhibits seasonal (low frequency) and daily (high frequency) variability (see **Figure 3-1**).

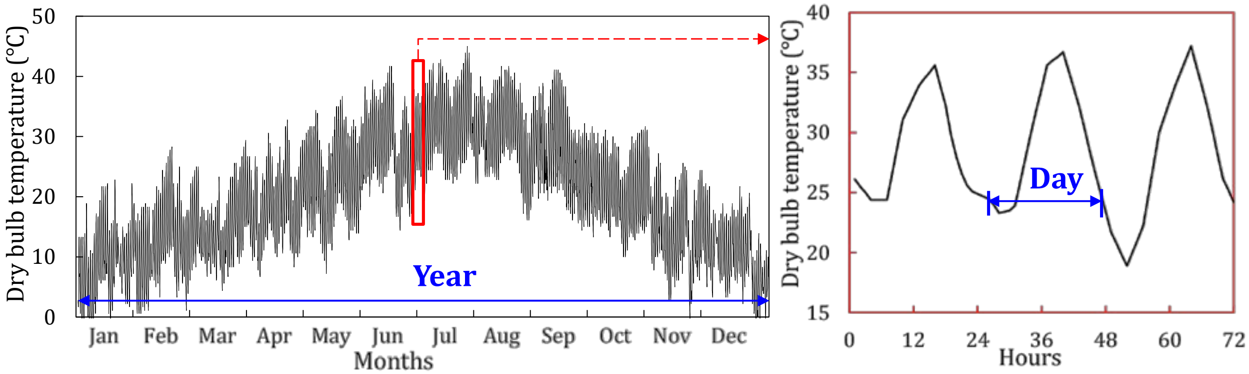

Figure 3-1. Seasonal (left) and daily (right) variability of ambient temperature in California.

The majority of research in the area of chemical process synthesis has focused on systems which operate in a single mode and also have reasonably small variability in terms of availability and quality of resources. Thus, variability is modeled as a “deviation” from the nominal operating mode. Furthermore, it is assumed that variability effects can be compensated for through control actions [108]. This treatment can be challenging, however, when the variability is so large and persistent that large subsystems of the process are essentially operating in completely different “modes”, or even, are shut down during, for example, the course of a day.

Accordingly, the and high frequency variability, coupled with a superstructure-based approach where different units may goal of this chapter is to develop a framework for the systematic design of processes under variability in two frequencies, for example, seasonal and daily variability. In doing so, we employ “scenarios” and “modes” to represent low be active during different modes. The resulting optimization model is a two-stage stochastic programming model with multiple modes embedded within each scenario. Finally, a propagation-based bound generation algorithm is proposed to enhance the solution. Design decisions are the first stage decisions, while operational decisions, for each scenario and mode, are second stage decisions. The proposed framework: (1) accounts for the two-frequency variability in an accurate yet tractable manner; (2) allows different units to be activated to handle high-frequency variability; and (3) considers temporal correlations among modes. The proposed framework enables the efficient optimization-based synthesis of renewable energy systems where parameters describing the energy resource (e.g., solar, wind) exhibit variability in two scales [4,6,109–113].

The remaining of this chapter is structured as follows. In the next section, we provide background on the synthesis of flexible chemical processes, stochastic programming (SP), and solution methods for SP models. Then, we present the optimization framework, which includes scenario and mode generation, multimode superstructure generation, the multimode two-stage stochastic programming model, and a propagation algorithm for bound tightening. Next, we illustrate the applicability of the proposed framework through the synthesis of concentrating solar power plants (CSP) with thermochemical energy storage (TCES). Finally, we compare the performance of the proposed approach with *conventional* stochastic and deterministic approaches through a simple illustrative example.

3.2 Background

3.2.1 Process synthesis and operational flexibility

Pioneered by Rudd, Powers, and Siirola [114] , process synthesis has become an active research area over the past 60 years. The goal in a process synthesis exercise is to select unit operations and their interconnections so as to optimize a specific metric subject to given constraints [115,116]. A number of extensive reviews are available, including reviews on heat exchanger network synthesis [117–119], separation network synthesis [120,121], reactor network synthesis [122] and water network synthesis [123].

Optimization-based approaches, in general, are one of the three major approaches to process synthesis [124]. Optimization superstructure-based approaches, in particular, have been proposed as an effective way to simultaneously consider and evaluate a large number of process alternatives. They have three main components: process representation, modeling [125–127], and solution of the resulting optimization models [128–131], typically a mixed-integer nonlinear (MINLP) model.

Most previous process synthesis approaches consider a single nominal operating mode. While this assumption is appropriate for the majority of *traditional* chemical processes, the emergence of systems that operate at widely different conditions (e.g., solar power plants), interacting with systems that operate at different conditions (e.g., natural-gas-fired power plants in a grid with significant renewable electricity) or simply being subject to time-varying constraints (e.g., buildings subject to ambient temperature and occupancy fluctuations) has led to the need to develop methods that account for inherent variability, often in multiple sources and at different frequencies.

One approach to account for variability is the design of flexible chemical processes which ensures feasible operation under parameter variations [97]. Systematic approaches have been developed for using a quantitative index to measure the size of feasible operation space and then establishing trade-offs between feasibility and cost through a multiobjective approach [132–136]. Another approach is to design a system that has a fixed degree of flexibility at minimum cost. Specifically, potential operating conditions are first specified in terms of either a bounded region or a finite number of scenarios/ periods, and then the optimization model seeks to find the most economic design that can meet all specifications under all considered conditions. To solve this process synthesis problem, various mathematical programming approaches have been proposed [137], including stochastic programming [138–140] and robust optimization [141–144]. Stochastic programming has the advantage of utilizing the probability distribution information of uncertain parameters and allowing recourse actions once uncertainty is revealed, which leads to less conservative results compared to robust optimization.

In this chapter, rather than considering a single operating mode and treating variability as a deviation from the nominal operating mode (potentially via scenarios), we employ scenario and multiple modes and, importantly, we allow the process to operate under vastly different operating modes. The proposed approach leads to a two-stage stochastic programming models with a number of interconnected modes within each scenario.

3.2.2 Stochastic programming

The general formulation of a two-stage stochastic programming model is as follows [145]:

$$\min_{\boldsymbol{x}} \; f^1(\boldsymbol{x}) + E_{\boldsymbol{\theta}}\{Q(\boldsymbol{x},\boldsymbol{\theta})\} \qquad \boldsymbol{x} \in \mathbb{R}^{n1},\ \boldsymbol{\theta} \in \mathbb{R}^{n2}$$

$$Q(\boldsymbol{x},\boldsymbol{\theta}) = \min_{y} f^2(\boldsymbol{x},\boldsymbol{y},\boldsymbol{\theta}) \tag{3-1}$$

$$\text{s.t.} \quad h(\boldsymbol{x},\boldsymbol{y},\boldsymbol{\theta}) = 0;\ g(\boldsymbol{x},\boldsymbol{y},\boldsymbol{\theta}) \le 0 \quad \boldsymbol{y} \in \mathbb{R}^{n3}$$

where $\boldsymbol{x}$ is the vector of first stage decisions which are made prior to the uncertainty realization; $\boldsymbol{y}$ is the vector of second stage decisions which are made after the realization of uncertain parameters $\boldsymbol{\theta}$ which is described by a continuous probability distribution function or a finite number of discrete scenarios through sampling approximations; $h(\boldsymbol{x}, \boldsymbol{y}, \boldsymbol{\theta})$ and $g(\boldsymbol{x}, \boldsymbol{y}, \boldsymbol{\theta})$ are vectors of equality and inequality constraints, respectively; and the objective function contains the first stage cost $f^1(\boldsymbol{x})$ and the expectation of the minimum second stage cost $Q(\boldsymbol{x}, \boldsymbol{\theta})$ over all realizations.

The scenario-based stochastic problem can then be written as,

$$
\begin{aligned}
&\min_{x} \; f^1(\boldsymbol{x}) + \textstyle\sum_s \pi_s \cdot Q_s(\boldsymbol{x}, \boldsymbol{\theta_s}) \quad \boldsymbol{x} \in \mathbb{R}^{n1}, \boldsymbol{\theta_s} \in \mathbb{R}^{n2} \\
&\qquad Q_s(\boldsymbol{x}, \boldsymbol{\theta_s}) = \min_{y} f^2(\boldsymbol{x}, \boldsymbol{y_s}, \boldsymbol{\theta_s}) \quad \forall\, s \in \mathbf{S} \qquad (3\text{-}2) \\
&\qquad \text{s.t.} \quad h_s(\boldsymbol{x}, \boldsymbol{y_s}, \boldsymbol{\theta_s}) = 0;\; g_s(\boldsymbol{x}, \boldsymbol{y_s}, \boldsymbol{\theta_s}) \le 0 \qquad \boldsymbol{y_s} \in \mathbb{R}^{n3}
\end{aligned}
$$

where $\boldsymbol{\theta_s}$ and π_s are the values of uncertain parameters and the probability of scenario $s \in \mathbf{S}$.

In this study, we deal with variability, as opposed to uncertainty. While the latter refers to the unknown, single, true value of a quantity and is described by a probability distribution based upon our state of information, the former refers to the true values of a quantity varying with time and is quantified by frequency distribution derived from observed data[146]. The fact that both uncertainty and variability are represented by distributions allows us to employ stochastic programming to address problems under variability in one time scale. In this setting, $\boldsymbol{\theta_s}$ and π_s are redefined as variability parameter values and frequency of scenario occurrence, respectively. Also, the objective function involves the minimization of the total cost, including (1) the capital cost (a function of first stage decisions); and (2) the operational cost (a weighted function of second stage decisions), where the summation over scenarios represents, essentially, a weighted sum over time, instead of the expected cost over realizations of random events. We note, however, that traditional two-stage stochastic programs cannot readily account for variability in two frequencies.

3.2.3 Solution methods

The main challenge associated with stochastic programming models, especially when functions $h_s(\boldsymbol{x}, \boldsymbol{y_s}, \boldsymbol{\theta_s})$ and $g_s(\boldsymbol{x}, \boldsymbol{y_s}, \boldsymbol{\theta_s})$ are nonlinear and involve binary variables, as in process synthesis problems, is that they quickly become intractable as the number of scenarios increases. To solve the resulting nonlinear programming (NLP) or mixed-integer nonlinear programming (MINLP) models, various global solvers such as BARON [147], SCIP [148], Couuenne [149] and Antigone [149] have been developed. To speed up the convergence to the global optimum, various domain reduction techniques have also been proposed to reduce the infeasible and suboptimal domains [150–152].

Among these techniques, propagation-based bound tightening is generally effective and computationally inexpensive. For chemical production scheduling, Velez et al. proposed a back-propagation algorithm based on customer demands [153] while Merchan and Maravelias proposed a forward-propagation algorithm based on inventory and resource availability [154]. Kong et al. extended these algorithms to address chemical process synthesis problems. Specifically, they developed methods for the calculation of bounds on component molar flows [155]. However, the aforementioned methods are not effective for problems with significant variability because the scenario-independent bounds they yield are rather weak.

Finally, the solution of stochastic programming models can be enhanced by exploiting their structure [156,157]. The original complex problem can be decomposed into a sequence of subproblems, which can then be solved in parallel independently. Two main classes of decomposition methods for stochastic programming are Lagrangian decomposition [158,159] and L-shaped method [160]. Several extensions of Bender's decomposition or L-shaped methods have been developed for nonlinear [161], nonconvex MINLP [162], and multi-stage stochastic programming problems [163].

3.3 Modeling framework

The outline of the proposed framework is given in **Figure 3-2**. In the remainder of the chapter we will consider daily and seasonal variability, but the proposed methods are applicable to problems under variability in any two frequencies, provided that there is there is sufficient time scale separation (see discussion in the following subsection). We use "scenarios" to represent seasonal variability and "modes" to represent daily variability. Scenarios ($s \in \mathbf{S}$) are representative days, each with a frequency of occurrence (π_s) within a year. For example, the variability of ambient temperature over a year can be represented by three scenarios: a typical winter day (25%), summer day (25%) and mid-season day (50%). Modes ($m \in \mathbf{M}$) are essentially time periods within a day; and the values of the varying parameters in each mode are notably different from the corresponding values in another mode. For example, day and night modes may be used to describe daily solar irradiance variation.

All scenarios have the same types of modes, which further occur in the same sequence, thereby allowing us to use the same temporal connections between consecutive modes across all modes. For example, operation between consecutive modes is linked through material and energy balances across modes. However, the parameter values and duration of modes are different across scenarios. For example, the day mode of a summer day scenario has higher solar irradiance and longer duration than the day mode of a winter day scenario.

The main motivation behind using modes to represent daily variability is to enable the activation of different units and thus selection of different active flowsheets during the course of a day.

Another motivation for using modes (i.e., coarse time periods), instead of more refined time steps (e.g., 1-hour steps), is computational tractability, since we aim to employ relatively detailed unit models (e.g., reactor models with kinetics or equilibrium relationships) and even consider, simultaneously, heat integration (which plays a key role in the development of renewable energy systems).

As shown in **Figure 3-2**, the proposed framework consists of four components: (1) scenario and mode generation; (2) multi-mode superstructure generation; (3) formulation of multimode stochastic programming model; and (4) propagation-based bound generation. In the following subsections, we present these four components in detail.

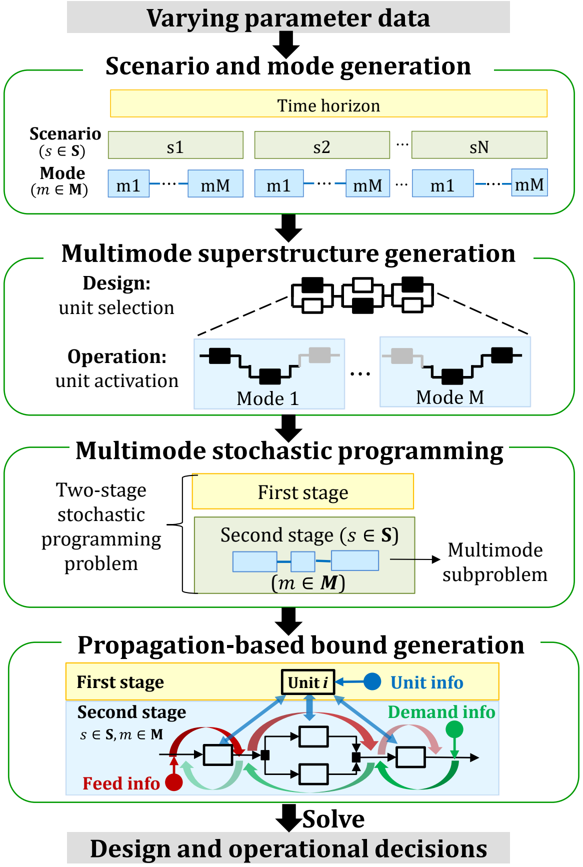

Figure 3-2. Overview of the proposed optimization framework.

3.3.1 Scenario and mode generation

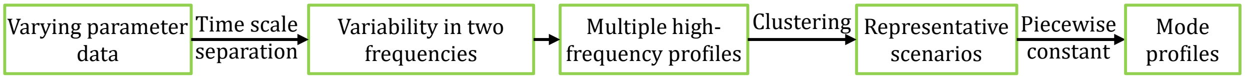

Figure 3-3. Procedure of scenario and mode generation.

The procedure of scenario and mode generation is shown in **Figure 3-3**. The proposed framework is applicable when the variability is in two frequencies whose timescales are order-of-magnitude different. Thus, the first step is to identify the two frequencies from the varying parameter data over the given time horizon. In some cases, the two frequencies are easy to determine (e.g., seasonal and daily variability for solar irradiance). In cases when the two frequencies are not obvious, *time filters* can serve as a useful tool to split the variability of a time series into 'fast' and 'slow' components [164]. For example, (1-2-1) and running mean are two simple filters for suppressing high frequency variability. For further information about different time filtering techniques, please refer to the following standard texts [165–167].

The second step is to divide the entire time horizon into L time periods, each with the timescale of high frequency variability. As for seasonal and daily variability, one-year horizon is divided into 365 days and daily profiles of the varying parameters ($\boldsymbol{\theta}$) are obtained. Due to the complexity of process synthesis problems, a small number (N) of typical days (i.e., scenarios) are selected to represent these L days. The scenarios can be generated through a variety of methods, including centroid clustering algorithms (e.g., k-means clustering), where L profiles partition into N clusters so as to minimize the total point-to-centroid Euclidean distance. The profile and occurrence frequency (π_s) of each cluster centroid (i.e., scenario) are the mean profile and the fraction of occurrences of all days belonging to the corresponding cluster. **Figure 3-4**A shows how the total point-to-centroid distance decreases with the increase in the number of scenarios in the solar irradiance case. The daily solar condition (described by daytime average solar irradiance and sun hours) and π_s of each scenario, if six scenarios are chosen to represent seasonal variability, are shown in **Figure 3-4**B and C, respectively.

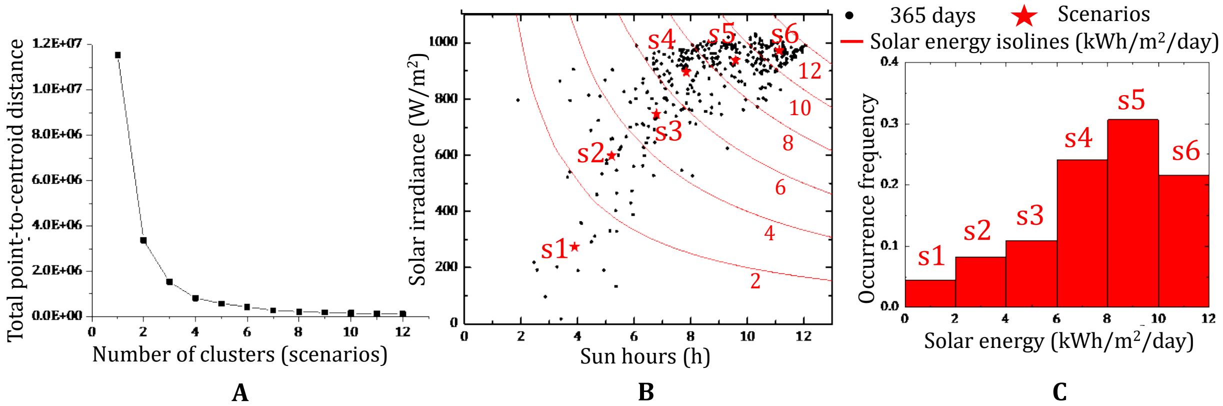

Figure 3-4. (A) Total point-to-centroid distance decreases with the number of scenarios. (B) Solar conditions and (C) occurrences of the 6 scenarios generated from 365 days

The third step is to identify M modes from common patterns in daily profiles of $\boldsymbol{\theta}$. A piecewise constant approximation with M intervals (modes) is then applied to approximate daily profiles of each scenario where $\boldsymbol{\theta}$ varies continuously. The duration of mode $m \in \mathbf{M}$ in scenario $s \in \mathbf{S}$ is denoted by $t_{s,m}$ whereas the parameter values are denoted by $\boldsymbol{\theta}_{s,m}$. $t_{s,m}$ and $\boldsymbol{\theta}_{s,m}$ are carefully chosen such that the piecewise constant function is a good approximation of the actual continuous profile (e.g., they have the same integral over time). **Figure 3-5** shows how daily profiles of solar irradiance can be approximated using two modes: a day mode with a positive constant irradiance and a night mode with zero irradiance.

The employment of a coarse time resolution may lead to deviations in the performance of the optimal process when actual profiles are used to check the quality of the approximation. System performance based on the original parameter data and the mode-based approximation are compared, post-optimization, using multiple scenarios. The approximation is valid if negligible differences are observed in important performance metrics. The validation procedure will be illustrated in the following case study section.

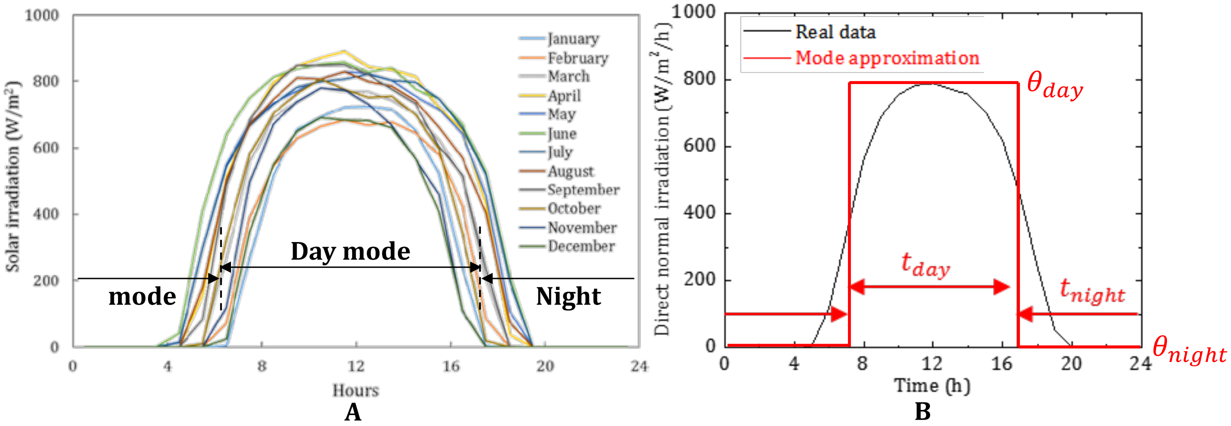

Figure 3-5. (A) Daily profiles of solar irradiance; (B) a mode-represented daily profiles using piecewise constant approximation.

3.3.2 Multimode superstructure generation

As opposed to traditional superstructure optimization, where units are selected for a single nominal operating mode, the proposed framework has two levels of structural decisions: (1) design decisions (unit *selection*) and (2) mode-specific operational decisions (unit *activation*). Among all potential units, a subset of units is *selected* to be installed, and among all selected units, a subset is *activated* during a mode.

To illustrate the concepts, we consider methanol production from solar energy in **Figure 3-6**. In the day mode, solar irradiance provides heat for H_2O and CO_2 splitting, which can take place in either a fluidized bed or a fixed bed reactor. The unreacted CO_2 is separated from CO using either membrane or distillation separation. To maintain 24-hour operation of the downstream methanol synthesis reactor, part of the produced syngas is stored in a tank for night use. In the night mode, the splitting reactor is shut down (i.e., no alternative reactors are activated) and the stored syngas is sent to the methanol synthesis reactor. If membrane separation is activated in the day mode, purified CO is stored and no CO_2/CO separation is needed in the night mode. However, if distillation is activated during the day, it has to be also activated during the night to prevent daily column startup and shutdown. In this case, CO_2/CO mixture is stored for night use without pre-separation. This example illustrates the necessity of considering different process flow sheets for each mode, as well as the interactions between unit activations across modes.

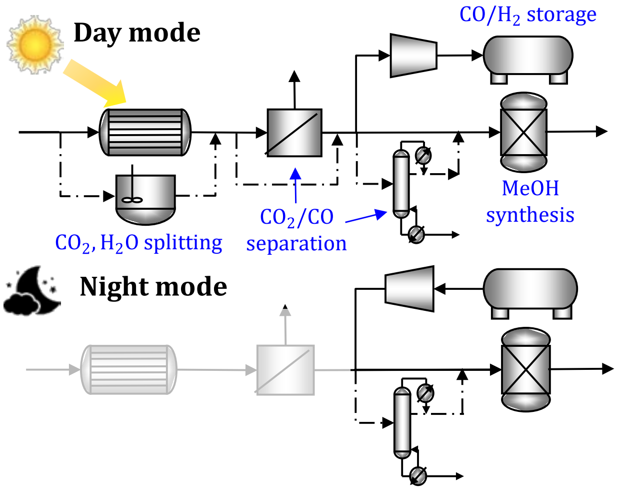

Figure 3-6. Multimode superstructure example: solar fuel production process with 2 modes. Streams connected to alternative reactor and separation units are shown in dashed lines.

The graphic representation of a general unit model, including all the relevant first and second stage variables, is illustrated in **Figure 3-7**. For the representation and modeling of the superstructure, we introduce three basic sets: (1) units, $i \in \mathbf{I}$; (2) streams $j \in \mathbf{J}$; and (3) components, $k \in \mathbf{K}$.

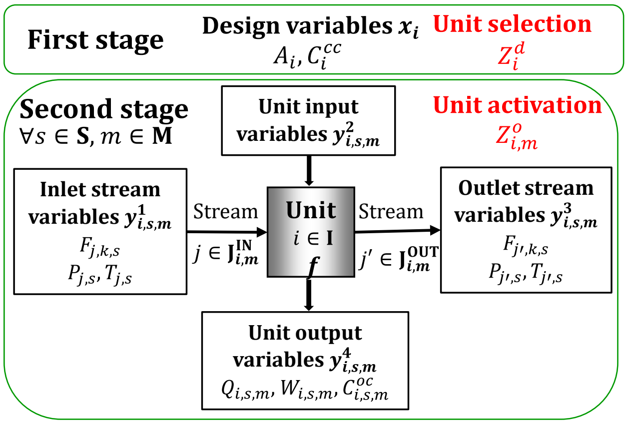

Figure 3-7. A general processing unit.

Binary variables Z_i^d denote the selection of unit *i* for the overall design, while binary variables $Z^o_{i,m}$ denote the activation of *i* in mode *m*. If *i* is not activated in *m* ($Z^o_{i,m} = 0$), all component flows of its inlet ($j \in \mathbf{J}^{\mathbf{IN}}_{i,m}$) and outlet streams ($j' \in \mathbf{J}^{\mathbf{OUT}}_{i,m}$) are forced to zero. Streams are indexed over (i, m) because different streams can connect to the same unit in different modes (e.g., the stream connections to the compressor in **Figure 3-6**). Unit *i* is selected if it is activated in any mode.

$$Z_i^d \geq Z^o_{i,m} \quad i \in \mathbf{I}, m \in \mathbf{M} \tag{3-3}$$

The unit operation over scenarios and modes can be formulated using a flow-based approach [127], in its general form, given as

$$(\boldsymbol{y}^3_{i,s,m}, \boldsymbol{y}^4_{i,s,m}) = f\left(\boldsymbol{y}^1_{i,s,m}, \boldsymbol{y}^2_{i,s,m}, , \boldsymbol{\theta}_{s,m}, t_{s,m}\right) \quad s \in \mathbf{S}, m \in \mathbf{M} \tag{3-4}$$

where $\boldsymbol{y}^1_{i,s,m}, \boldsymbol{y}^2_{i,s,m}$ are input operational variables and $\boldsymbol{y}^3_{i,s,m}, \boldsymbol{y}^4_{i,s,m}$ are output operational variables. Specifically, $\boldsymbol{y}^1_{i,s,m}$ are inlet stream variables (component flow rates $F_{j,k,s}$, stream temperatures $T_{j,s}$ and pressures $P_{j,s}$); $\boldsymbol{y}^2_{i,s,m}$ are unit input variables (e.g., distillation reflux ratio); $\boldsymbol{y}^3_{i,s,m}$ are outlet stream variables ($F_{j',k,s}, T_{j',s}, P_{j',s}$); and $\boldsymbol{y}^4_{i,s,m}$ are unit output variables (e.g., heating duty $Q_{i,s,m}$, work $W_{i,s,m}$ and operating cost $C^{oc}_{i,s,m}$). $C^{oc}_{i,s,m}$ includes a fixed part and a varying part given as follows

$$C^{oc}_{i,s,m} = f_i^{oc,fix}(Z^o_{i,m}) + f_i^{oc,vary}(Q_{i,s,m}, W_{i,s,m}) \;\; i \in \mathbf{I}, s \in \mathbf{S}, m \in \mathbf{M} \qquad (3\text{-}5)$$

While operational variables are different across scenarios and modes, design variables $\boldsymbol{x_i}$ (equipment size A_i, capital cost C_i^{cc}) are first stage decisions, that is, are common across scenarios and modes. To guarantee operational feasibility, the equipment size is chosen as the maximum required size ($A^o_{i,s,m}$) among all scenarios and modes:

$$A_i \geq A^o_{i,sm} = f_i^{sizing}(\boldsymbol{y^1_{i,s,m}}, \boldsymbol{y^2_{i,s,m}}, \boldsymbol{\theta_{s,m}}, t_{s,m}) \;\; i \in \mathbf{I}, s \in \mathbf{S}, m \in \mathbf{M} \qquad (3\text{-}6)$$

where f_i^{sizing} is the unit sizing function, carefully designed so that when unit inlet component flows are equal to zero, $A^o_{i,sm}$ is also equal to zero. In the sizing of equipment used for storing materials (i.e., storage tanks), durations $t_{s,m}$ also need to be considered.

The multimode superstructure can be generated based on any superstructure representation (e.g., STN, ETN, P-graph). Logic constraints that have been developed for conventional steady-state superstructure optimization are also applicable here using the design (unit selection) decisions. In addition, we introduce new types of logic constraints to describe the interactions between unit activations across modes. For example, a type of constraint is designed for units (e.g., distillation columns) which cannot be shutdown frequently (e.g., daily) during operation. This constraint ensures a unit being activated in all modes once it is selected, given as

$$Z_i^d = Z^o_{i,m} \;\; i \in \mathbf{I}, m \in \mathbf{M} \qquad (3\text{-}7)$$

Another type of constraint is applied when the activation of one unit i in one mode implies the activation of another unit i' in another mode. For example, if a storage tank is active in a mode, a compressor or pump should be active in the next mode for stored material discharging. An example of such constraint is:

$$Z^o_{i,m} - Z^o_{i',m+1} \leq 0 \;\; i, i' \in \mathbf{I}, m \in \mathbf{M} \tag{3-8}$$

3.3.3 Multimode stochastic programming model

The optimization problem is formulated as a two-stage stochastic programming model with mode subproblems inside each scenario, leading to a multimode stochastic programming model:

$$\begin{aligned}
&\min_{x} f^1(\boldsymbol{x}) + \textstyle\sum_s \pi_s \cdot Q_s\big(\boldsymbol{x}, \boldsymbol{\theta_{s,m}}, t_{s,m}\big)\\
&\qquad \boldsymbol{x} = [\,\boldsymbol{x}^{\mathbb{B}}, \boldsymbol{x}^{\mathbb{C}}], \boldsymbol{x}^{\mathbb{B}} \in \{0,1\}^{n1}\,,\;\; \boldsymbol{x}^{\mathbb{C}} \in \mathbf{R}^{n2}\\
&\qquad\quad Q_s = \min_{\boldsymbol{y_{s,m}}} f^2(\boldsymbol{x}, \boldsymbol{y_{s,m}}, \boldsymbol{\theta_{s,m}}, t_{s,m}) \qquad \forall\, s \in \mathbf{S}\\
&\qquad\quad \text{s.t.}\\
&\qquad\qquad \left.\begin{aligned}
h_{s,m}\big(\boldsymbol{x}, \boldsymbol{y_{s,m}}, \boldsymbol{\theta_{s,m}}, t_{s,m}\big) = 0\\
g_{s,m}\big(\boldsymbol{x}, \boldsymbol{y_{s,m}}, \boldsymbol{\theta_{s,m}}, t_{s,m}\big) \leq 0\\
r_{s,m}\big(\boldsymbol{x}, \boldsymbol{y_{s,m}}, \boldsymbol{\theta_{s,m}}, t_{s,m}, \boldsymbol{y_{s,m+1}}, \boldsymbol{\theta_{s,m+1}}, t_{s,m+1}\big) = 0\\
\boldsymbol{y_{s,m}} = \big[\,\boldsymbol{y^{\mathbb{B}}_{m}}, \boldsymbol{y^{\mathbb{C}}_{s,m}}\big], \boldsymbol{y^{\mathbb{B}}_{m}} \in \{0,1\}^{n3}\,, \boldsymbol{y^{\mathbb{C}}_{s,m}} \in \mathbf{R}^{n4}
\end{aligned}\right\}\;\forall\, m \in \mathbf{M}
\end{aligned} \tag{3-9}$$

where $\boldsymbol{x}$ are design variables, including discrete decisions $\boldsymbol{x}^{\mathbb{B}}$ (i.e., Z^d_i) and continuous decisions $\boldsymbol{x}^{\mathbb{C}}$ (i.e., A_i, C^{cc}_i); $\boldsymbol{y_{s,m}}$ are operational variables, including discrete decisions $\boldsymbol{y^{\mathbb{B}}_{m}}$ (i.e., $Z^o_{i,m}$) and continuous decisions $\boldsymbol{y^{\mathbb{C}}_{s,m}}$ (i.e., $\boldsymbol{y^1_{i,s,m}}, \boldsymbol{y^2_{i,s,m}}, \boldsymbol{y^3_{i,s,m}}, \boldsymbol{y^4_{i,s,m}}$);$h_{s,m}$ are equality constraints (e.g., unit mass and energy balance, unit connectivity); $g_{s,m}$ are inequality constraints including equipment sizing equations (eqn (3-6)) and design specifications; and $r_{s,m}$ are coupling constraints (e.g., storage or inventory level tracking) that connect the operation across modes. Note that the stochastic programming formulation exhibits a nested block diagonal structure (see **Figure 3-8**). Inside the block of each scenario, blocks of modes are linked through coupling constraints.

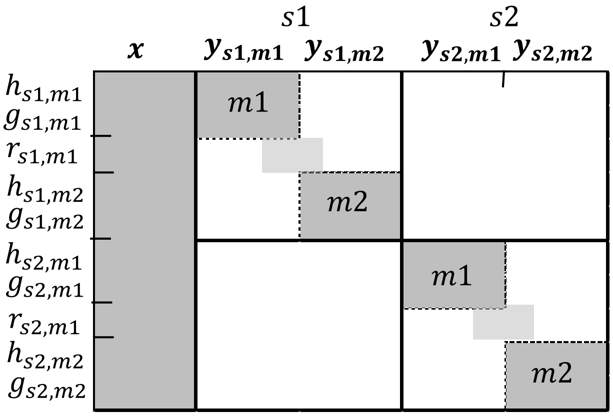

Figure 3-8. The nested block diagonal structure of the multimode stochastic model (illustrated with two modes and two scenarios).

3.3.4 Propagation-based bound generation

To enhance the computational performance of the resulting MINLP model, we develop a constraint propagation algorithm (see **Figure 3-9**) for the calculation of lower and upper bounds on both first stage design variables $\boldsymbol{x}$ and second stage operational variables $\boldsymbol{y}_{\boldsymbol{s},\boldsymbol{m}}$. The propagation starts from initial bounds on a set of variables, which are usually given as feed, demand and unit specifications. Bounds on feed and demand stream variables (e.g., component flowrates) are scenario/mode specific second stage information; while specifications regarding first stage unit decisions should be satisfied in all scenarios and modes. For convenience, we use $\underline{X}/\overline{X}$ to denote the lower/upper bound on variable X.

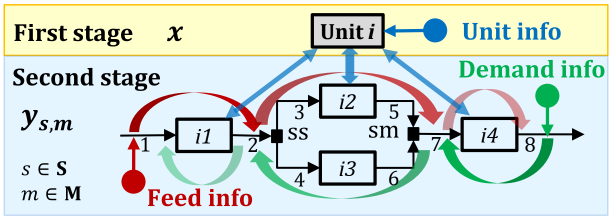

Figure 3-9. Bound propagation for two-stage multimode stochastic model. Circles are three information sources and colored arrows are corresponding information flows including forward propagation (red), backward propagation (green), and information exchange between 1st and 2nd stage (blue).

The *direction* of the propagation algorithm depends on the type of available information. If specifications on feed stream flowrates are given, bounds on downstream flowrates can be calculated sequentially through forward propagation, that is, calculate bounds on $\boldsymbol{y}_{\boldsymbol{i,s,m}}^{\boldsymbol{3}}, \boldsymbol{y}_{\boldsymbol{i,s,m}}^{\boldsymbol{4}}$ from bounds on $\boldsymbol{y}_{\boldsymbol{i,s,m}}^{\boldsymbol{1}}, \boldsymbol{y}_{\boldsymbol{i,s,m}}^{\boldsymbol{2}}$ utilizing the unit model (see **Figure 3-7**). Specifically, for every unit i, the tightest possible bounds on all involved operational variables $\boldsymbol{y}_{\boldsymbol{i,s,m}}$ based on given bounds ($\underline{\boldsymbol{y}}_{\boldsymbol{i,s,m}}/\overline{\boldsymbol{y}}_{\boldsymbol{i,s,m}}$) can be obtained by solving the following optimization problems for each variable individually, where $y_{i,s,m}^{(k)}$ is the k^{th} element of $\boldsymbol{y}_{\boldsymbol{i,s,m}}$ ($k = 1,2, \dots, n$).

$$
\begin{aligned}
&\min/\max y_{i,s,m}^{(k)} \qquad \forall\, i \in \mathbf{I}, s \in \mathbf{S}, m \in \mathbf{M} \\
&\text{s.t.} \quad f\left(\boldsymbol{y}_{\boldsymbol{i,s,m}}, \boldsymbol{\theta}_{\boldsymbol{s,m}}, t_{s,m}\right) = 0 \\
&\qquad \underline{\boldsymbol{y}}_{\boldsymbol{i,s,m}} \le \boldsymbol{y}_{\boldsymbol{i,s,m}} \le \overline{\boldsymbol{y}}_{\boldsymbol{i,s,m}} \\
&\qquad \boldsymbol{y}_{\boldsymbol{i,s,m}} = \left[\boldsymbol{y}_{\boldsymbol{i,s,m}}^{\boldsymbol{1}}, \boldsymbol{y}_{\boldsymbol{i,s,m}}^{\boldsymbol{2}}, \boldsymbol{y}_{\boldsymbol{i,s,m}}^{\boldsymbol{3}}, \boldsymbol{y}_{\boldsymbol{i,s,m}}^{\boldsymbol{4}}\right], \boldsymbol{y}_{\boldsymbol{i,s,m}} \in \mathbb{R}^n
\end{aligned}
\tag{3-10}
$$

The solution of the min/max problem yields $\underline{y}_{i,s,m}^{(k)}/\overline{y}_{i,s,m}^{(k)}$ respectively.

Similarly, if bounds on demand stream flowrates are given, we can calculate other flow rate bounds moving upstream through backward propagation (i.e., assigning bounds on $\boldsymbol{y}_{\boldsymbol{i,s,m}}^{\boldsymbol{1}}, \boldsymbol{y}_{\boldsymbol{i,s,m}}^{\boldsymbol{2}}$ from bounds on $\boldsymbol{y}_{\boldsymbol{i,s,m}}^{\boldsymbol{3}}, \boldsymbol{y}_{\boldsymbol{i,s,m}}^{\boldsymbol{4}}$). When there are loops (i.e., recycle streams) in the process, tear streams are used together with the forward/backward propagation algorithms [153].

In our superstructure modeling, we use selection splitter (ss)/selection mixer (sm) to divide/combine the inlet/outlet streams of alternative units, respectively (see **Figure 3-9**). Since ss/sm are not actual splitter/mixer (i.e., only one unit intlet/outlet stream exists in the solution), special considerations are needed when propagating through them. In backward propagation, the upper bounds on outlet streams of all units connecting to sm are equal to the upper bound on the outlet stream of sm, while the lower bounds on all unit outlet streams are zero. This can be illustrated using the example in **Figure 3-9**,

$$\bar{F}_{5,k,s} = \bar{F}_{6,k,s} = \bar{F}_{7,k,s} \quad k \in \mathbf{K}, s \in \mathbf{S} \tag{3-11}$$

$$\underline{F}_{5,k,s} = \underline{F}_{6,k,s} = 0 \quad k \in \mathbf{K}, s \in \mathbf{S} \tag{3-12}$$

For an ss, the upper bound on its inlet stream is the maximum among the upper bounds on inlet streams of all units connecting to this ss.

$$\bar{F}_{2,k,s} = \max(\bar{F}_{3,k,s}, \bar{F}_{4,k,s}) \quad k \in \mathbf{K}, s \in \mathbf{S} \tag{3-13}$$

Let $\tilde{F}_{j,k,s}$ be the minimum flow of component k along stream j in scenario s, if the stream is active in (s, m). The lower bound on the inlet stream of ss is given as follows:

$$\underline{F}_{2,k,s} = \min(\tilde{F}_{3,k,s}, \tilde{F}_{4,k,s}) \quad k \in \mathbf{K}, s \in \mathbf{S} \tag{3-14}$$

After bounds on all $\boldsymbol{y}_{\boldsymbol{s},\boldsymbol{m}}$ are calculated, bounds on required unit sizes ($A^{o}_{i,s,m} = f_i^{sizing}(\boldsymbol{y}_{\boldsymbol{i},\boldsymbol{s},\boldsymbol{m}})$) in all scenarios/modes are calculated and used to calculate bounds on first stage unit sizes (A_i),

$$\bar{A}_i = \underset{s,m}{max}\, \bar{A}^{o}_{i,s,m} \quad i \in \mathbf{I}, s \in \mathbf{S}, m \in \mathbf{M} \tag{3-15}$$

$$\underline{A}_i = \underset{s,m}{max}\, \underline{A}^{o}_{i,s,m} \quad i \in \mathbf{I}, s \in \mathbf{S}, m \in \mathbf{M} \tag{3-16}$$

Alternatively, if first stage unit information is given for unit *i*, bounds on its design variables are used to tighten bounds on its operational variables. For example, bounds on reactor sizes and reaction information (e.g. kinetics), can be used to derive bounds on effluent flow rates.

If multiple specifications or externally provided bounds are available, we use our propagation algorithms from different starting points and towards different *directions*. This process continues until no more variable bounds can be updated. The bound propagation algorithm described in this section will be further illustrated in the case study.

3.4 Case study

We apply the proposed framework to concentrating solar power (CSP) plants with thermochemical energy storage (TCES). CSPs convert sunlight to heat, which then drives a turbine to generate electricity. Using heat as an intermediate, rather than converting sunlight directly to electricity as in photovoltaics (PV), CSP can incorporate efficient and low cost thermal energy storage (TES) for night power generation [11]. Thermochemical energy storage reversibly converts solar-heat to chemical energy, offering high energy density and low heat loss over long periods. CSP plants with TCES have the potential for grid-scale dispatchable solar power generation.

A deterministic optimization model for the design of general CSP+TCES processes has been developed and used to analyze the performance of multiple TCES technologies [168]. Building upon that work, which employed annual average solar irradiance, we consider the seasonal and daily variability in solar irradiance using the proposed framework. Moreover, we present a new reactor configuration which allows more efficient steam generation from the heat of the exothermic reaction. The process flow sheet of CSP plants employing TCES is shown in **Figure 3-10**. The plant comprises four subsystems, the solar field (i.e., collector), receiver, TCES and turbine. Note that different process configurations are adopted in day and night modes.

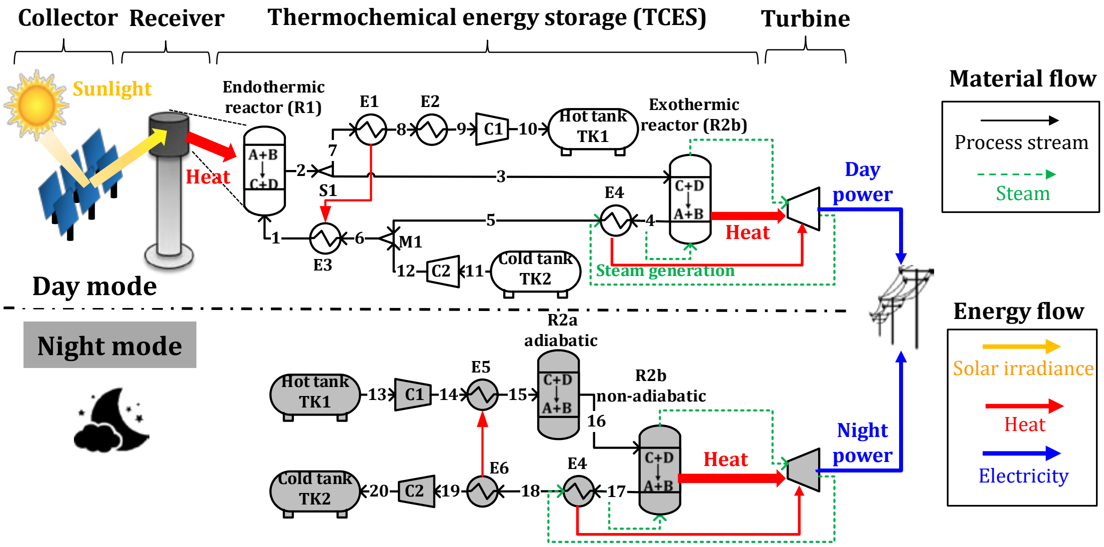

Figure 3-10. Process flowsheet of CSP plants with fluid phase TCES systems (day and night modes).

During the day, a large field of mirrors focuses sunlight onto the receiver, on top of a tower, where the concentrated sunlight drives an endothermic reaction $(A + B \rightarrow C + D)$ in reactor R1. A fraction of the effluent is cooled down and stored in storage tank TK1 while the remaining fraction is sent to reactor R2b, where the reverse exothermic reaction $(C + D \rightarrow A + B)$ takes place and the reaction heat is used to generate steam for daytime power production.

During the night, the collector, receiver and R1 are deactivated, while reactor system R2 and the turbine run at a steady state, which can be different from daytime. Products stored in TK1 are preheated and sent to reactor system R2, which consists of (1) an adiabatic stage (only activated during the night), R2a, where the heat of exothermic reaction further increases the temperature of stream 16; and (2) a non-adiabatic stage, R2b, where the reaction heat is used for steam generation. This two-stage reactor configuration can achieve both high steam temperature and low equilibrium temperature of the exothermic reaction (illustrated in **Figure 3-16**B).

3.4.1 Scenario and mode generation

We chose Daggett in southern California (34.87°N, 116.78°W) as the CSP plant site and obtain its typical meteorological year (TMY) data, that is, the standard hourly direct normal irradiance (DNI) in a 1-year period, from the National Solar Radiation Data Base [169]. Following the procedure described in the previous section, we generate six scenarios, each with two modes. In the mode generation, the constant DNI in the day mode is equal to the daily maximum DNI (**Figure 3-11**A). The duration of the day mode is chosen to ensure the mode profile and continuous profile have the same daily solar energy (integral over time). The duration, DNI and occurrence frequency of all scenarios and modes are shown in **Table 3-1**.

Table 3-1. Duration, DNI and occurrence frequency of all scenarios and modes.

Scenario	Duration (hours)		DNI (W/m^2)		Occurrence
	Day	Night	Day	Night	
s1	3.9	20.1	273	0	4.4%
s2	5.2	18.8	598	0	8.2%
s3	6.8	17.2	747	0	11.0%
s4	7.8	16.2	895	0	24.1%
s5	9.6	14.4	938	0	30.7%
s6	11.1	12.9	973	0	21.6%

The replacement of the hourly time-step profiles with day and night modes using a piecewise constant approximation (**Figure 3-11**A) is valid because the two lead to similar results. For example, although the approximation through modes leads to a different total flow to the storage tank, the difference in the storage tank pressure and compression power, which ultimately affects the performance of the system, is negligible (**Figure 3-11**C).

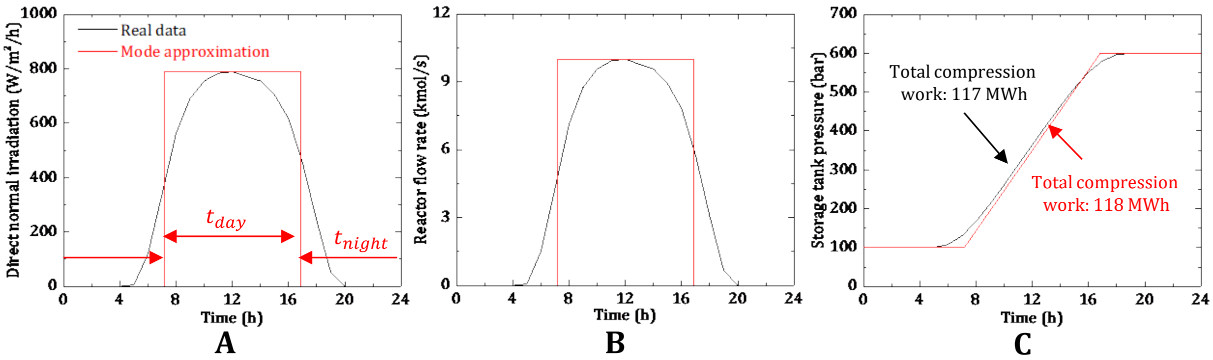

Figure 3-11. Comparison of mode approximation (red) and hourly data (black). (A) DNI (W/m^2), (B) flow delivered to storage tank (kmol/s) and (C) storage tank pressure (bar) during charging and the required compression power (MWh).

3.4.2 CSP plant models

Our objective is to minimize the overall levelized cost of electricity (LCOE) of the CSP plant. We specify the plant nameplate capacity as 100 MW to avoid the trivial solution ($\boldsymbol{x} = \mathbf{0}$). The first stage design variables ($\boldsymbol{x}$) include solar field area ($AREA$), receiver size (Q^r) and TCES equipment sizes (A_i). The second stage operational variables ($\boldsymbol{y_{s,m}}$) include turbine output levels ($P_{s,m}$), stream flow rates ($F_{j,k,s}$) and unit operating conditions ($P_{i,s,m}, T_{i,s,m}, Q_{i,s,m}, W_{i,s,m}$). Equality constraints arise from the physical model of the subsystems (i.e., collector, receiver and turbine), unit mass and energy balances, as well as cost calculations. Inequality constraints arise from equipment sizing and design specifications. Coupling constraints across modes arise from the material balances around storage tanks (TK1, TK2), which ensure the same amount of products are added and removed across modes within each scenario. The parameters include reaction properties, plant characteristics and cost assumptions.

Energy flows and interactions between the four subsystems are shown in **Figure 3-12**. In the following subsections, we present models for each subsystem and the objective function, LCOE.

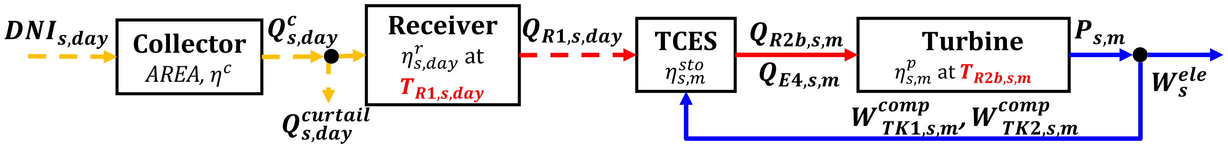

Figure 3-12. Energy flows in CSP plants. (yellow: solar energy, red: thermal energy, blue: electricity; dash line: daytime operation; solid line: 24-hour continuous operation).

Collector and receiver

Given the direct normal irradiance ($DNI_{s,day}$) and the solar field area ($AREA$), solar energy collected by the solar field ($Q^c_{s,day}$) in each scenario is calculated as,

$$Q^c_{s,day} = AREA \cdot DNI_{s,day} \cdot \eta^c \quad s \in \mathbf{S} \tag{3-17}$$

where $\eta^c = 0.6$ is the collector efficiency (constant). The model can readily handle the variability in η^c by simply treating the product of DNI and η^c as the varying parameter."

The heat absorbed by R1 ($Q_{R1,s,day}$) is given as

$$Q_{R1,s,day} = (\, Q^c_{s,day} - Q^{curtail}_{s,day}) \cdot \eta^r_{s,day} \quad s \in \mathbf{S} \tag{3-18}$$

where $Q^{curtail}_{s,day}$ is the energy curtailed through heliostat defocus to prevent receiver from overheating in extremely sunny days; $\eta^r_{s,day}$ is the receiver efficiency (variable), which is a function of endothermic reaction temperature ($T_{R1,\mathrm{s,day}}$) [96]. Higher $T_{R1,\mathrm{s,day}}$ leads to greater radiation and convection losses and thus lower $\eta^r_{s,day}$.

TCES system

To model the TCES subsystem, we define subsets for the four types of units in TCES: reactors ($\mathbf{I^R}$), storage tanks ($\mathbf{I^{TK}}$), compressors ($\mathbf{I^C}$), and heat exchangers ($\mathbf{I^E}$). Based upon flow-based formulations of general processing units, we develop models for each type of TCES units.

Reactor. Reactors are the key components of the TCES subsystem. **Figure 3-13** shows the related process variables and parameters for a general reactor ($i \in \mathbf{I^R}$). The reversible reaction is expressed in a general form $v_A A + v_B B \leftrightarrow v_C C + v_D D$. In this case study, methane dry reforming $CH_4 + CO_2 \leftrightarrow 2CO + 2H_2$ is used, with its reaction enthalpy (ΔH), entropy (ΔS), and component heat capacity (Cp_k) given as parameters. Equilibrium reactors are assumed and the reactor heat duty ($Q_{i,s,m}$) is equal to the enthalpy difference between its outlet and inlet stream, resulting from both component and temperature changes,

$$Q_{i,s,m} = \frac{\Delta H}{v_A} \cdot \left(F_{OUT,A,s} - F_{IN,A,s}\right) + \left(T_{OUT,s} - T_{IN,s}\right) \cdot \left(\sum\nolimits_k F_{IN,k,s} \cdot Cp_k\right) \quad i \in \mathbf{I^R}, s \in \mathbf{S}, m \in \mathbf{M} \tag{3-19}$$

where $F^T_{IN,s}$ and $F^T_{OUT,s}$ are total molar flow rates of inlet and outlet streams, $F_{IN,k,s}$ and $F_{OUT,k,s}$ are component flow rates.

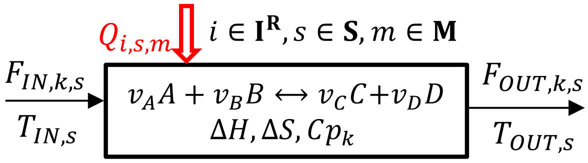

Figure 3-13. A general reaction unit.

Storage and compression. The dynamic charging and discharging of TK1 in the course of the day (24 h) is illustrated in **Figure 3-14**. When products are charging into TK1 during the day mode, tank pressure increases from $P^L_{TK1,s}$ to $P^H_{TK1,s}$. When products are discharging from TK1 during the night mode, tank pressure decrease from$P^H_{TK1,s}$ to $P^L_{TK1,s}$. The material balance around TK1 is given as,

$$F^T_{IN,s} \cdot t_{s,day} = F^T_{OUT,s} \cdot t_{s,night} \quad s \in \mathbf{S} \tag{3-20}$$

The tank pressures depends on the storage tank size (V^{tank}_{TK1}) and the amount of stored products,

$$P^H_{TK1,s} - P^L_{TK1,s} = F^T_{IN,s} \cdot t_{s,day} \cdot R \cdot T_{IN,s} / V^{tank}_{TK1} \quad s \in \mathbf{S} \tag{3-21}$$

Compression is needed during the charging phase (2) when tank pressure exceeds TCES process pressure (P^{TCES}) and the discharging phase (4) after tank pressure drops below P^{TCES}. In **Figure 3-14**B, the blue line shows how compression power varies with time. Points A and B are compression power peaks during phase (4) and (2) respectively. The compressor rated power of C1 (PWR_{C1}) is the maximum power required between these two peaks among all scenarios,

$$PWR_{C1} = \max_{s} \left\{ FCp_{IN,s} \cdot T_{IN,s} \cdot [\left(\frac{P^{H}_{TK1,s}}{P^{TCES}}\right)^{\frac{\gamma-1}{\gamma}} - 1]/\eta^{comp}; FCp_{OUT,s} \cdot T_{OUT,s} \cdot [\left(\frac{P^{TCES}}{P^{L}_{TK1,s}}\right)^{\frac{\gamma-1}{\gamma}} - 1]/\eta^{comp} \right\} \quad s \in \mathbf{S} \tag{3-22}$$

where $FCp_{IN,s}$ is the inlet flow heat capacity, γ is the heat capacity ratio, and η^{comp} is the compressor isentropic efficiency. The max function is reformulated in the model implementation.

Electricity consumed by C1 during the day ($W^{comp}_{TK1,s,day}$) and night ($W^{comp}_{TK1,s,night}$) are derived by integrating the compressor power over time.

The above calculations show that smaller V^{tank}_{TK1} leads to larger $P^{H}_{TK1,s} - P^{L}_{TK1,s}$ and thus higher compressor cost and electricity cost. In this model, the storage tank sizes and compression strategy are simultaneously optimized considering the trade-offs between storage cost and compression cost.

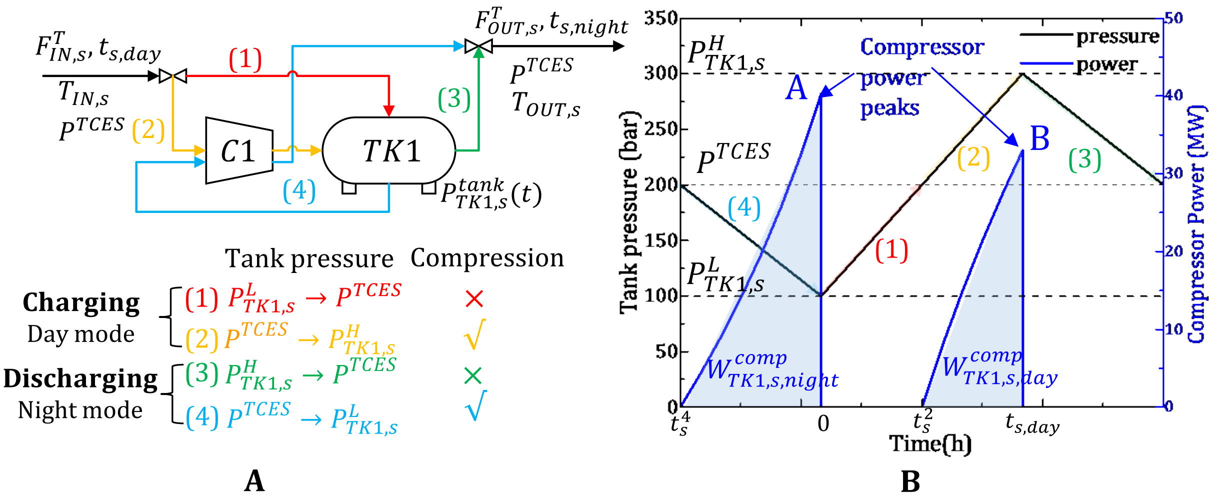

Figure 3-14. (A) Charging and discharging process of TK1 inside a day; (B) daily profile of storage tank pressure and compressor power.

Heat exchanger and steam generation. Reactions occur at high temperature while gaseous reaction products are stored at relatively low temperature to reduce the gas storage volume. To reduce utility usage, hot reactor effluents are used to preheat cold reactor feed streams in heat-exchangers (E1-E3 for R1 and E5-E6 for R2 system). The effluent of R1 can be further cooled down by cold utilities in cooler E2. The effluent of R2b can be further cooled down by preheating the turbine feed water in cooler E4. The synthesis of the heat exchange network, which accounts for the heat exchanger cost, gas storage cost and cooling utility cost, is solved simultaneously with the process design problem.

Exothermic reaction heat and sensible heat of R2b inlet stream are used to generate superheated steam for the turbine in R2b and E4, respectively (see **Figure 3-15**). The overall energy balance for steam generation is,

$$-Q_{R2b,s,m} - Q_{E4,s,m} = F_{s,m}^{steam} \cdot (h_{PRE}^{steam} + h_{EVAP}^{steam} + h_{SUPER,s,m}^{steam}) \quad s \in \mathbf{S}, m \in \mathbf{M} \tag{3-23}$$

where $F_{s,m}^{steam}$ is the steam flow rate; h_{PRE}^{steam}, h_{EVAP}^{steam} and $h_{SUPER,s,m}^{steam}$ are the heat (per mole) to preheat, evaporate and superheat steam. Given the fixed steam pressure (12.5 MPa) and feed water temperature (T_{IN}^{steam} =40°C), h_{PRE}^{steam} and h_{EVAP}^{steam} are pre-calculated parameters, while $h_{SUPER,s,m}^{steam}$ is a function of the steam outlet temperature ($T_{OUT,s,m}^{steam}$),

$$h_{SUPER,s,m}^{steam} = Cp_{SUPER}^{steam} \cdot \left(T_{OUT,s,m}^{steam} - T_{SAT}^{steam}\right) \quad s \in \mathbf{S}, m \in \mathbf{M} \tag{3-24}$$

where Cp_{SUPER}^{steam} is the heat capacity of the superheated steam and $T_{SAT}^{steam} = 328℃$ is the temperature of the saturated steam at 12.5 MPa.

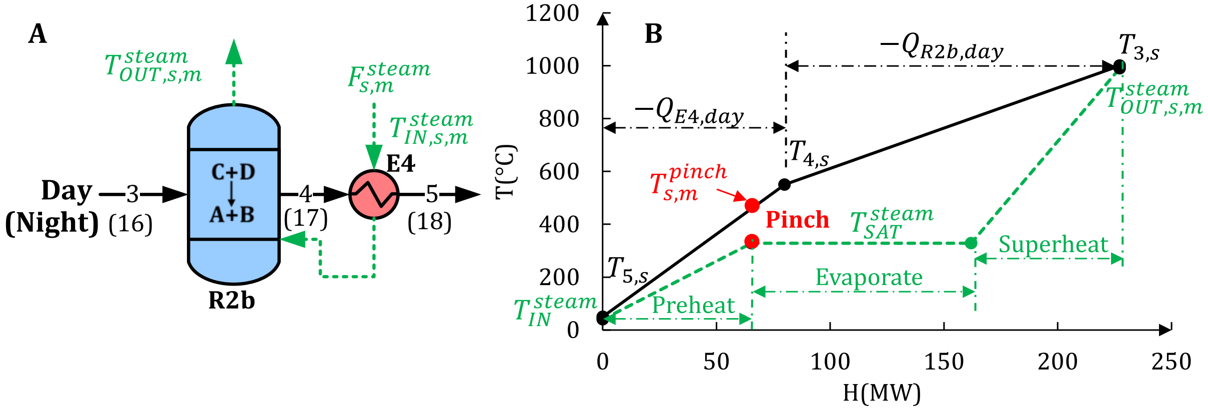

Figure 3-15. (A) Steam generation process and (B) the composite curve.

In addition, we use constraints tailored to prevent violation of the second law of thermodynamics during steam generation. Although steam is generated at different conditions during the day and night modes, the same types of constraints are applied. Here, we use steam generation in the day mode for illustration. The inlet and outlet temperature difference between process streams and the steam stream should be greater than the minimum approach temperature ΔT_{min} (10 °C),

$$T_{5,s} - T_{IN}^{steam} \geq \Delta \mathrm{T_{min}};\ T_{3,s} - T_{OUT,s,day}^{steam} \geq \Delta T_{min} \quad s \in \mathbf{S} \tag{3-25}$$

Figure 3-15B shows that a potential pinch location exists in the composite curve at the end of steam preheating. On the cold composite curve (steam), the enthalpy and temperature of this point is $F_{s,day}^{steam} \cdot h_{PRE}^{steam}$ and T_{SAT}^{steam}; while on the hot composite curve (process stream), the temperature corresponding to this enthalpy value ,$T_{s,day}^{pinch}$, can be determined by interpolation between $T_{5,s}$ and $T_{4,s}$ (when $F_{s,day}^{steam} \cdot h_{PRE}^{steam} \leq -Q_{E4,\mathrm{s,day}}$) or between $T_{4,s}$ and $T_{3,s}$ (when $F_{s,day}^{steam} \cdot h_{PRE}^{steam} \geq -Q_{E4,\mathrm{s,day}}$).

To ensure feasible heat transfer (i.e., hot and cold composite curves do not cross), we introduce the following constraint:

$$\frac{F_{s,day}^{steam} \cdot h_{PRE}^{steam}}{-Q_{E4,\mathrm{s,day}}} \cdot (T_{4,s} - T_{5,s}) + T_{5,s} \geq T_{SAT}^{steam} + \Delta T_{min} \; s \in \mathbf{S} \tag{3-26}$$

When $T_{s,day}^{pinch}$ is between $T_{5,s}$ and $T_{4,s}$, the left hand side of eqn (3-26) equals to $T_{s,day}^{pinch}$. This constraint enforces the temperature difference between $T_{s,day}^{pinch}$ and T_{SAT}^{steam} being greater than ΔT_{min}. When $T_{s,day}^{pinch}$ is between $T_{4,s}$ and $T_{3,s}$, hot and cold composite curves will never cross because the lower bound on $T_{4,s}$, specified based on the catalyst operating temperature range, is higher than $T_{SAT}^{steam} + \Delta T_{min}$. In this case, eqn (3-26) is always satisfied given that

$$\frac{F_{s,day}^{steam} \cdot h_{PRE}^{steam}}{-Q_{E4,\mathrm{s,day}}} \cdot (T_{4,s} - T_{5,s}) + T_{5,s} \geq T_{s,day}^{pinch} \geq T_{4,s} \geq T_{SAT}^{steam} + \Delta T_{min} \; s \in \mathbf{S}, m \in \mathbf{M} \tag{3-27}$$

TCES overview. In summary, the TCES subsystem (**Figure 3-10**) consists of a non-storage loop (stream 1-6) for daytime power generation, and a storage loop for nighttime power generation. In the day mode, stream 5 from the non-storage loop and and stream 12 from the storage loop combine in mixer m1, receive process heat and solar heat from E3 and R1, and then resplit into stream 3 (non-storage loop) and 7 (storage loop) with corresponding split fractions ζ_{nonsto} and ζ_{sto}. Stream 3 directly delivers heat to the turbine in R2b and E4, while stream 7 is cooled down and stored for the night use.

An X-T diagram (**Figure 3-16**) is used to illustrate the stream conditions (points) and unit operations (arrows connecting the points of its inlet and outlet streams) in these two loops. Heat exchangers are shown as horizontal arrows since this operation only changes the temperature (T) but not the composition (X) of its inlet stream. Reactor arrows can point in both T and X directions but cannot cross over the reaction equilibrium line. Heat duty of each unit ($Q_{i,s,m}$) is the enthalpy difference between its outlet and inlet streams (eqn (3-19)). The overall energy balances of non-storage and storage loops are given as follows, respectively,

$$-Q_{R2b,s,day} - Q_{E4,\mathrm{s,day}} = \zeta_{nonsto} \cdot (Q_{E3,\mathrm{s,day}} + Q_{R1,\mathrm{s,day}}) \quad s \in \mathbf{S} \tag{3-28}$$

$$-Q_{R2b,s,night} - Q_{E4,\mathrm{s,night}} = \zeta_{sto} \cdot \left(Q_{E3,\mathrm{s,day}} + Q_{R1,\mathrm{s,day}}\right) + Q_{E1,\mathrm{s,day}} + Q_{E2,\mathrm{s,day}} \quad s \in \mathbf{S} \tag{3-29}$$

Note that if the effluent of R1 is split evenly to the two loops ($\zeta_{nonsto} = \zeta_{sto} = 0.5$), the heat delivered to the turbine in the day mode ($-Q_{R2,\mathrm{s,day}} - Q_{E4,\mathrm{s,day}}$) is significantly higher than that delivered in the night mode. This is because that the sensible energy (high T) of stream 7 is consumed in cooler E1 and E2 and only its chemical energy (i.e., low x_{CH_4}) is stored for the night use. Moreover, extra compression power is required for gas storage, which makes the storage loop less energy efficient.

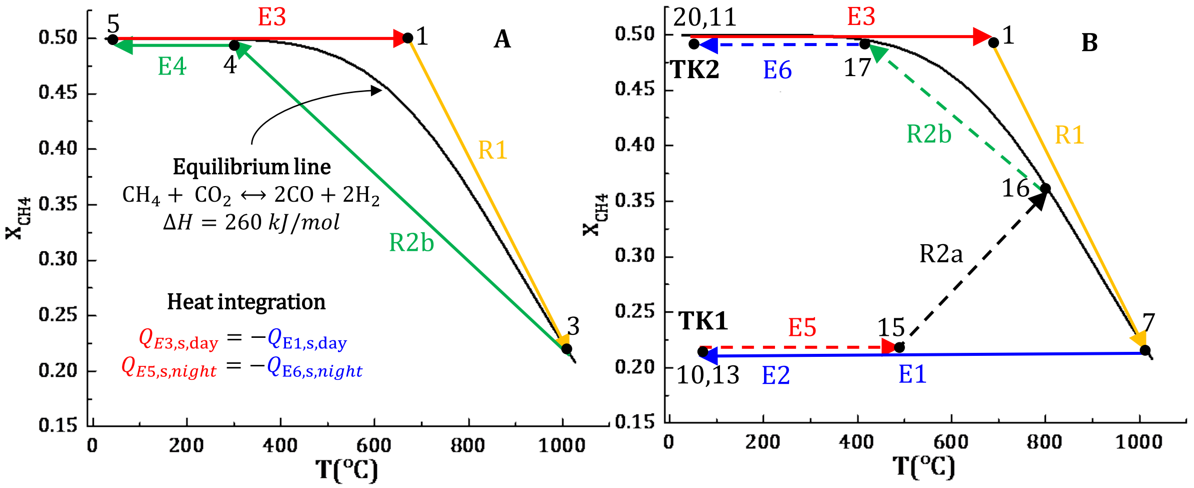

Figure 3-16. X-T diagram of the TCES subsystem: (A) non-storage loop (B) storage loop. Point: stream condition; arrow: unit operation (Heat exchangers between process streams, red: heating side, blue: cooling side; yellow: units with solar energy input; green: units with heat output for steam generation; black: adiabatic units. Solid arrow: daytime operation; dashed arrow: nighttime operation).

Turbine and part-load conditions

The steam turbine performance at rated ($P^{rate} = 100\ MW$) and part-load conditions is simulated using a rigorous Rankine cycle model [170]. At rated output, simulation results of turbine efficiency ($\eta^{p,rate}$) at different steam temperatures are shown in **Figure 3-17**A. It can be seen that $\eta^{p,rate}$ depends linearly on T_{OUT}^{steam} and this correlation can be fitted by linear regression,

$$\eta_{s,m}^{p,rate} = 1.55 \times 10^{-4}\ T_{OUT,s,m}^{steam} + 0.34 \quad s \in \mathbf{S}, m \in \mathbf{M} \tag{3-30}$$

The steam turbine can also operate at part-load conditions using the sliding pressure method [171]. Turbine (part-load) efficiency ($\eta_{s,m}^{p}$), defined as the ratio of the generated power to the turbine input heat load, reduces as the power output level ($P_{s,m}$) deviates from the nominal full load condition

$$\eta_{s,m}^{p} = P_{s,m}/\eta^{para}/\left(-Q_{R2,s,m} - Q_{E4,s,m}\right) \quad s \in \mathbf{S}, m \in \mathbf{M} \tag{3-31}$$

where $\eta^{para} = 0.9$ is the parasitic efficiency.

Simulation data (**Figure 3-17**B) shows that $\eta^{p}_{s,m}$ depends on $P_{s,m}$ in a non-linear way, but the input heat load presents a nearly linear relation with $P_{s,m}$. Assuming a 5% efficiency reduction at 50% load level, we derive the linear relation between the input heat load and $P_{s,m}$,

$$-Q_{R2,s,m} - Q_{E4,s,m} = (\frac{18}{19}P_{s,m} + \frac{1}{19}P^{rate})/\eta^{para}/\eta^{p,rate}_{s,m} \quad s \in \mathbf{S}, m \in \mathbf{M} \qquad (3\text{-}32)$$

By substituting eqn (3-32) into eqn (3-31), we calculate $\eta^{p}_{s,m}$ based on this linear approximation,

$$\eta^{p}_{s,m} = \eta^{p,rate}_{s,m}/(\frac{18}{19} + \frac{1}{19}\frac{P^{rate}}{P_{s,m}}) \quad s \in \mathbf{S}, m \in \mathbf{M} \qquad (3\text{-}33)$$

From **Figure 3-17**B, we can see the calculated $\eta^{p}_{s,m}$ (black line) fits well with the simulation data (black squares). Thus, eqns (3-30) and (3-32) are used to describe the turbine performance.

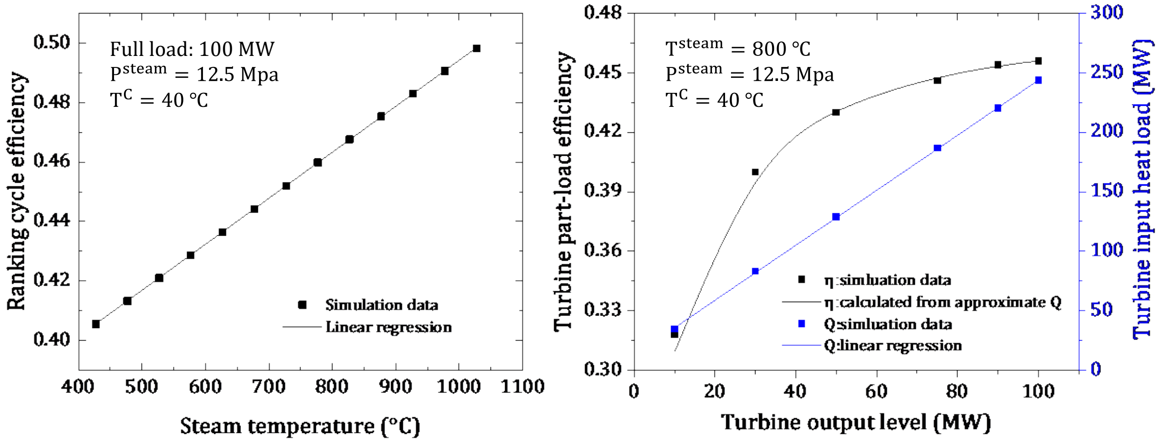

A

B

Figure 3-17. (A) Turbine full load efficiency as a function of steam temperature (B) turbine performance at part-load conditions.

Electricity generation and cost calculation

The total capital cost of the CSP plant (*CAPEX*) consists of the costs of four subsystems and depends only on the first stage design variables. The cost of the TCES subsystem includes equipment cost and the storage material cost, which is accounted as working capital with a cost factor of 0.15. The second stage operational costs ($OPEX_{s,m}$) account for the cooling utility cost and the operation and maintenance cost.

The daily net electricity output of the CSP plant in each scenario is given as,

$$W_s^{ele} = \sum_m (P_{s,m} \cdot t_{s,m} - W_{TK1,s,m}^{comp} - W_{TK2,s,m}^{comp}) \quad s \in \mathbf{S} \tag{3-34}$$

Finally, the objective function, the overall levelized cost of electricity (LCOE), is

$$\min LCOE = (CAPEX \cdot CRF + \sum_s \pi_s \cdot \sum_m OPEX_{s,m})/(365 \cdot \sum_s \pi_s \cdot W_s^{ele}) \tag{3-35}$$

where CRF is the capital recovery factor used to calculate the annual capital cost. Assuming a 9% interest rate and 30 years plant operation, $CRF = 0.1$.

3.4.3 Problem-specific bound generation

We apply the propagation algorithm described in the previous section to generate variable bounds. The three types of given information (feed, demand, unit) and propagation directions (forward, backward, exchange between two stages) are shown in Figure 3-18.

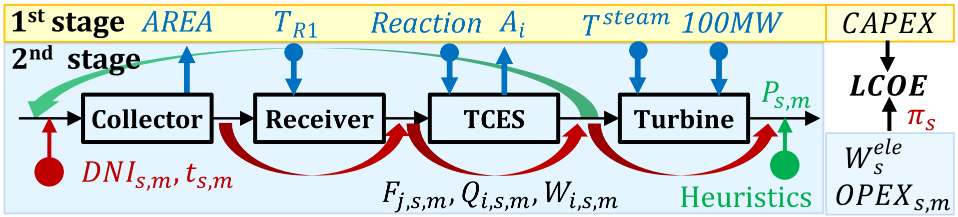

Figure 3-18. Bound propagation for case study.

The parameters we use for propagation include the fixed turbine capacity (100 MW) and the solar conditions ($DNI_{s,m}, t_{s,m}$). To calculate bounds on the received solar energy ($Q_{s,day}^{in} = AREA \cdot DNI_{s,day} \cdot \eta^c - Q_{s,day}^{curtail}$), we need bounds on collector area ($AREA$), which can be calculated as follows. Based on the operation of two existing CSP plants, Gemasolar [172] and Cresent Dunes [173], in the very sunny days, CSP plants maintain 24-hour full-load ($P_{s6,day} = P_{s6,night} = 100\ MW$)

with, potentially, solar energy curtailment. Thus, $\underline{AREA}$ is calculated through backward propagation assuming that no curtailment is needed,

$$\underline{AREA} = \left(\frac{P_{s6,day}}{\bar{\eta}^{p}_{s6,day} \cdot \bar{\eta}^{sto}_{s6,day} \cdot \eta^{para}} + \frac{P_{s6,night}}{\bar{\eta}^{p}_{s6,night} \cdot \bar{\eta}^{sto}_{s6,night} \cdot \eta^{para}} \cdot \frac{t_{s6,night}}{t_{s6,day}}\right) / \left(\bar{\eta}^{r}_{s6,day} \cdot \eta^{c} \cdot DNI_{s6,day}\right) \quad (3\text{-}36)$$

where $\bar{\eta}^{r}_{s,day}, \bar{\eta}^{sto}_{s,m}$, and $\bar{\eta}^{p}_{s,m}$ are upper bounds on receiver, TCES, and turbine efficiency. In the least sunny scenario (s1), the CSP plant is expected to maintain a low output level ($\bar{P}_{s1,day} = 50\ MW$) during the day and no night power output ($Q^{curtail}_{s1,day} = P_{s1,night} = 0$). Thus, $\overline{AREA}$ is calculated as,

$$\overline{AREA} = \left(\frac{\bar{P}_{s1,day}}{\underline{\eta}^{p}_{s1,day} \cdot \underline{\eta}^{sto}_{s1,day} \cdot \eta^{para}} + \frac{P_{s1,night}}{\underline{\eta}^{p}_{s1,night} \cdot \underline{\eta}^{sto}_{s1,night} \cdot \eta^{para}} \cdot \frac{t_{s1,night}}{t_{s1,day}}\right) / \left(\underline{\eta}^{r}_{s1,day} \cdot \eta^{c} \cdot DNI_{s1,day}\right) \quad (3\text{-}37)$$

Given bounds on $AREA$, we calculate bounds on $Q^{in}_{s,day}$ for every scenario and propagate forward from the collector to the turbine to obtain bounds on all energy flows. In the TCES subsystem, bounds on stream flow rates are also calculated by forward propagation moving downstream from R1 to R2b. Other given equipment and unit operation information (e.g., upper temperature limit of the receiver, steam generation requirements, and reaction characteristics) are also utilized. Design (A_i, C^{cc}_i) and operational variables ($Q_{i,s,m}$, $W_{i,s,m}$ and $C^{oc}_{i,s,m}$) are functions of stream conditions so their bounds can be generated accordingly. Finally, the bound on LCOE is derived from bounds on capital cost ($CAPEX$), operational costs ($OPEX_{s,m}$) and net electricity outputs (W^{ele}_{s}).

3.4.4 Results

The optimization model is an MINLP with 1095 variables and 1461 constraints. The nonlinear constraints mainly arise from reaction equilibrium and compression power calculations, as well as equipment sizing. The model is formulated in GAMS (25.0.2) and solved using global optimization solver BARON (17.10.16) [147] on an Intel® i7-4790 CPU (3.6 GHz) with 8 GB RAM.

Due to the complexity of the detailed CSP model, only low time resolution (i.e. 2 modes and ≤ 6 scenarios) leads to computationally tractable problems. Thus, in this case study, we compare the solutions of the proposed stochastic model and the deterministic model, where the design is based on an annual average day ($DNI_{avg,day}$=891 W/m^2, $t_{avg,day}$=8.6 h). The two designs are evaluated through the following process (see **Figure 3-19**). A one-day CSP plant operational model is used, where the first stage design variables are fixed to the ones found by the stochastic/deterministic synthesis approach; and the goal of the operational problem is to achieve maximum daily net electricity output (W_d^{ele}) under the solar condition of a specific day ($DNI_{d,m}, t_{d,m}$). The one-day model is solved separately for each day d of a year ($d = 1,2, \dots 365$), using historic solar irradiance data. The maximum annual power output ($\sum_d W_d^{ele}$) and thus the evaluated LCOE of the given design ($\text{LCOE} = \frac{\text{Annualized cost}}{\sum_d W_d^{ele}}$) is then calculated.

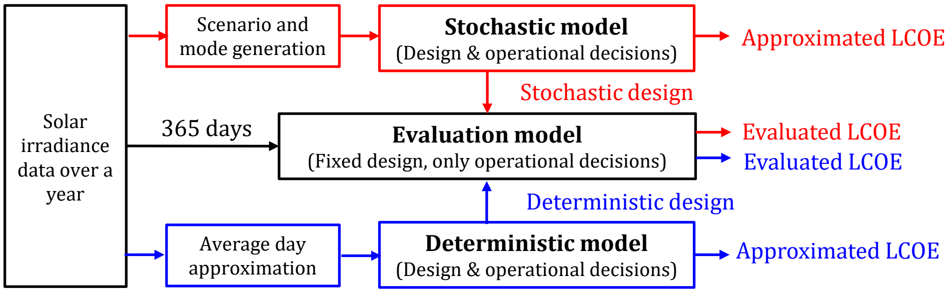

Figure 3-19. Evaluation process for stochastic and deterministic approaches.

The results from the stochastic and deterministic approaches are compared in **Table 3-2**. The stochastic design achieves a 0.3 $₵/kWh$ evaluated LCOE reduction over the deterministic design. While the turbine capacity in both designs are fixed to 100 MW, the deterministic approach leads to a design where the other subsystems are larger (i.e., higher capital cost). This is because the average day assumption overestimates the plant annual power output to a great extent, and thus underestimates the LCOE (see **Table 3-2**). This *larger* deterministic design is better for the average day, but inferior when the seasonal variability is considered. The stochastic approach, utilizing the knowledge of distributions on solar conditions, allows a more accurate estimation of the power output and LCOE.

Table 3-2. Comparison of stochastic and deterministic designs.

Approach	LCOE (₵/kWh)		Annual average power level (MW)		Capital cost (M$)				
	Approximated	Evaluated	Approximated	Evaluated	Total	Collector	Receiver	TCES	Turbine
Stochastic	12.4	13.0	78.6	74.9	789	386	180	43	179
Deterministic	11.1	13.3	97.4	81.4	879	454	194	52	179

Finally, to better understand the second stage operational decisions of the proposed approach, power output and compression demand in different scenarios are shown in **Figure 3-20**. In scenarios s5 and s6, the plant maintains full-load during both day and night. In scenarios with lower solar irradiance, the production during daytime is high but drops notably during the night, because night generation requires compression for gas storage, the amount of which depends on the night production level and duration. Finally, in scenario s1, there is no night production because the total solar input is low.

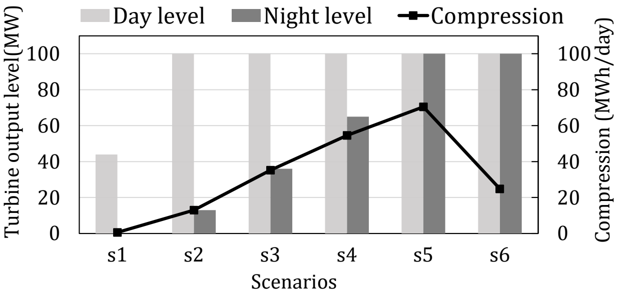

Figure 3-20. Turbine output levels and compression demands for storage in all scenarios.

3.5 Remarks

In this section, we study the accuracy of the proposed multimode stochastic programming approach through an illustrative example, in which a simplified CSP plant (as shown in **Figure 3-21**) is designed. The simplified process considers the plant at the subsystem level, instead of the detailed unit level, as is done in the previous case study. The price (λ) and efficiency (η) of each subsystem are given as parameters. This simplified process preserves the main characteristics of CSP plants and leads to a tractable optimization problem, allowing us to compare designs obtained from various approaches with different time resolution.

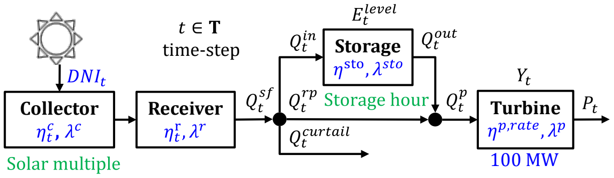

Figure 3-21. The simplified CSP process with main optimization variables (design: green, operation: black) and parameters (blue).

The 1-year hourly DNI data of southern California (described in the previous case study section) is used in this example. To deal with the seasonal and daily variability in DNI, three approaches are explored. The first approach is deterministic, where the design is based on an annual average day divided into 24 1-hour periods or 2 modes. The second one is the conventional stochastic programming, where the seasonal variability is represented by a small number of typical days (i.e., scenarios) and each day is divided into 24 1-hour periods with the associated hourly DNI data. The third approach is the proposed multimode stochastic programming, which further approximates the hourly daily profile of each scenario through modes. For the last two approaches, different number of scenarios (365, 12 and 6) are used. Scenarios are further considered to be temporally independent, and energy can only be stored and used within each day. Given that energy storage across days may occur in real CSP operation, we also use a full fidelity model ($\mathcal{M}$), which utilizes the original 1-year hourly DNI data and allows stored energy to pass on to any consecutive time-steps. By solving $\mathcal{M}$, we obtain a benchmark design ($\boldsymbol{x}^*$) which is considered as the optimal design in real plant operation.

For each approach, an optimization model is developed for the optimal design (i.e., collector and storage size) and operational decisions (i.e., energy flows between subsystems at each time-step) using annual profit maximization as objective function. The parameters, variables, and equations of model $\mathcal{M}$, which is the most complex and detailed model, are given in the **Appendix A2.2** information. The design obtained from each approach is then evaluated, post optimization, using hourly DNI data over 365 days. The evaluation is performed using model $\mathcal{M}^{OPER}$ which is, essentially, model $\mathcal{M}$ with fixed design decisions. In other words, a design obtained from a given approach is evaluated assuming that operations can be optimized on a daily basis using a detailed operational model.

All models are solved using CPLEX (12.8.0) via GAMS (25.0.2) and on an Intel® i7-4790 CPU (3.6 GHz) with 8 GB RAM. Default options with resource limit of 3 hours are used. The computational statistics of the three approaches and $\mathcal{M}$ are shown in **Table 3-3**. The computational results show that, not surprisingly, $\mathcal{M}$ is the most computationally demanding model. The conventional stochastic programming approach leads to significantly smaller solution times as the number of scenarios decreases, and the proposed multimode SP approach further reduces the problem size and solution times. Notably, the multimode SP model appears to be 2-3 orders of magnitude faster than the standard SP model when the same number of scenarios are used, and all three instances based on the multimode SP approach are solved to optimality in 2s.

Table 3-3. Comparison of computational statistics of different approaches.

Approach	Scenarios	Periods	Constraints	Variables	CPU (s)	Gap
Deterministic	1	2	45	40	0.1	-
	1	24	336	310	0.1	-
Stochastic	6	24	1,896	1,750	0.2	-
	12	24	3,768	3,478	101	-
	365	24	114,269	105,142	10,800	4%
Stochastic Multimode	6	2	150	130	0.1	-
	12	2	276	238	0.1	-
	365	2	7,689	6,592	2	-
$\mathcal{M}$	365	24	113,904	105,142	10,800	10%

The eight designs obtained from three approaches, as well as their evaluated profits, are compared with the benchmark design $\boldsymbol{x}^*$ in **Table 3-4** and **Figure 3-22**, where the X and Y axes correspond to the two design variables, solar multiple and storage hour, respectively. The former yields the size of the collector and the latter the size of the storage subsystem, both normalized with respect to the fixed turbine size (100 MW). **Figure 3-22** shows that plant designs based on an annual average day (shown as purple dots) deviate significantly from $\boldsymbol{x}^*$ (red diamond), while better designs are obtained when stochastic approaches is adopted. Note that the multimode SP approach leads to superior designs (green dots) than the ones based on conventional SP (blue dots). This is because the two-mode approximation, which centralizing the DNI profile (see **Figure 3-5**B), overestimates the storage size requirement. This overestimation offsets the underestimation caused by assuming temporally independent scenarios.

Our proposed approach with 12 scenarios and 2 modes leads to a significantly smaller optimization problem compared to $\mathcal{M}$, but yields a design that is very similar to the optimal design $\boldsymbol{x}^*$, and leads to an evaluated profit that is only 0.3% lower than the evaluated profit of the optimal design (3.30 M\$/y compared to 3.31 M\$/y).

Table 3-4. Comparison of results of different approaches.

Approach	Scenarios	Periods	Solar multiple	Storage hour	Profit (M$/y)	
					Approximated	Evaluated
Deterministic	1	2	3.30	14.3	23.46	2.02
	1	24	3.16	10.7	28.53	-2.80
Stochastic	6	24	2.69	10.9	11.48	0.66
	12	24	2.72	10.5	10.77	-0.43
	365	24	2.96	12.1	4.50	2.19
Stochastic Multimode	6	2	2.81	14.2	5.85	3.20
	12	2	2.87	13.8	5.06	3.30
	365	2	2.89	14.0	3.78	3.30
$\mathcal{M}$	365	24	2.87	14.0	3.31	3.31

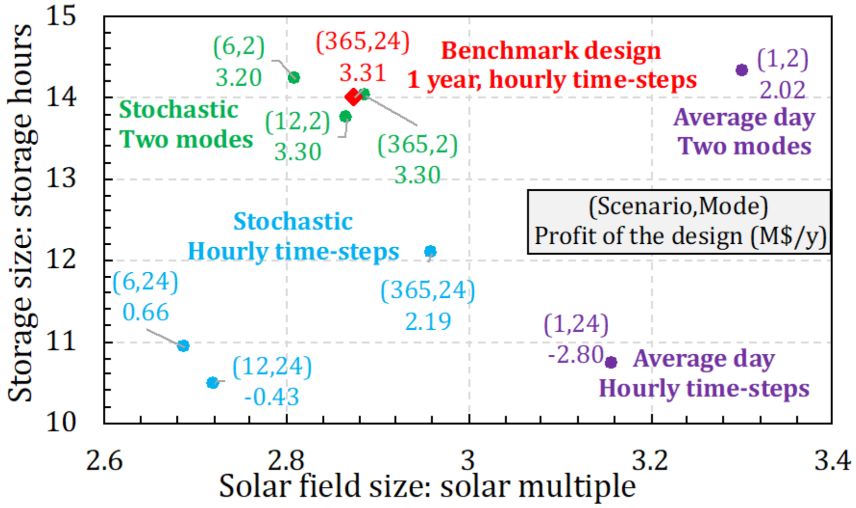

Figure 3-22. Comparison of design decisions based on different approaches and their corresponding evaluated profits.

3.6 Conclusions

In this work, we developed an optimization-based framework for process synthesis under resource, broadly defined, variability in two frequencies. We first introduced scenarios and modes to represent low and high frequency variability, respectively. We then proposed a multimode superstructure to consider different process alternatives for each mode, and formulated the synthesis problem as a multimode two-stage stochastic programming model. Compared to deterministic approaches, the proposed approach yields significantly better solutions. Compared to conventional stochastic programming approaches, it leads to computationally more efficient models which, in addition, yield designs that are very close to the designs that would be obtained if the exact problem could be solved to optimality, which rarely can be. The proposed approach is well suited to address, specifically, the synthesis of renewable energy systems where the energy resource (e.g., solar, wind) often exhibits variability in two scales.

Chapter 4

Design of Fixed-bed Reactors for Solid-gas TCES[4]

4.1 Introduction

Different solar reactors have also been developed for solid-gas reactions. Among all 68 reported solid-gas solar reactors, fixed bed is the most frequently adopted reactor type (50%), followed by fluidized bed (21%) and rotary kiln (15%) [88]. In fixed-bed reactors, solid reactants are packed inside the reactor with heat transfer fluid (HTF) or working fluid (WF) flowing through the stationary bed. Fixed beds are easy to design, construct and operate. They have been experimentally tested for carbonate [31], hydroxide [48,49,87,174,175], and redox TCES systems [70–72]. In parallel, numerical models with different levels of complexity have been developed [23,176,177], for system diagnosis, experimental results evaluation, and reactor design improvements. Slow heat transfer due to low thermal conductivity of porous bed has been identified as the major limitation for fixed-bed reactor in TCES [51,87].

---

[4] The contents of this chapter appear in Peng, Yao, Root and Maravelias, *Appl Energy*. **submitted**

While most research on TCES focuses on reaction and reactor studies, a few system-level studies are available for CSP with solid-gas TCES systems (hereinafter referred to as "CSP-TCES" systems), including energy/exergy analyses, process design, and techno-economic analysis (TEA). Albrecht et al. [76] and Lei et al. [178] evaluated the thermodynamic performance of redox TCES. Pelay et al [57]. performed exergy analyses on several integration concepts of TCES in Rankine-cycle driven CSP. Conceptual process design has been conducted for CSP employing carbonate [27,179,180], hydroxide [59,60] and redox TCES [69,78]. Bayon et al. [42] assessed the techno-economic performance for 17 solid-gas TCES systems. Salas et al. [61,181] optimized the design of CSP-$\mathrm{Ca(OH)_2}$ TCES together with its power production strategy in spot electricity markets.

Nevertheless, previous reactor and system-level TCES studies have some limitations. The detailed reactor studies investigate the TCES reactor in isolation, neglecting its interactions with other plant components (e.g., receiver and turbine). The reactors are typically studied under one specified condition where hot and cold fluids flow through the reactor at a constant flowrate and inlet temperature. However, in real plant operation, the HTF flowrate varies under different solar conditions during reactor charging and the WF outlet temperature decreases during reactor discharging. Designing the reactor in isolation and based on one specific operating condition does not necessarily result in high integrated plant performance. On the other hand, the system-level studies evaluate the integrated plant performance, but are typically based on ideal reactors which do not take into account the rate of reaction and heat transfer. Neglecting the kinetics and heat transfer limitations, especially in fixed-bed reactors, may lead to unrealistic reactor designs and underestimated reactor costs. Moreover, although CSP plants are subject to variability in solar irradiance, the majority of system-level studies evaluate the plants based on an annual average solar condition, which may result in inaccurate estimation of plant performance.

Accordingly, the goal of this work is to provide a system-level analysis for CSP-TCES using an optimization-based process model. The proposed model: (1) considers the interactions between plant components; (2) accurately predicts the reactor performance over a wide operating space; and (3) evaluates the overall plant performance under seasonal solar variability. Special emphasis is placed on the modeling of fixed-bed reactors that operate in a cyclic batch mode, which are modeled using partial differential equations (PDEs) in time and space.

The outline of this chapter is shown in **Figure 4-1**. We first specify the TCES integration strategy and fixed-bed reactor configuration given its unique heat-transfer considerations; then carry out expensive reactor simulations offline at various operating conditions; generate reactor surrogate models via dimensional analysis and data fitting; and, finally, integrate the surrogate models into the CSP-TCES process synthesis optimization model to obtain the optimal design and plant performance. In the last section, we discuss the impacts of key process and reaction parameters on CSP-TCES performance.

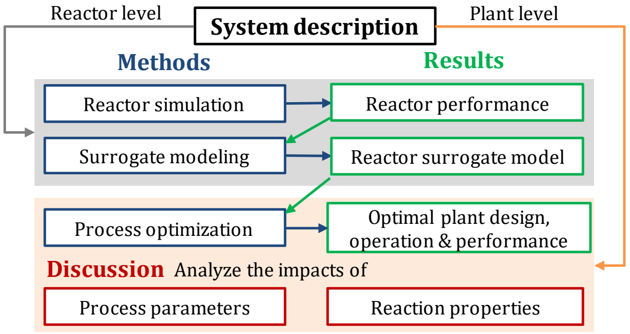

Figure 4-1. Outline of the proposed system-level analysis.

4.2 System description

4.2.1 CSP-TCES process

This study considers a central receiver CSP plant (illustrated in **Figure 4-2**), which comprises four components: the solar field (i.e., collector), receiver, TCES system and power block. The TCES is based on a solid-gas reversible reaction ($\mathrm{A\ (s) \leftrightarrow B\ (s) + C\ (g)}$), which is carried out in a fixed-bed reactor.

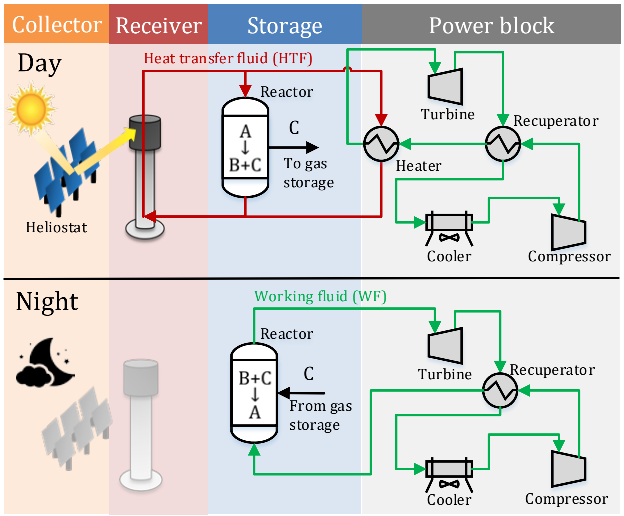

Figure 4-2. Schematic diagram of a power tower CSP plant with solid-gas TCES employing a fixed-bed reactor.

During the day, the solar field concentrates sunlight onto a receiver, where sunlight is converted to heat and absorbed by a heat transfer fluid (HTF). The hot HTF splits into a portion flowing through the power block heater for power generation and the remainder through a fixed-bed reactor for heat storage. The fixed-bed reactor operates in a cyclic batch mode. During daytime operation, heat is transferred from the HTF to the fixed bed and drives an endothermic reaction ($\mathrm{A \rightarrow B + C}$). During nighttime operation, the power block working fluid (WF) enters the fixed-bed reactor and extracts the heat released by the reverse (exothermic) reaction ($\mathrm{B + C \rightarrow A}$).

Solid reactants A, B are packed inside the reactor and converted, back and forth, in a cyclic operation. Gas reactant C leaves/enters the reactor during storage charging/discharging. In this work, we study three solid-gas reactions, summarized in **Table 4-1**, to represent carbonate, hydroxide and redox types respectively. Based on the properties of C (i.e., percentage in air, boiling point), the three reactions are applied with different gas storage options (see **Figure 4-3**). An open-loop configuration is used for the redox reaction, where O_2 generated during charging is directly emitted and air is used as the source of oxygen during discharging. A closed-loop configuration is used for the hydroxide and carbonate reactions, where the generated H_2O and CO_2 are stored in water vessels (1 bar, 25°C) and liquid CO_2 vessels (75 bar, 25°C), respectively.

Since reactions occur at high temperature but C is emitted/ stored at low temperature, significant amount of sensible heat is associated with this cooling process (up to 40% of the total heat stored in TCES). Storing this heat and reusing it to preheat the gas entering the reactor during discharging is necessary for high plant efficiency. To achieve this, a sensible heat storage unit is used in this study. For the carbonate reaction, a compressor is used to compress CO_2 into the storage vessels. When CO_2 exits the vessels during discharging, it expands through a turbine for power generation.

Table 4-1. Reaction properties and material prices of selected reactions.

Type	$A(s) \leftrightarrow B(s) + C(g)$	$T^{eq}*$ (K)	ΔH^{rxn} (kJ/kg A)	Cp_A $(kJ/kg \cdot K)$	Price of A ($/ton)
Redox	$6Mn_2O_3 \leftrightarrow 4Mn_3O_4 + O_2$	1094	202	0.83	1000
Hydroxide	$Ca(OH)_2 \leftrightarrow CaO + H_2O$	778	1409	1.53	150
Carbonate	$CaCO_3 \leftrightarrow CaO + CO_2$	1168	1779	1.29	100

$*T^{eq}$ is calculated at gas C partial pressure of 1 bar for hydroxide and carbonate reactions, at 0.21 bar for redox reactions.

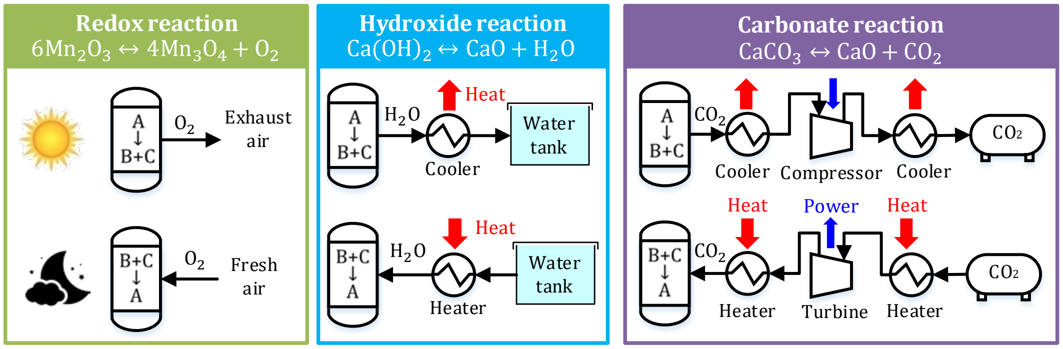

Figure 4-3. Gas storage options for three TCES reactions.

4.2.2 Power block

The commercially developed CSP plants use molten-salt as HTF, with a maximum operating temperature of 565℃. To attain higher temperature and therefore higher turbine efficiency, supercritical CO_2 (s-CO_2) has been identified as a promising candidate both as the HTF and WF. In the meantime, s-CO_2 Brayton cycles attract increasingly attention because they have higher power cycle efficiency, smaller equipment and lower costs than current steam Rankine cycles [182–184]. In this study, we use s-CO_2 as both the HTF and WF and s-CO_2 Brayton cycle for power generation.

The s-CO_2 Brayton cycle adopts a simple recuperative configuration (see **Figure 4-4**A), which consists of one compressor, turbine, recuperator, heater/reactor and cooler. The recuperator transfers heat from the hot turbine exhaust to the cold compressor outlet. The recuperator outlet is then heated to turbine inlet temperature (TIT) in the heater by the HTF (daytime) or in the reactor by the exothermic reaction (nighttime). We build a s-CO_2 power cycle model to evaluate the power cycle performance at different turbine inlet temperatures (TIT) with the following assumptions:

(1) HTF pressure and turbine inlet pressure are 25 MPa; turbine pressure ratio is 3.

(2) Dry cooling is adopted. Assuming a 30 ℃ ambient temperature and a 10 ℃ approach temperature, the compressor inlet temperature is 40℃.

(3) Isentropic efficiencies of the turbine and compressor are 0.9.

(4) The minimum approach temperature of the recuperator is 10℃.

Figure 4-4A illustrates the T-S diagram of the s-CO_2 cycle at TIT of 1000 K. **Figure 4-4**B shows the power cycle efficiency (η^p) and heater/reactor inlet temperature varying as a function of TIT. Both relations are obtained through data fitting (functions shown in **Figure 4-4**B) and used in the reactor and plant models.

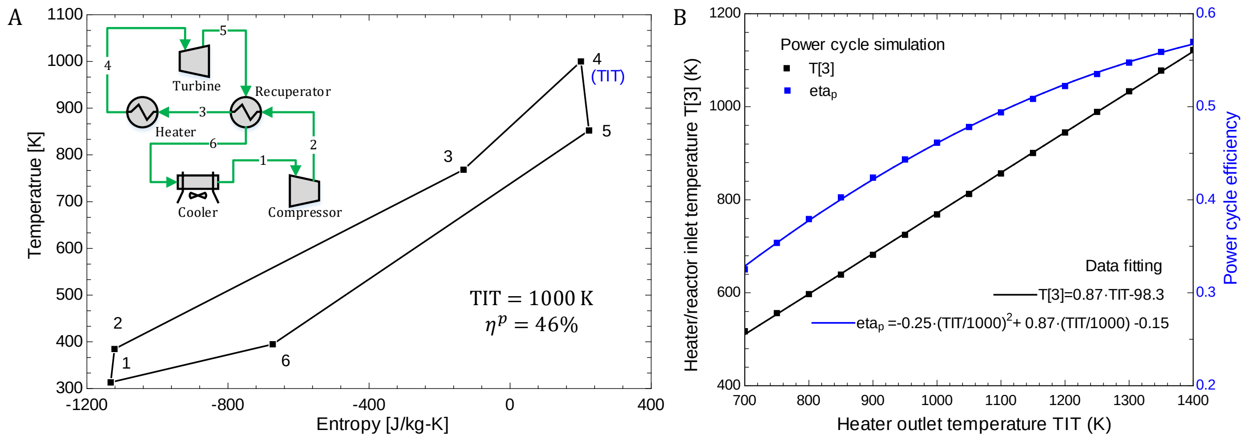

Figure 4-4. (A) T-S diagram of the s-CO_2 cycle at TIT of 1000 K; (B) power cycle efficiency (blue) and heater inlet temperature (black) versus TIT.

4.2.3 Fixed-bed reactor

The fixed-bed reactor adopts a shell-and-tube configuration (see **Figure 4-5**) to enable heat exchange between reactants and HTF/WF. The fixed bed (i.e., the shell side) is packed with solid reactants and HTF/WF flow through a bundle of tubes (distributed evenly inside the bed). The computational domain of our reactor numerical simulation consists of one tube and the bed around it (illustrated as the dashed boxes in **Figure 4-5**). The key reactor parameters are listed in **Table 4-2**.

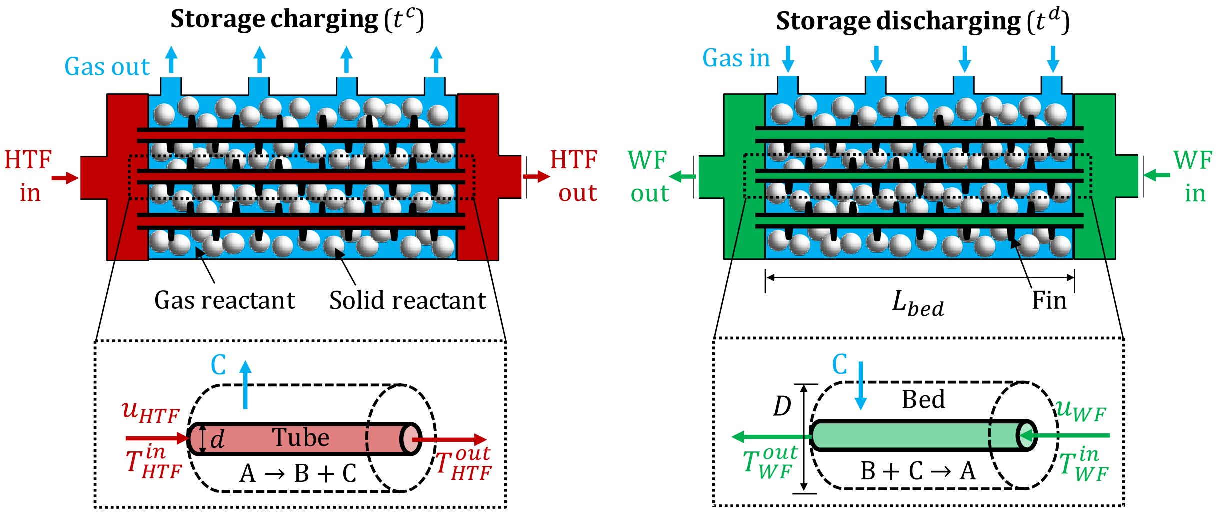

Figure 4-5. Fixed-bed reactor with indirect heat exchange.

A disadvantage of indirect reactors is the slow heat transfer so our goal is to enhance the overall heat transfer coefficient (U) between the fluid and the bed, which can be expressed as

$$1/U = 1/h_f + (D - d)/k_{bed} \tag{4-1}$$

where $1/h_f$ and $(D - d)/k_{bed}$ characterize the heat transfer resistance in the tube and shell side, respectively. On the tube side, h_f is the convective heat transfer coefficient of the fluids (HTF/WF), which can be calculated from Nusselt number (Nu),

$$h_f = Nu \cdot k_f/d \tag{4-2}$$

Due to the high fluid density, a small u_{WF} of 0.1 m/s is adopted to ensure long fluid residence time for a moderate-length reactor. At this velocity, the fluids are in laminar flow region with a constant Nu of 4.4.[185] Therefore, according to eqn (4-2), small *d* is required to achieve high h_f.

On the shell side, k_{bed} is the bed thermal conductivity, which is typically low (~1 W/m-K) due to the porous bed structure. Previous studies show that k_{bed} can be enhanced by adding high conductive fillers/fins[185]. In this study, we assume that the bed porosity is 0.7, comprising reactants A/B in the solid phase and C in the gas phase. We use fins to increase k_{bed} to 5 W/m-K. In addition to high k_{bed}, a small $(D - d)$ is also needed to achieve high U.

To determine the optimal reactor geometry, we run reactor numerical simulations with different tube diameters (see **Appendix A3.3**) and find that $d \leq 2$ mm is required for efficient heat transfer. This finding agrees with previous studies on $Ca(OH)_2$ TCES where a pilot scale fixed-bed reactor with HTF channel width of 1.5 mm was simulated [186] and built [187]. However, the previous $Ca(OH)_2$ reactor adopts a plate heat exchanger configuration which allows maximum HTF pressure of 5 bar. To be compatible with the 75 bar s-CO_2, shell-and-tube heat exchanger is used in this study with tube diameter of 2 mm, wall thickness of 0.5 mm and tube distance of 20 mm. The proposed TCES reactors are similar to microchannel heat exchangers/reactors which have been designed and fabricated economically at an industrial scale [188]. Since heat exchangers with ultra-small tubes are still an emerging technology, we have conservative cost estimations on them. The capital costs of the proposed heat exchangers are 50 times of their construction material costs while 1.5 times are suggested for conventional heat exchangers [189]. Given the uncertainty in this cost estimation, we also provide sensitivity analysis on reactor costs in the Discussion Section.

To determine the optimal HTF/WF inlet temperatures, we also run simulations with different combinations of T_{HTF}^{in}/T_{WF}^{in} for all three reactions. For a reversible reaction in TCES, temperatures should satisfy $T_{WF}^{in} < T^{eq} < T_{HTF}^{in}$. The selected T_{HTF}^{in}/T_{WF}^{in} are shown in **Table 4-2** and the detailed comparisons among different inlet temperatures can be found in **Appendix A3.2**.

Table 4-2. Key reactor parameters for numerical simulations.

Fixed-bed reactor geometry				
Tube diameter	d	0.002 m		
Distance between tubes	D	0.02 m		
Heat transfer coefficient	U	127 W/m^2-K		
Bed porosity	ε_{bed}	0.7		
HTF & WF: s-CO_2 at 250 bar				
HTF inlet velocity [a]	u_{HTF}	0.05 – 0.2 m/s		
WF inlet velocity	u_{WF}	m/s		
		$\mathrm{Mn_2O_3}$	$\mathrm{Ca(OH)_2}$	$\mathrm{CaCO_3}$
HTF inlet temperature	T_{HTF}^{in}	1273 K	923 K	1373 K
WF inlet temperature [b]	T_{WF}^{in}	1009 K	704 K	1095 K

$a.\ u_{HTF} = u_{WF} \cdot t^d / t^c$; $b.\ T_{WF}^{in}$ will decrease during discharging

4.3 Methods

4.3.1 Reactor numerical simulations

The major assumptions of the reactor numerical model used are summarized as follows:

(1) The model is based on a one-dimensional (1D) representation of the fixed-bed reactor along the axial (z) direction. The reactor has indirect heat exchange between the two domains: the porous bed and the fluids. This assumption is valid since the temperature gradient in the radial direction is negligible based on the reactor parameters shown in **Table 4-2**.

(2) The HTF/WF in the tube and the gas in the bed are at constant pressure, 250 bar and 1bar, respectively. It is assumed that gas C produced (consumed) can be removed from (added to) the bed instantaneously at the bed temperature.

(3) T_{WF}^{in} and T_{WF}^{out} follow the relationship obtained from the power cycle model (see **Figure 4-4**B).

(4) The porous bed is treated as continuum. The resistances of heat and mass transfer between the solid and gas in bed are neglected.

(5) The heat loss to the ambient is neglected.

According to the above assumptions, a numerical model describing the heat transfer, energy balance and reaction in the fixed-bed reactor is developed. For brevity, we only present the major governing equations. The details of the numerical model, including initial and boundary conditions, and kinetic models are provided in **Appendix A3.1**.

The energy balance for the fluids (HTF/WF) is

$$A_{tube}\rho_f {C_p}_f \frac{\partial T_f}{\partial t} + A_{tube}\rho_f {C_p}_f u_f \frac{\partial T_f}{\partial z} - A_{tube}k_f \frac{\partial^2 T_f}{\partial z^2} = P_{tube}U(T_{bed} - T_f) \qquad (4\text{-}3)$$

where T_f and T_{bed} denote the temperature of the fluids and the bed, respectively; A_{tube} is the cross-sectional area of the tube; and P_{tube} is the cross-sectional perimeter.

The energy balance for the bed is

$$A_{bed}\left(\rho C_p\right)_{bed} \frac{\partial T_{bed}}{\partial t} - A_{bed}k_{bed} \frac{\partial^2 T_{bed}}{\partial z^2} = A_{bed}Q^{rxn} + P_{tube}U(T_f - T_{bed}) \qquad (4\text{-}4)$$

where A_{bed} is the cross-sectional area of the surrounding bed; $\left(\rho C_p\right)_{bed}$ is the effective volumetric heat capacity of the porous bed, comprising the gas and solid phase,

$$\left(\rho C_p\right)_{bed} = \varepsilon_{bed} \cdot \left(\rho_g {C_p}_g\right) + (1 - \varepsilon_{bed}) \cdot (\rho_s {C_p}_s) \qquad (4\text{-}5)$$

The rate of heat generation/depletion due to the reaction, is given by

$$Q^{rxn} = (1 - \varepsilon_{bed})\rho_s \Delta H^{rxn} \frac{dX_{bed}}{dt} \qquad (4\text{-}6)$$

where ΔH^{rxn} is the reaction enthalpy, and X_{bed} is the conversion of solid reactant A in the bed (0: pure A; 1: pure B). The rate of conversion is calculated using the empirical kinetics models presented in previous studies[177,190–192],

$$\frac{dX_{bed}}{dt} = k_0 \exp\left(-\frac{E_a}{R_{const}T_{bed}}\right) {X_{bed}}^a (1 - X_{bed})^b \left|1 - \frac{p_C}{p_C^{eq}}\right|^s \qquad (4\text{-}7)$$

where p_C is the partial pressure of gas C and p_C^{eq} is the equilibrium pressure of gas C at the bed temperature. The values of k_0, E_a, a, b, and s for the three reactions can be found in **Appendix A3.1**.

The reactor model is implemented in the commercial software, COMSOL Multiphysics® and solved by the finite element method. The geometry and time are discretized by customized non-uniform grids (0.0005-0.005 m) and time steps (0.000001-5 s), respectively. To simulate the periodic operation of TCES reactor, the boundary conditions are specified alternately in accordance with either the charging or the discharging half-cycle. The final state of the previous half-cycle is the initial state for the subsequent one. The simulations are repeated for multiple cycles until the reactor reaches quasi-steady state (i.e., discrepancy of local bed temperatures at the final state between two consecutive cycles is less than 0.1 K)

4.3.2 Surrogate modeling

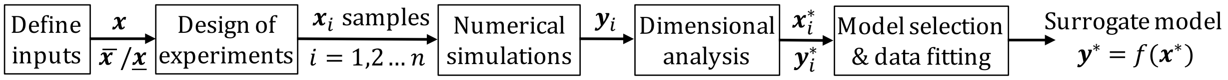

Figure 4-6. Procedure of surrogate model generation.

The procedure to replace the reactor numerical model in the previous section with a surrogate model is shown in **Figure 4-6**. The first step is to identify the input variables $\boldsymbol{x}$ and define their lower and upper bounds ($\overline{\boldsymbol{x}}\,/\underline{\boldsymbol{x}}$). **Table 4-3** shows the three input variables and their ranges in this study. The fixed-bed reactor length (L_{bed}) is the design variable. Simulations with various L_{bed} can help us understand how the plant performance improves with increasing storage capacity. A reactor can operate differently under various solar conditions over a year. To simulate these different conditions, we have reactor charging and discharging time (t^c and t^d) as two operational input variables.

The next step is to generate sampling points ($\boldsymbol{x}_i$) in the design space using design of experiments. Based on the variable ranges defined in **Table 4-3**, a total of 72 sampling points are generated via Latin hypercube sampling. A simulation is carried out for each sample in COMSOL Multiphysics® using the reactor numerical model. Bed temperature and conversion profiles, as well as HTF/WF outlet temperatures are obtained as outputs ($\boldsymbol{y}_i$) for each simulation.

Compared to conventional surrogate modeling, we add a dimensional analysis step before data fitting. The surrogate models are then constructed based on dimensionless variables ($\boldsymbol{x}_i^*$, $\boldsymbol{y}_i^*$) instead of ($\boldsymbol{x}_i$, $\boldsymbol{y}_i$). **Table 4-3** shows the dimensionless input and output variables ($\boldsymbol{x}^*, \boldsymbol{y}^*$) in this study. The detailed definitions of theses variables will be given in the Results Section. The benefit of dimensional analysis, illustrated by Sanchez et al [193] in the thermal modeling of different multiphysics systems, is that it leads to surrogate models that have more compact forms and better predictive accuracy over a wide range of design variables. Another benefit is potential dimensionality reductions by identifying the correlations between the original input variables. This will be illustrated in **Figure 4-10** where the output variables χ and φ are only functions of one dimensionless variable θ instead of three original input variables (L_{bed}, t^c, t^d). Finally, based on the sampling data, we select the surrogate model structure and fit the data through regression.

Table 4-3. Surrogate model input and output variables.

Original input variables $\boldsymbol{x}$		
Bed length	L_{bed}	0.8-3.2 m
Charging time	t^c	3-12 h
Discharging time	t^d	3-12 h
Dimensionless input variables $\boldsymbol{x}^*$		
Normalized bed storage capacity	θ	0.5-5
Heat transfer effectiveness during charging/discharging	κ^c/κ^d	7-103
Original output variables $\boldsymbol{y}$		
Bed temperature	$T_{bed}(z,t)$	255-1373 K
Bed conversion	$X_{bed}(z,t)$	0-1
HTF/WF outlet temperature	$T_{HTF/WF}^{out}$	333-1373 K
Dimensionless output variables $\boldsymbol{y}^*$		
Bed storage capacity utilization	φ	0.2-2
Overall bed conversion	χ	0-1
Power generation effectiveness	γ	0-1

4.3.3 Process optimization

We select Daggett in southern California (34.87°N,116.78°W) as the plant site and obtain its weather data from the National Solar Radiation Data Base [194]. To consider the seasonal variability in solar irradiance, we generate six representative scenarios (i.e., days) from the annual data using centroid clustering algorithm. The sun hours, solar irradiance and occurrence frequency of each scenario is provided in shown in **Table 3-1**.

Peng et al. developed a general process model for CSP-fluid-phase TCES systems [195] and an optimization-based framework for process synthesis under seasonal and daily variability [196]. Building upon these two works, we develop a process model for the design of CSP-solid-gas TCES systems. The model objective is to minimize the levelized cost of electricity (LCOE) of the CSP plant. The associated cost assumptions are provided in **Table 5-3**. The optimization problem is formulated as a two-stage stochastic programming model [196]. This allows us to optimize both first-stage design decisions (e.g., solar field area, receiver size and TCES reactor sizes) and scenario specific second-stage operational decisions (e.g., t^c, t^d,stream flowrates) simultaneously. The optimization model is a nonlinear programming (NLP) model, formulated in GAMS (28.1.0), and solved using global optimization solver BARON (19.7.13) [197].

4.4 Results

In this section, we present the results from the application of the methods introduced in the previous section. Specifically, we present reactor temperature and conversion profiles, reactor surrogate models, and a techno-economic analysis of CSP-TCES systems.

4.4.1 Reactor numerical simulations

Temperature and conversion profiles

To study some key simulation outputs (fixed-bed temperature, T_{bed}, and conversion, X_{bed} profiles), we select one out of the 72 simulations and show its T_{bed} and X_{bed} axial profiles during one charging-discharging cycle in **Figure 4-7**. The selected simulation is based on Mn_2O_3 TCES, with inputs $L_{bed} = 1.6$ m, $t^c = t^d = 6$ h. During charging, HTF at 1273 K enters the fixed-bed reactor from the left inlet ($z = 0$) and delivers heat to the bed. The continuous flow of the hot HTF results in bed temperature (**Figure 4-7**A) and reaction fronts (**Figure 4-7**B) moving to the right. Once the local $T_{bed}(z,t)$ increases above T^{eq}(1094 K), the endothermic reduction reaction starts but initially at a slow reaction rate. As the bed is being further heated, reduction rate grows rapidly with the increase of T_{bed} until the reaction heat absorption and HTF heat input balance out. This leads to the stabilization of T_{bed} at $T^{red} \approx 1190\text{ K}$ (blue arrow in **Figure 4-7**A points to the plateau of the temperature front). After Mn_2O_3 is fully reduced (i.e., $X_{bed} = 1$), the bed is heated to T_{HTF}^{in} rapidly.

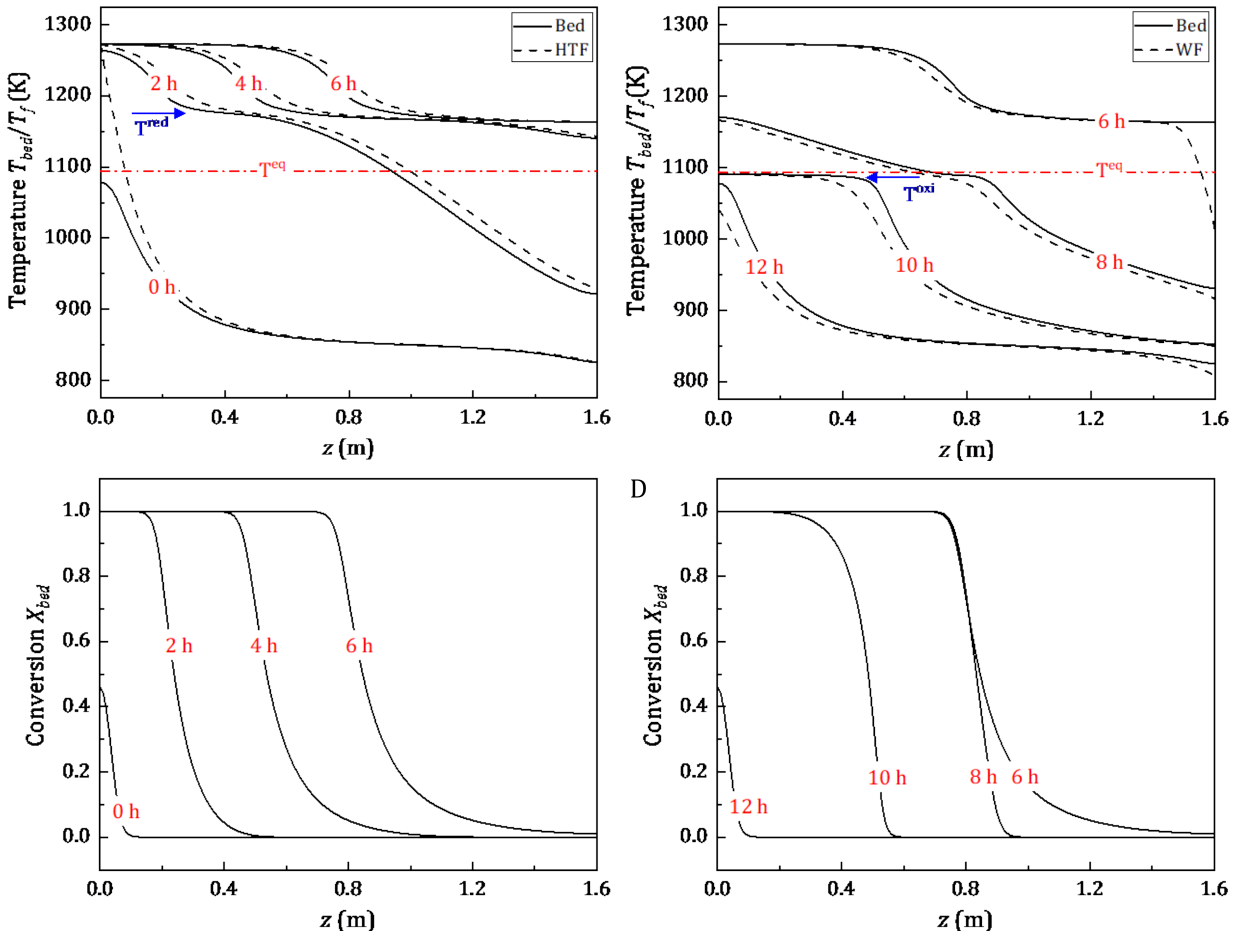

Figure 4-7. Fixed-bed reactor temperature and conversion profiles during charging (A, B) and discharging (C, D). In AC, the solid curves denote the bed temperature and the dashed curves denote the fluid temperature.

During discharging, cooler WF enters the reactor from the right ($z = 1.6$ m) so the temperature (**Figure 4-7**C) and reaction fronts (**Figure 4-7**D) move in a reverse direction. When T_{bed} drops below T_{eq}, the exothermic oxidation reaction starts. A temperature plateau is observed at $T^{oxi} \approx$ 1090 K. The T_{bed} and X_{bed} profiles at the start of charging ($t = 0$) and end of discharging ($t =$ 12 h) are identical, indicating the reactor operates at a quasi-steady state. **Figure 4-7**A/C show that the temperature difference between the bed and the HTF/WF during charging/discharging are small ($\approx$ 20 K), indicating good heat transfer is achieved using this reactor design.

Reactor length

We further study the impact of fixed-bed length on reactor performance. Results of three simulations with Mn_2O_3 TCES, $L_{bed} = 0.8, 1.6, 3.2$ m and $t^c = t^d = 6$ h are compared in **Figure 4-8**. **Figure 4-8**A shows X_{bed} profiles along dimensionless z axis ($z^* = z/L_{bed}$) at the start and end of charging. The overall bed conversion χ can be calculated as the area enclosed by these two X_{bed} profiles, i.e.,

$$\chi = \int_0^1 X_{bed}(z^*, t^c) - X_{bed}(z^*, 0)\, dz^* \tag{4-8}$$

If $L_{bed} = 0.8$ m, then 96% of the bed reacts, while if $L_{bed} = 3.2$ m, then only a small fraction (12%) reacts. The unreacted fraction of the bed only serves as sensible heat storage.

Figure 4-8B shows the HTF/WF inlet ($T_{HTF/WF}^{in}$) and outlet temperatures ($T_{HTF/WF}^{out}$) in one charging-discharging cycle. During charging (t=0-6 h), T_{HTF}^{in} is constant at 1273 K while T_{HTF}^{out} increases with time as the bed is heated up (see **Figure 4-8**A). T_{HTF}^{out} stays close to T^{red} until the bed at the HTF outlet (z^*=1) is fully reduced. During discharging (t=6-12 h), T_{WF}^{out} decreases with time as the bed is cooled down. Based on the power cycle model (**Figure 4-4**), T_{WF}^{in} depends on T_{WF}^{out} and decreases as T_{WF}^{out} decreases. T_{WF}^{out} stays close to T^{oxi} until the bed at the WF outlet (z^*=0) is fully oxidized. After that, T_{WF}^{in} and T_{WF}^{out} drop rapidly (see blue line in **Figure 4-8**B) which leads to lower power cycle efficiency (η^p). To quantify the decrease in η^p, we define a dimensionless output variable γ to measure the power generation effectiveness,

$$\gamma = \frac{W^{night}}{W^{night,max}} = \frac{\int_{t^c}^{t^c+t^d} \left(T_{WF}^{out}(t) - T_{WF}^{in}(t)\right) \cdot \eta^p(t)\, dt}{\left(T_{WF}^{out}(t=t^c) - T_{WF}^{in}(t=t^c)\right) \cdot \eta^p(t^c) \cdot t^d} \tag{4-9}$$

where W^{night} is the actual power generated during discharging and $W^{night,max}$ is the maximum power generated during discharging if there is no decrease in T_{WF}^{in}, T_{WF}^{out} and η^p. The γ values of the three reactors with different L_{bed} are shown in **Figure 4-8**B. In reactors with larger L_{bed} (i.e., storage capacity), the stored energy is not fully depleted so T_{WF}^{out} stays relatively high, leading to higher power generation efficiency (i.e., γ).

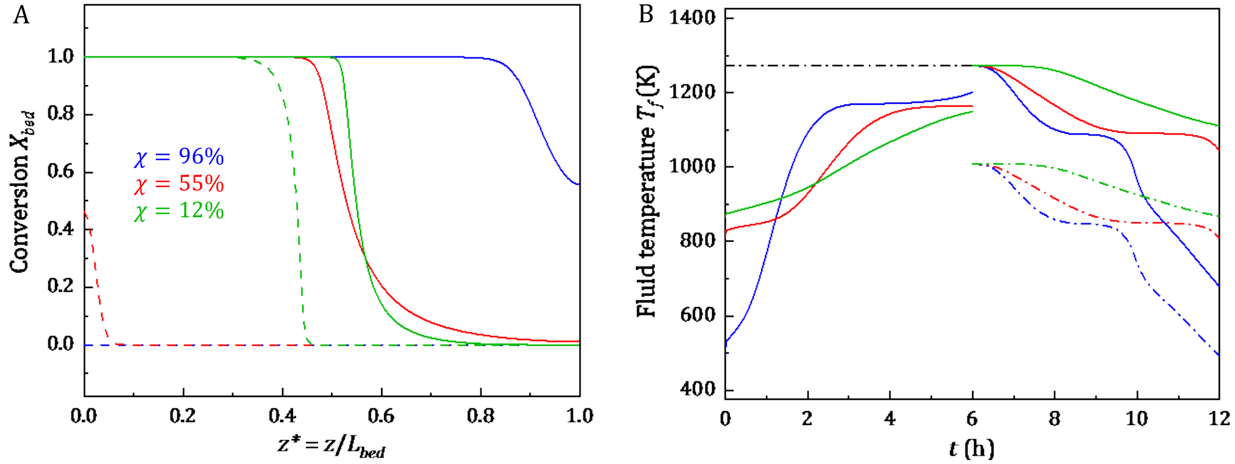

Figure 4-8. (A) Bed conversion and (B) fluid temperature of fixed-bed reactors with different bed length (blue: 0.8 m, red: 1.6 m, green: 3.2 m). In A, conversions at the start of charging (t=0) are shown as dashed lines and at the end of charging (t=6 h) as solid lines. In B, fluid temperatures at the inlet are shown as dash-dotted lines and at the outlet as solid lines. Note that the black dash-dotted line in B denotes an overlap of lines in blue, red, and green.

TCES reactions

Finally, we compare the performance of rectors employing different reactions. For a fair comparison, we consider reactors with the same normalized storage capacity (θ), which is the bed storage capacity normalized by the WF heat requirement (dimensionless),

$$\theta = \frac{Q_{bed}}{Q_{WF}^{max}} = \frac{A_{bed}L_{bed}((\rho Cp)_{bed}\Delta T_{WF}^{max}+(1-\varepsilon_{bed})\rho_s\Delta H^{rxn})}{A_{tube}u_{WF}\rho_{WF}Cp_{WF}\Delta T_{WF}^{max}t^d} \tag{4-10}$$

The numerator, Q_{bed}, is the "nominal design" bed storage capacity, based on both sensible and chemical energy storage. At the nominal design, we assume (1) the average bed temperature increase during charging is equal to ΔT_{WF}^{max} and (2) full bed conversion (i.e., $\chi = 1$). ΔT_{WF}^{max} is the temperature difference between T_{WF}^{in} and T_{WF}^{out} at the beginning of discharging. The denominator,

Q_{WF}^{max}, is the maximum heat required by WF during discharging if there is no decrease in T_{WF}^{in} and T_{WF}^{out}.

We compare the simulation results, with $\theta = 1$, for Mn_2O_3, $Ca(OH)_2$, and $CaCO_3$ TCES reactors with L_{bed} of 1.6, 0.9 and 0.5 m, respectively. $Ca(OH)_2$ and $CaCO_3$ reactors are shorter than the Mn_2O_3 reactor because the former two reactions have much higher ΔH^{rxn} (see **Table 4-1**). **Figure 4-9**A shows X_{bed} profiles and overall conversion χ of the three reactors. With θ identical for each reactor, the differences between X_{bed} are attributed to the different reaction kinetics. $CaCO_3$ reaction has the fastest reaction rate, which leads to the sharpest X_{bed} profile and largest χ (76%).

Figure 4-9B shows the profiles of HTF/WF inlet and outlet temperatures. Different T_{HTF}^{in} and T_{WF}^{in} are selected for the three reactions based on their T^{eq}. For the slow Mn_2O_3 reaction, T_{HTF}^{out} increases gradually while for the other two faster reactions, T_{HTF}^{out} rapidly reaches the endothermic reaction temperature. Since the HTF energy input is proportional to $(T_{HTF}^{in} - T_{HTF}^{out})$, more energy is stored in the Mn_2O_3 reactor during charging. Therefore, Mn_2O_3 reactor supplies more energy to WF during discharging and has the highest γ.

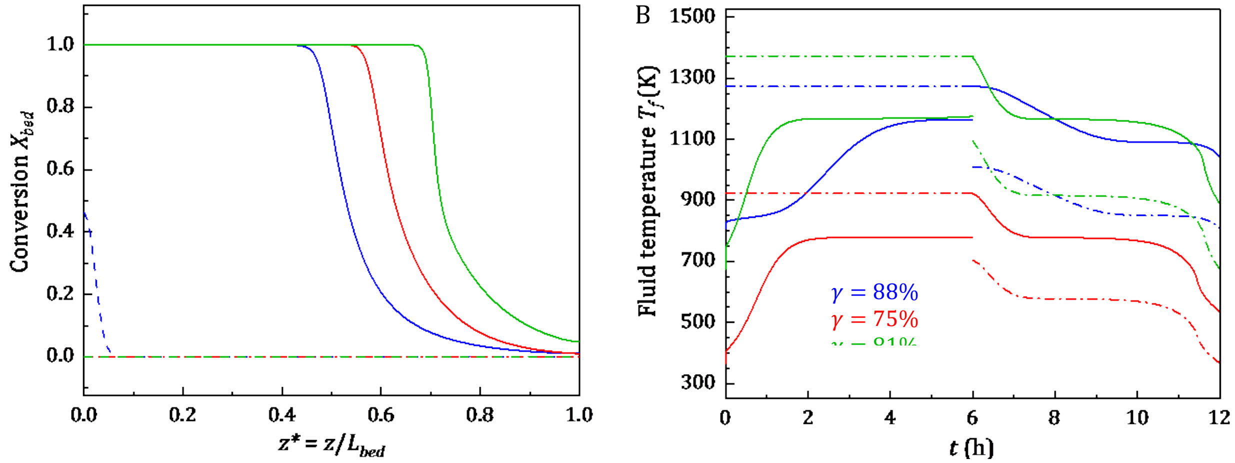

Figure 4-9. (A) Bed conversion and (B) fluid temperature of fixed-bed reactors with different TCES reactions (blue: Mn_2O_3, red: $Ca(OH)_2$, green: $CaCO_3$) at $\theta = 1$. In A, conversions at the start of charging

(*t*=0) are shown as dashed lines and at the end of charging (*t*=6 h) as solid lines. In B, fluid temperatures at the inlet are shown as dash-dotted lines and at the outlet as solid lines.

4.4.2 Surrogate modeling

The surrogate model has two (dimensionless) input variables and three (dimensionless) output variables (see **Table 4-3**). The first input variable θ, which has been defined in the previous section, denotes the bed storage capacity, while the actual heat stored in the bed may be limited by slow heat transfer. Hence, to measure the heat transfer effectiveness, we define another input variable κ, which is obtained from nondimensionalizing the governing equations of the reactor numerical model (see details in **Appendix A3.1**):

$$\kappa = \frac{\text{Heat transfer rate across tube wall}}{\text{Heat advection rate along the tube}} = \frac{4U/d}{u_f \rho_f Cp_f / L_{bed}} \tag{4-11}$$

Note that the heat transfer effectiveness may be different during charging (κ^c) and discharging (κ^d) due to different fluid velocities (u_f). A larger κ is preferred, which leads to a smaller temperature difference between fluid and bed and thus higher exergy efficiency.

The three output variables are (1) overall bed conversion χ, (2) power generation effectiveness γ, and (3) bed storage capacity utilization φ. Since χ and γ have been introduced in the previous section, we hereby only define φ, which is the total stored energy (Q^{sto}) normalized by the bed storage capacity (Q_{bed}),

$$\varphi = \frac{Q^{sto}}{Q_{bed}} = \frac{A_{bed} L_{bed}\left((\rho Cp)_{bed} \Delta T_{bed}^{avg} + \chi(1-\varepsilon_{bed})\rho_s \Delta H^{rxn}\right)}{A_{bed} L_{bed}\left((\rho Cp)_{bed} \Delta T_{WF}^{max} + (1-\varepsilon_{bed})\rho_s \Delta H^{rxn}\right)} \tag{4-12}$$

where ΔT_{bed}^{avg} is the average temperature increase of the bed during charging, which can be calculated from T_{bed} profiles at $t = 0$ and t^c,

$$\Delta T_{bed}^{avg} = \int_0^1 T_{bed}(z^*, t^c) - T_{bed}(z^*, 0)\, dz^* \tag{4-13}$$

Note that $\Delta T_{bed}^{avg}/\Delta T_{WF}^{max}$ represents the utilization percentage of sensible heat storage and χ represents the utilization of chemical energy storage. **Figure 4-10**B and C show that χ, $\Delta T_{bed}^{avg}/\Delta T_{WF}^{max}$ and φ all decrease with the increase of θ. Also, $\Delta T_{bed}^{avg}/\Delta T_{WF}^{max}$ and φ can exceed 1 when the reactor is under designed ($\theta < 1$), and T_{WF}^{out} drops significantly during discharging of small reactors, leading to large ΔT_{bed}^{avg} (i.e., high φ) but less efficient power generation (i.e., low γ).

Figure 4-10 shows the simulation results for 26 Mn_2O_3 TCES sampling points. We observe that the impact of θ on the three reactor performance indicators (γ, χ and φ) is significant when θ is small and becomes less prominent as θ increases. Each of the three outputs forms a monotonic smooth function of θ, with a horizontal asymptote line. Therefore, we use (rotated) hyperbola functions (see **Table 4-4**) to fit the data points in terms of θ.

We also observe that κ^c and κ^d have a notable impact on γ but negligible impact on χ and φ (black dots at same θ and different κ^c, κ^d overlap in **Figure 4-10**B and C). Therefore, we only include κ^c and κ^d in the surrogate model of γ. When κ^c and κ^d are small, the heat transfer between the fluid and the bed is ineffective which appreciably limits γ. As κ^c and κ^d increase, γ increases as the transport limitation is alleviated but further increase of κ^c, κ^d becomes less beneficial to γ, which is now limited by θ. To represent this behavior, two penalty terms ($\frac{c_4}{\kappa^c} + \frac{c_5}{\kappa^c}$) are added to the fitting of γ.

We determine the parameters (c_i) in the fitting functions by regression, minimizing the mean squared error (MSE). The surrogate models for Mn_2O_3 TCES are shown as red lines in **Figure 4-10**. The parameters and the surrogate models for all three reactions are given in **Table 4-4**. All nine surrogate models are highly accurate ($R^2 > 0.99$). In the next section, we integrate these reactor surrogate models into the CSP plant model for process optimization. To avoid extrapolation errors, we bound the input variables within the sampling domains.

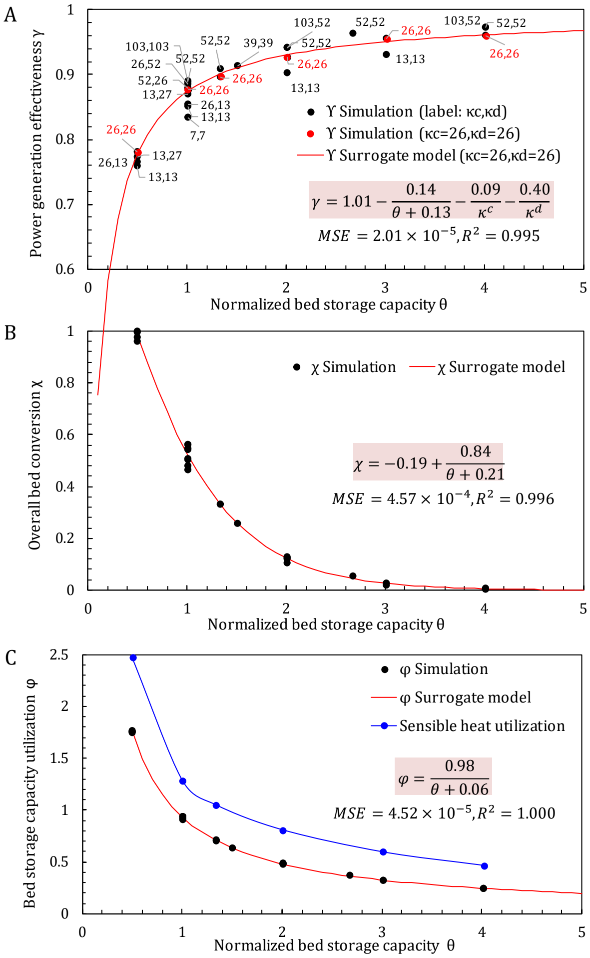

Figure 4-10. Simulation data and fitted surrogate models of Mn_2O_3 TCES.

Table 4-4. Surrogate model fitted from reactor numerical simulations.

TCES reaction	Power generation effectiveness $\gamma = c_1 + \frac{c_2}{\theta - c_3} + \frac{c_4}{\kappa^c} + \frac{c_5}{\kappa^d}$						Overall bed conversion $\chi = c_1 + \frac{c_2}{\theta - c_3}$				Bed capacity utilization $\varphi = c_1 + \frac{c_2}{\theta - c_3}$			
	c_1	c_2	c_3	c_4	c_5	R^2	c_1	c_2	c_3	R^2	c_1	c_2	c_3	R^2
Mn_2O_3	1.01	-0.14	-0.13	-0.09	-0.40	0.995	-0.19	0.84	-0.21	0.996	0	0.98	-0.06	1.000
$Ca(OH)_2$	1.02	-1.06	-3.75	-0.16	-0.37	0.997	-0.12	1.04	-0.30	0.994	-0.01	0.99	-0.09	0.999
$CaCO_3$	1.03	-1.42	-7.18	-0.08	-0.19	0.991	-0.13	1.15	-0.30	0.996	0.01	0.91	-0.02	1.000

4.4.3 Process optimization

The proposed process model is used to optimize the design and operation of CSP plants employing three different TCES systems ($\mathrm{Mn_2O_3}$, $\mathrm{Ca(OH)_2}$, and $\mathrm{CaCO_3}$). We also compare their performance against commercially developed CSP plants which employ two-tank molten salt storage. For each case, we present its optimal LCOE and the corresponding design and energy efficiency.

Economic analysis

The optimal LCOE of the four cases are shown in **Figure 4-11**A. Using $\mathrm{Mn_2O_3}$ and $\mathrm{CaCO_3}$ TCES lead to 0.1 and 0.7 ₵/kWh LCOE reductions, respectively, when compared to CSP plants with two-tank storage. This is mainly because these two TCES lead to higher overall solar-to-electricity efficiency (η^{s-e}) (see **Figure 4-12**) and thus require less input energy (i.e., smaller solar field and receiver) to produce the same amount of electricity. The CSP plant with $Ca(OH)_2$ TCES has the lowest η^{s-e} due to its low reaction temperature and therefore has the highest LCOE among the four cases.

Figure 4-11B shows detailed cost distribution for the storage systems. In two-tank TES, storage material (molten salt) is the main cost driver, while in TCES systems, material costs are significantly lower, especially for $Ca(OH)_2$ and $\mathrm{CaCO_3}$, due to their low material price and high storage density. The $\mathrm{Mn_2O_3}$ TCES system has the highest storage cost due to its expensive fixed-bed reactor (i.e., shell-and-tube heat exchanger), which contributes to 87% of the storage cost. The reactor is highly expensive because in this 100 MW plant, ~15 million small diameter (2 mm) tubes are used to ensure fast heat transfer.

The $Ca(OH)_2$ and $CaCO_3$ TCES systems have smaller reactors (i.e., lower reactor costs) compared to the one employing Mn_2O_3 reaction. This is because ΔH^{rxn} of $Ca(OH)_2$ (1409 kJ/kg) and $CaCO_3$ (1779 kJ/kg) reactions are significantly higher than the Mn_2O_3 reaction (202 kJ/kg). However, gas/liquid storage of reactant C in $Ca(OH)_2$ and $CaCO_3$ TCES are more expensive. **Figure 4-3** shows the unit operations used for storing C in the three TCES systems. In $Ca(OH)_2$ TCES, the sensible heat storage unit and water tank account for 99% and 1% of the gas storage cost, respectively. A large amount of heat needs to be stored during the cooling process of H_2O where phase change occurs. In $CaCO_3$ TCES, the compressor for CO_2 storage and the turbine for electricity generation during CO_2 expansion account for 69% of the gas storage cost because CO_2 is stored at 75 bar.

Interestingly, the two-tank storage system has the lowest storage costs but the second highest LCOE, which indicates that storage systems should not be designed and evaluated in isolation. Their interactions with other components and their impact on the overall plant performance should also be considered.

Energetic analysis

The designs that yield the minimum LCOE and the corresponding energy flows and energy efficiencies are shown in **Figure 4-12**. CSP plants with Mn_2O_3 or $CaCO_3$ TCES have higher overall solar-to-electricity efficiency (η^{s-e}) than that with two-tank storage. Note that η^{s-e} is proportional to the product of receiver efficiency (η^{r}) and turbine efficiency (η^{p}); η^{r} decreases with the increase of T_{HTF}^{in}, whose values are $CaCO_3$: 1373 K $>$ Mn_2O_3: 1273 K $>$ $Ca(OH)_2$: 923 K $>$two-tank: 838 K. With respect to η^{p}, high T_{HTF}^{in} leads to high working fluid temperature (T_{WF}^{out}) and thus high η^{p}. While T_{WF}^{out} remains the same as T_{HTF}^{in} in two-tank sensible storage, T_{WF}^{out} drops during the storage discharging in fixed-bed TCES. This is why $Ca(OH)_2$ has higher T_{HTF}^{in} but lower η^p than two-tank storage.

In the TCES reactors, energy is stored in the form of both sensible heat and chemical energy, with the percentages shown in **Figure 4-12**. Reactions with high ΔH^{rxn} and fast reaction rates (e.g., $CaCO_3$ reaction) have higher fraction of chemical energy storage. This leads to higher bed storage density (i.e., smaller reactor) at a penalty of higher cooling duty and compression power for gas storage since more C is generated.

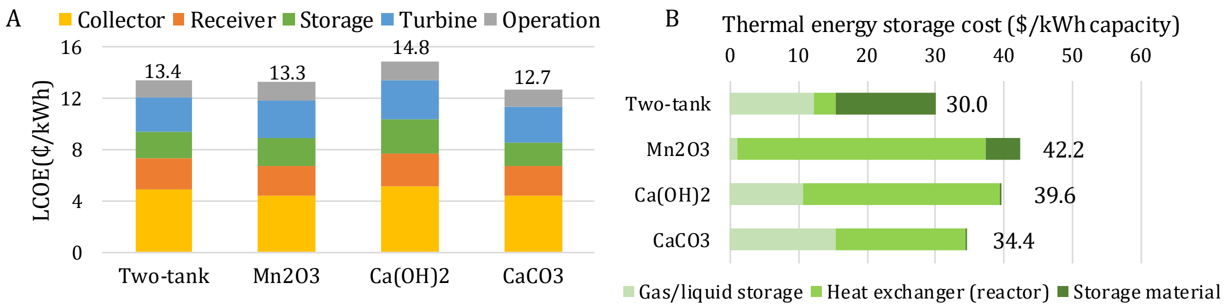

Figure 4-11. Cost distribution of (A) plant LCOE and (B) thermal energy storage.

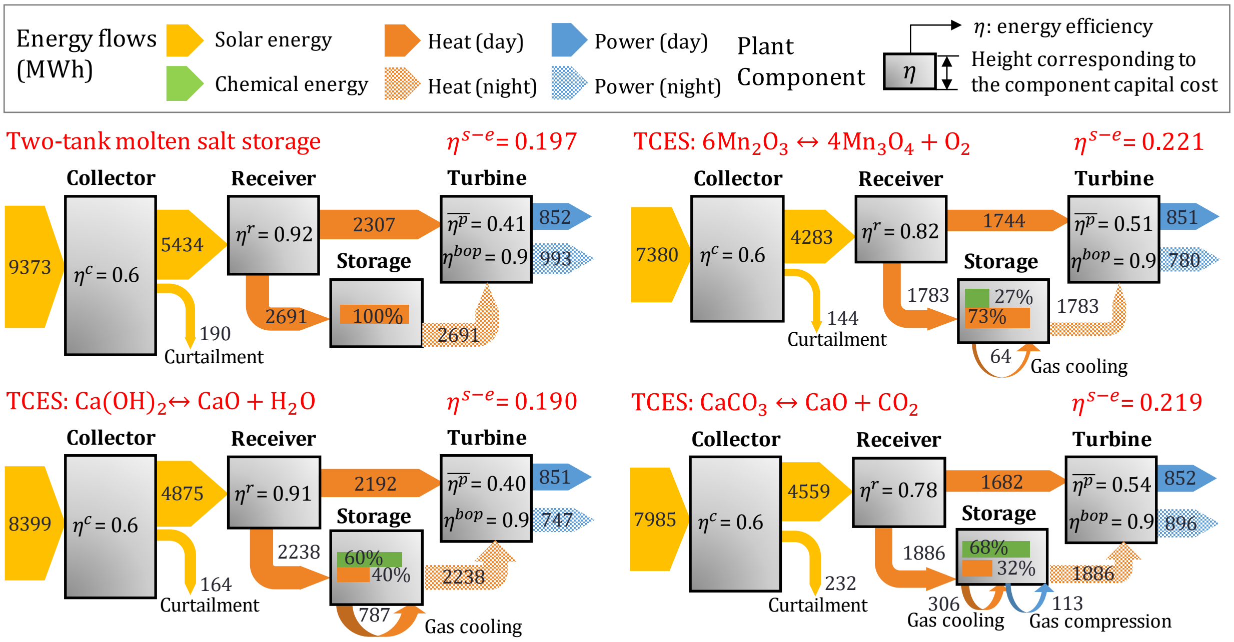

Figure 4-12. Daily energy flows in CSP plants (weighted average of six scenarios). The four plant components are shown as blocks with their energy efficiency and capital costs. Assuming no heat loss to

ambient and full gas cooling heat recovery, the storage efficiency is 100% for all cases and thus not shown inside the storage block. Instead, the percentages of sensible heat and chemical energy storage are shown.

Operational analysis To better understand the plant operation under different solar irradiance conditions, we show the daytime and nighttime power generation in six scenarios in **Figure 4-13**. Scenarios 1-6 are ranked from low to high irradiance (see **Table 3-1**). Both plants maintain 24-hour full-load operation in scenario 6. The $\mathrm{CaCO_3}$ TCES system has larger capacity and supports full-load operation in scenario 5 as well. In scenarios 2-4, the plant generates power during the day but only during a part of the night. In scenario 1, the solar input is too low to support full-time operation during the day and no power is generated during the night.

Furthermore, operating at full-load for part of the night is preferred over operating at part-load during the entire night. This is because part-load operation leads to a reduction in power cycle efficiency and thus the total produced power. The proposed model can be extended to use other objective functions (e.g., profit) and account for time-varying value of electricity.

Figure 4-13 also shows the normalized bed capacity θ in different scenarios. While the bed storage capacity is a design variable which is fixed across scenarios, θ are smaller in scenarios with longer nighttime power generation hours. Based on this analysis, we derive some general insights into the sizing of TCES fixed-bed reactors. If the reactor is relatively expensive (e.g., $\mathrm{Mn_2O_3}$ reactor), then the optimal θ is around 0.5 in high-irradiance scenarios (5 and 6), and if the reactor is relatively cheap (e.g., $\mathrm{CaCO_3}$ reactor), then the optimal θ in these scenarios is around 1.

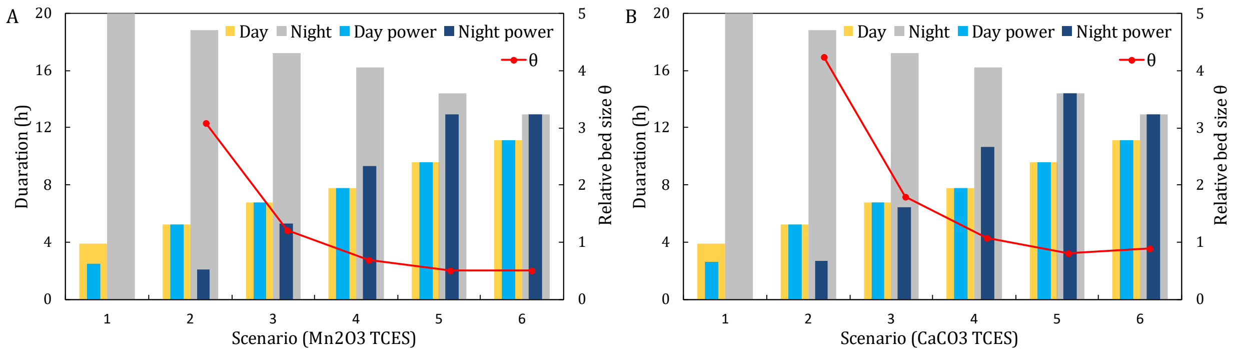

Figure 4-13. Daytime and nighttime power generation hours in six scenarios (A: Mn_2O_3 TCES, B: $CaCO_3$ TCES).

4.5 Discussion

4.5.1 Sensitivity analysis

To understand how various process parameters affect system performance, we perform sensitivity analyses for all three TCES cases (see **Figure 4-14**). First, we consider solar irradiance, which plays an important role by directly affecting the size of the solar field. A 10% decrease of solar irradiance in all scenarios results in an increase in the LCOE increases by 4% in all cases.

We then study the impacts of the prices of reactor, storage material, and gas C sensible heat storage unit. LCOE is most sensitive to the reactor cost, which is the main contributor to the storage cost (see **Figure 4-11**B). This high reactor cost is expected to decrease as the maturity of microchannel heat exchangers/reactors increases. If reactor costs decrease by 50%, the LCOE of CSP plants with Mn_2O_3 and $CaCO_3$ TCES will become 12.3 and 12.2 ₵/kWh, respectively, which is more than 1 ₵/kWh lower than the LCOE of CSP plants with two-tank storage. For Mn_2O_3 TCES, where the storage material is relatively expensive (see **Table 4-1**), the material price has a moderate impact on LCOE. The gas C heat storage price has the highest impact on $Ca(OH)_2$ TCES, where large amount of heat is released during H_2O condensation.

Finally, beyond TCES, improving collector, receiver and power cycle efficiency has been a long-term goal of CSP research. Our analysis shows that 5% increases in one of these three efficiencies could lead to a 3-8% decrease in LCOE. Power cycle efficiency typically has higher impact on LCOE than receiver and collector efficiency because its improvement benefits all upstream components.

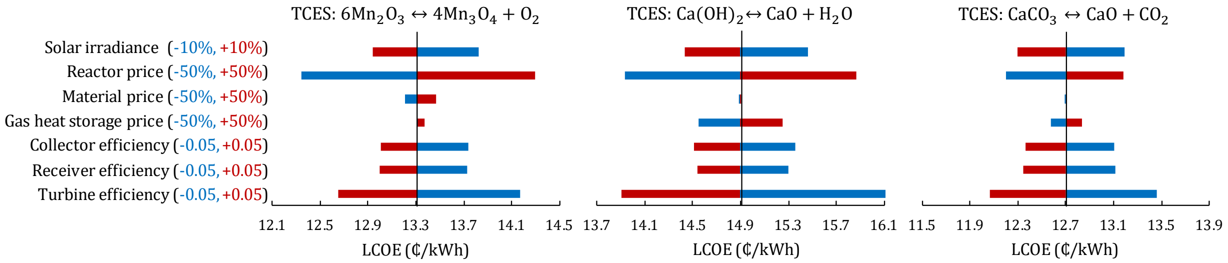

Figure 4-14. Sensitivity of LCOE with respect to different process parameters.

4.5.2 Reaction properties

We summarize how reaction properties affect storage costs and energy efficiencies in **Table 4-5**. The first key reaction property is T^{eq}, which determines the operating temperatures of the receiver and turbine as well as their efficiencies η^p and η^r. In the range of 700-1473K, increasing T^{eq} leads to an increase in $(\eta^p \cdot \eta^r)$ and thus higher overall plant efficiency η^{s-e}. However, since gas C needs to be cooled down from T^{eq} to storage temperature, an increase in T^{eq} also results in larger sensible heat storage unit (i.e., higher gas storage cost).

The second property is reaction kinetics (i.e., k_0, Ea), which determines the reaction rate. Faster reactions lead to higher bed conversion χ, higher bed storage density and thus smaller bed. However, since more energy is stored as chemical energy, more gas C is generated and stored, resulting in an increase in the gas storage cost.

Higher reaction enthalpy (ΔH^{rxn}) or solid heat capacity (Cp_A) means that more reaction or sensible heat can be stored using the same amount of storage materials. This leads to a smaller bed and reductions in all three types of storage costs. Increasing the gas heat capacity (Cp_C)/stoichiometric coefficient of C (ν_C) would increase the gas heat storage demand/the amount of C generated, both leading to a higher gas storage cost.

Next, high solid conductivity (k_A) means high heat transfer effectiveness (κ) and hence more efficient power generation (i.e., high η^p), as suggested by the correlation between κ and γ (see **Figure 4-10**A). Also, with high k_A, larger distance between tubes and less fins are needed, leading to a reduction in reactor cost. Finally, lower material price reduces the material cost but its effect on overall LCOE may be limited, as indicated in the sensitivity analysis (see **Figure 4-14**).

Table 4-5. The effects of reaction properties on storage cost and energy efficiency. [a]

Reaction property	TCES storage cost			Energy efficiency	
	Reactor	Gas/Liquid storage	Storage material	η^r	η^p
Equilibrium temperature (T^{eq})	0	−	0	−	+
Kinetics (k_0, $-Ea$)	+	−	+	0	0
Reaction enthalpy (ΔH^{rxn})	+	+	+	0	0
Solid heat capacity (Cp_A)	+	+	+	0	0
Gas heat capacity (Cp_C)	0	−	0	0	0
Stoichiometric coefficient of C (ν_C)	0	−	0	0	0
Solid conductivity (k_A)	+	0	0	0	+
Material price	0	0	−	0	0

a. + suggests that increasing the specific reaction property is beneficial to the process performance (i.e., reduction in cost or increase in energy efficiency); − suggests that increasing this reaction property is detrimental to the process performance (i.e., increase in cost or decrease in energy efficiency); and 0 suggests that the reaction property has no significant effect on the performance.

4.6 Conclusion

In this work, we developed models to simultaneously optimize the design and operation of CSP-TCES systems and provided a high-level analysis for three types (redox, hydroxide, and carbonate) of solid-gas TCES chemistries. Results show that CSP employing $6Mn_2O_3 \leftrightarrow 4Mn_3O_4 + O_2$ TCES has the highest solar-to-electricity energy efficiency and CSP with $CaCO_3 \leftrightarrow CaO + CO_2$ TCES has the greatest LCOE reduction potential over two-tank molten salt storage.

The fixed-bed reactor is identified as the major cost driver because of the ultra-small tube diameter (i.e., large heat exchange area) required for efficient heat transfer between fluids and the fixed bed. This cost can be potentially reduced by advances in microchannel heat exchanger/reactor technologies. Gas reactant storage, including sensible heat storage units, gas storage vessels, as well as compressors and turbines, is identified as the second cost driver.

Finally, we evaluated the impacts of key process parameters and reaction properties. Ideal reaction candidates for TCES should have the following characteristics, ranked from high to low importance: high T^{eq}, large ΔH^{rxn}, fast kinetics and low material price. By providing insights for fixed-bed reactor design, evaluating performance of integrated CSP plants, and identifying key areas for future research, we hope that our study will help accelerate TCES development and solar power deployment.

Chapter 5

Optimization and System Analysis of Solid-gas TCES Strategies[5]

5.1 Introduction

While considerable work has been done in reaction selection, there are limited system-level studies for CSP integrated with solid-gas TCES systems (hereinafter referred to as "CSP-TCES" systems). As a result, it remains unclear what is the best process configuration for CSP-TCES systems. Accordingly, the goal of this work is to study the system performance of different TCES strategies using an optimization-based process model. Specifically, we determine (1) what are the potential solid-gas TCES process configurations, (2) how a specific combination of reaction and process configuration impacts the CSP-TCES performance under seasonal variability, and (3) given the properties of a reversible reaction, how to select the optimal configuration for this reaction.

The remaining of this chapter is structured as follows. In **Section 5.2**, we identify four key process characteristics and propose six process configurations. In **Section 5.3**, we present process flowsheets for the proposed configurations and an optimization-based process model used for our analyses. In **Section 5.4**, we present the results for all TCES strategies, including their optimal design, energy efficiency, and cost. Finally, in **Section 5.5**, we analyze the impacts of key reaction and process properties.

---

[5] The contents of this chapter appear in Peng, Yao, Root and Maravelias, *Energy Environ. Sci*. **submitted**

5.2 TCES process and strategy

5.2.1 TCES process characteristics

Figure 5-1 shows a CSP plant which comprises of four components: the solar field (i.e., collector), receiver, TCES system and power cycle. During the day, the collector focuses sunlight onto a receiver, where photons are absorbed and converted into heat. Part of the heat is delivered to the power block for power generation while the other part is converted to chemical energy and stored in TCES for night use. The key units of a TCES system are two reactors: R1, where the solar heat drives an endothermic reaction (A (s) → B (s) + C (g)); and R2, where the reverse exothermic reaction takes place and heats up the power cycle working fluid (WF). To systematically describe a TCES system and its integration within a CSP plant, we identify four key process characteristics, which are further discussed in the following subsections.

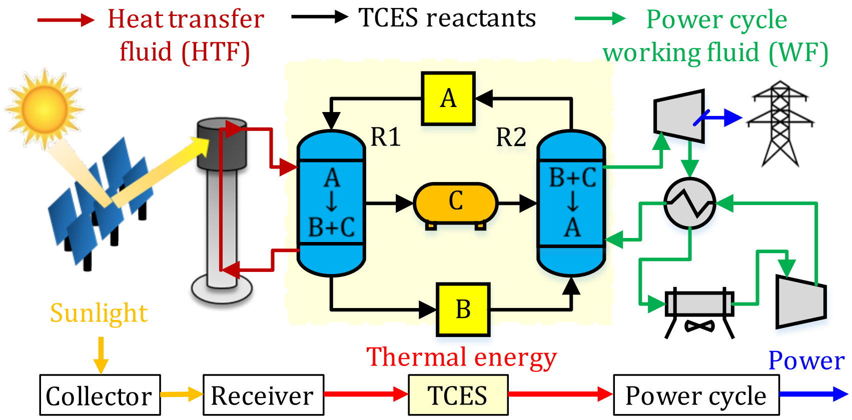

Figure 5-1. Schematic diagram of a CSP plant with solid-gas TCES system.

Solar irradiation on R1

Reactor R1 can be directly or indirectly irradiated. Directly irradiated R1 have concentrated sunlight incident upon the reactants, while reactants in indirect irradiated R1 are not exposed to solar irradiation. Instead, a heat transfer fluid (HTF) is heated in the solar receiver and then transfers the heat to R1. Requiring the HTF between the receiver and reactor, indirect irradiated R1 has more heat-transfer resistance than direct irradiated R1 but maintains a more uniform temperature distribution and minimizes the thermal shocks inside the reactor chamber.[85]

Heat transfer between R2 and power cycle

Two options are available for the heat exchange between reactor R2 and the WF. The reactor, where its reactants have direct contact with the WF, is referred to as “direct R2”; and the reactor, where reactants have indirect contact with the WF (e.g., using a shell-and-tube heat exchanger), is referred to as “indirect R2”. Although indirect R2 may have slower mass and heat transfer than direct R2, it has the following advantages:

(1) Indirect R2 is compatible with all types of HTF/WF (e.g., liquid) while direct R2 can only employ reactant gas C as both HTF and WF.

(2) By maintaining the physical separation between reactants and the WF, the R2 and power cycle can operate at different pressures. This is important because the solid-gas reactions typically take place at low pressure (~1 bar) while the WF is at high pressure (200-300 bar).

(3) Indirect contact reduces the risks of introducing impurities (e.g., solid reactants) in the WF and thus leads to safer turbine operation.

In summary, indirect R2 can be more readily integrated in a CSP-TCES facility and is therefore selected in this study.

Reactor operating mode

Reactors R1 and R2 can be continuous or fixed-bed reactors. Continuous reactors (e.g., moving beds, fluidized beds) operate at a steady state with reactants flowing in and products flowing out. The particle movement leads to a more uniform temperature distribution and enhances heat and mass transfer.[56] On the other hand, fixed-bed reactors operate at a cyclic batch mode with solid reactants packed inside and HTF/WF going through the bed. During charging, the reaction zone and temperature front move forward with the continuous supply of hot HTF. During discharging, the directions of the cold WF and hence the temperature front are reversed. The fixed-bed reactor is the most experimentally tested reactor type because it is easy to design and operate.

Gas storage

The configuration of a TCES system can have a closed-loop or open-loop structure, depending on whether the gas phase reactant C is stored in a vessel or directly emitted from R1. In this study, we use the closed-loop structure for carbonate ($\mathrm{C} = \mathrm{CO_2}$) and hydroxide ($\mathrm{C} = \mathrm{H_2O}$) systems, and the open-loop structure for redox ($\mathrm{C} = \mathrm{O_2}$) systems. Using atmospheric air as the source of oxygen for R2, open-loop configurations have no need for pressure vessels and compression for gas storage, which are the main cost and energy drivers for fluid-phase TCES systems.[168]

5.2.2 TCES strategy

In the previous subsection, we introduced two options for each of the four process characteristics: direct/indirect irradiated R1 (DR1/IR1), direct/indirect R2 (DR2/IR2), continuous/fixed-bed reactor (CON/FIX), and closed-loop/ open-loop structure (CL/OL). A process configuration is the outcome of four option selections. For example, the process in **Figure 5-1** is based on the selection of IR1, IR2, CON and CL. **Figure 5-2** shows the six out of 2^4 configurations selected in this study. The other configurations are not selected because (1) only indirect R2 is selected and (2) fixed-bed reactors, which require HTF flowing through, can only use indirect R1.

A TCES strategy is defined as a combination of a reversible reaction and a process configuration. Based on the review in **Section 1.3.1**, we select one representative reaction from each reaction type (see

Table 5-1). TCES systems based on $CaCO_3$/CaO and $Ca(OH)_2$/CaO reactions employ three configurations with a closed-loop structure, while those based on Mn_2O_3/Mn_3O_4 reaction employ the other three configurations with an open-loop structure, leading to nine strategies in total (see **Figure 5-2**).

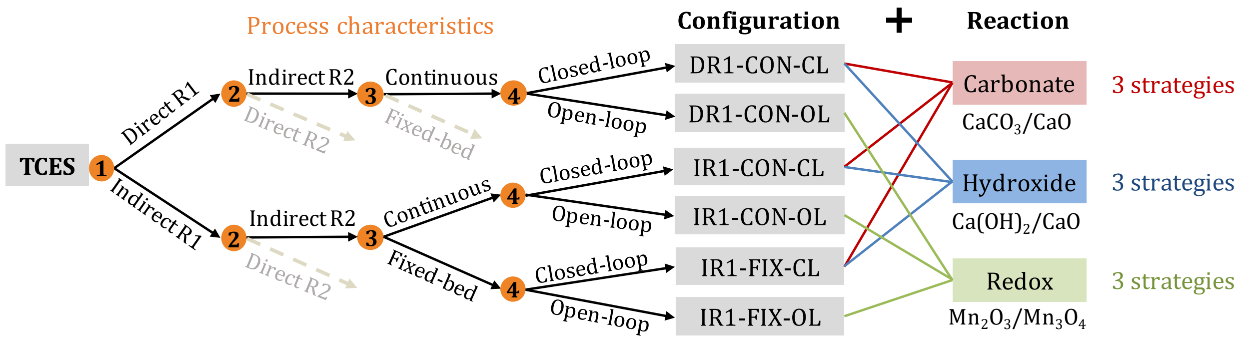

Figure 5-2. TCES strategies as combinations of configurations and reactions. Each orange circle represents a process characteristic, which branches into its two possible options. Since only indirect R2 is selected, each process configuration is described by the other three process characteristics connected with dashed lines.

Table 5-1. Selected reactions and their key properties.

Type	A(s) ↔ B(s)+ C(g)	T^{eq}* (°C)	ΔH^{rxn} (kJ/kg A)
Carbonate	$CaCO_3 \leftrightarrow CaO + CO_2$	895	1779
Hydroxide	$Ca(OH)_2 \leftrightarrow CaO + H_2O$	505	1409
Redox	$6Mn_2O_3 \leftrightarrow 4Mn_3O_4 + O_2$	821	202

*T^{eq} is the reaction equilibrium temperature at gas pressure of 1 bar. For redox reactions, O_2 partial pressure in air is 0.21 bar. ΔH^{rxn} is the reaction enthalpy.

5.3 Process modeling

5.3.1 Process flowsheets of CSP-TCES

We generate process flowsheets for the six selected CSP-TCES system configurations (see **Figure 5-3**). Unlike traditional chemical plants, CSP plants operate in two modes (i.e., day and night). Some units, such as reactor R1, operate only during the day; while some units, such as reactor R2, run during both day and night but could be operated under different conditions. To guarantee operational feasibility, all units are designed at the maximum required size over daily and seasonal variability in solar irradiance.

To attain high HTF temperature and power block efficiency, all configurations use s-CO_2 as HTF and WF, and s-CO_2 Brayton cycle for power generation (see **Section 4.2.2**). The TCES systems have five types of units, classified based on the tasks they perform (shown with different colors in **Figure 5-3**). The main differences between configurations are the following:

(1) DR1 vs IR1: Direct irradiated R1 is located at the top of a tower and a lifting conveyor is required to transport reactant A from solid storage tank A to R1. Indirect R1, where reaction heat is provided by HTF, can be placed on the ground. Also, for indirect R1, HTF delivers heat to WF during the day and R2 delivers heat only during the night. Thus, endothermic and exothermic reactions can take place alternately during day and night in the same reactor.

(2) CON vs FIX: Continuous reactors are typically smaller than fixed-bed reactors, where all solid reactants are packed inside the bed. However, continuous reactors require extra solid storage vessels for both A and B as well as conveyors for solid transportation between reactors and tanks.

(3) CL vs OL: In an open-loop structure, no gas storage vessel is needed while in a closed-loop structure, H_2O and CO_2 are stored in water vessels (1 bar, 25℃) and CO_2 vessels (75 bar, 25℃), respectively. Carbonate TCES also requires a compressor for storage charging and a turbine for power generation via CO_2 expansion during discharging. The endothermic reaction in R1 typically occurs at high temperature but C is expected to be stored or emitted at low temperature to reduce the storage volume or heat loss. Thus, heat released during gas cooling is stored in a sensible heat storage unit and reused to preheat C during the night.

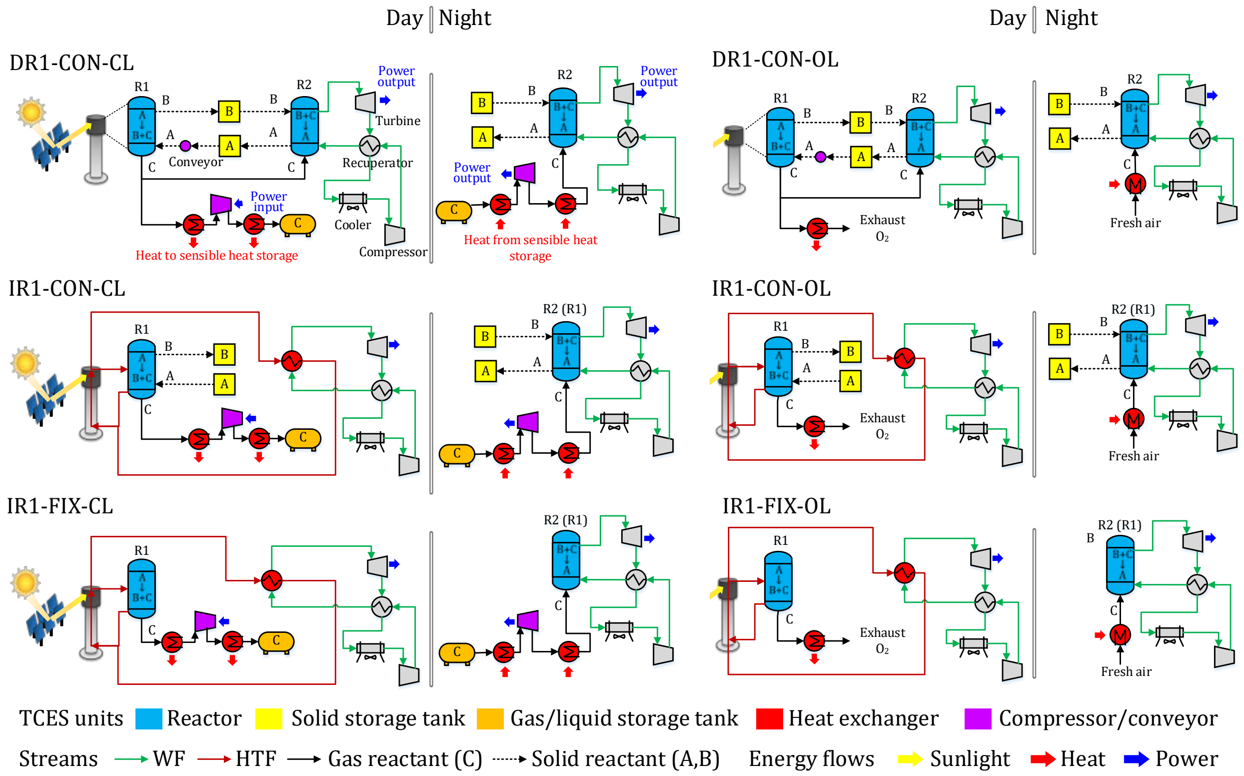

Figure 5-3. Process flowsheets of different CSP-TCES process configurations.

5.3.2 Optimization model

Peng et al. developed a general process model for CSP plant with fluid-phase TCES systems[168] and an optimization-based framework for process synthesis under seasonal and daily variability[196]. Building upon these two works, we develop an optimization model (as shown in **Figure 5-4**) for the design of CSP plants with solid-gas TCES systems. The complete list of parameters, variables and equations is given in the **Appendix A4.3**.

The first type of input is the TCES strategy. For the selected reaction, its material properties (e.g., material cost, density, specific heat capacity) and reaction characteristics (e.g., reaction enthalpy, kinetics) are given as parameters. For the selected process configuration, its flowsheet serves as a basis for expressing mass and energy balances as well as operational constraints. The other inputs include plant specifications (e.g., plant location and nameplate capacity), weather data and cost assumptions. In this study, all TCES strategies are implemented in a 100 MW CSP plant with power tower configuration. Daggett in southern California (34.87°N,116.78°W) is selected as the plant location and its weather data is obtained from the National Solar Radiation Data Base.[194] To consider the seasonal variability in solar irradiance, we generate six representative scenarios (i.e., days) from the annual data using centroid clustering algorithm[196]. The sun hours, solar irradiance and occurrence frequency of each scenario are provided in **Table 3-1**.

The main constraints of the model arise from the physical model of plant components, unit mass and energy balances, as well as equipment sizing and costing calculations. The objective is to minimize the overall levelized cost of electricity (LCOE), though a different objective can be readily used. The optimization model is a nonlinear programming (NLP) model, formulated in GAMS (28.1.0) and solved using global optimization solver BARON (19.7.13)[197]. By solving the model, we obtain the design decisions (e.g., collector area and all equipment sizes) and scenario-specific operational decisions (e.g., storage hours, flow rates, unit operating temperatures and pressures) that yield the minimum LCOE.

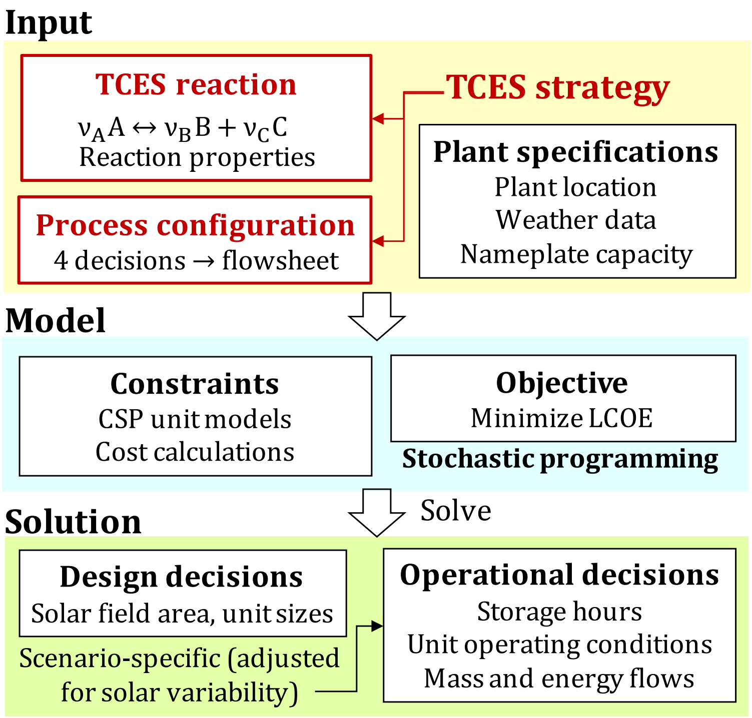

Figure 5-4. Overview of the optimization-based CSP-TCES process model.

5.4 Results

The proposed model is used to optimize the design and operation of CSP plants with the nine solid-gas TCES strategies. For each strategy, we present its optimal design and the corresponding LCOE and energy efficiency. We also compare their performance against commercially developed CSP plants which employ two-tank molten salt storage.

5.4.1 Energetic analysis

The primary energetic metric we use is the overall solar-to-electricity efficiency (η^{s-e}), defined as the ratio of net electricity output to solar energy input. It depends on block efficiencies of the four plant components. As shown in **Figure 5-5**, receiver efficiency (η^r) decreases with increasing receiver temperature (T^r), and power cycle efficiency (η^p) increases with increasing turbine inlet temperature (T^p). The heat transfer process of the TCES system is illustrated in **Figure 5-6**. During the day, reactant A is heated up and then converted to B in R1 by absorbing the heat from HTF; during the night, B is cooled down and converted back to A in R2 by releasing heat to WF. Heat is stored in the form of both chemical and sensible energy. We impose modeling constraints to prevent the violation of the second law of thermodynamics during heat transfer (details see **Appendix A4.2**). **Figure 5-6** shows the relation between operating temperatures,

$$T^r = T_{HTF} > T_{R1} > T^{eq} > T_{R2} \tag{5-1}$$

where T_{R1} and T_{R2} are the endothermic and exothermic reaction temperatures. T^p lies between T_{R1} and T_{R2} and moves towards T_{R2} as the fraction of chemical energy storage increases. Since T^r is always higher than T^p, it is impossible to have both low T^r (i.e., high η^r) and high T^p (i.e., high η^p). **Figure 5-5** shows how $\eta^r \cdot \eta^p$ changes with T^r at two different $T^r - T^p$ (0℃ and 100℃). In general, CSP plants that have high η^{s-e} need to satisfy two conditions:

- Condition 1: have T^r as high as possible in the range of 500-1200 ℃.
- Condition 2: have small exergy losses during heat transfer (i.e., small $T^r - T^p$).

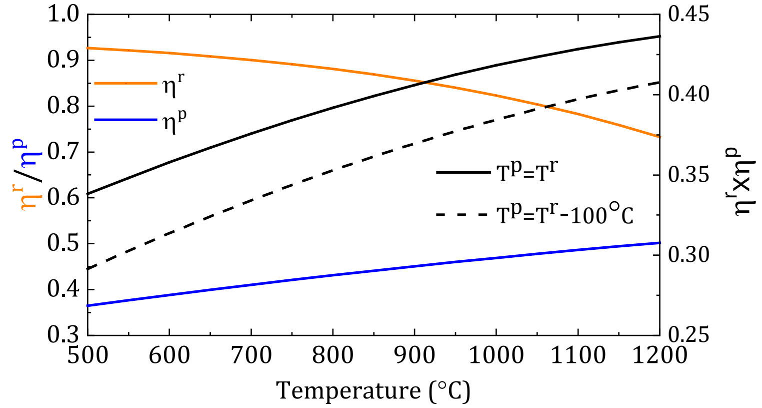

Figure 5-5. Receiver (orange) and power cycle efficiency (blue) as a function of temperature.

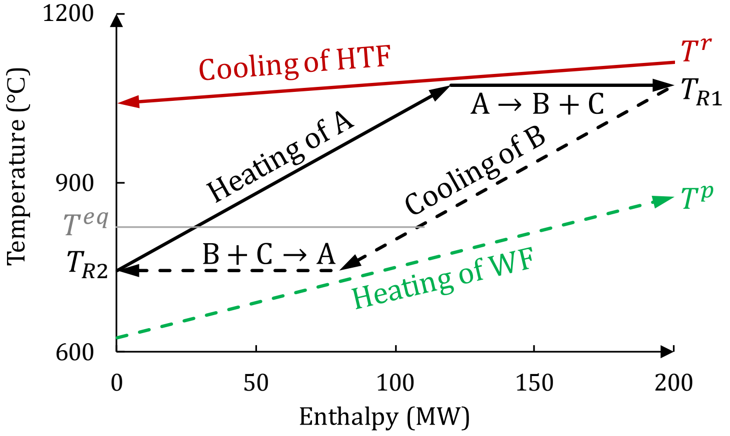

Figure 5-6. Temperature-enthalpy diagram of heat transfer between HTF and R1 during the day (solid lines), and between WF and R2 during the night (dashed lines).

For each TCES strategy, its key operating temperatures and energy efficiencies are shown in **Table 5-2** and the corresponding detailed energy flows are shown in **Figure 5-7**. **Table 5-2** shows that CSP with $\mathrm{CaCO_3}$ or $\mathrm{Mn_2O_3}$TCES have higher η^{s-e} than that with two-tank storage or $\mathrm{Ca(OH)_2}$ TCES. Also, importantly, the configurations that have the highest η^{s-e} are different for the three representative reactions (e.g., DR1-CON-CL for $CaCO_3$ and IR1-FIX-OL for Mn_2O_3). Based on the two conditions for high η^{s-e}, we can investigate the impact of two reaction properties and two process characteristics on η^{s-e}:

(1) Reaction equilibrium temperature (T^{eq}): In order to have a small $T^r - T^p$ (Condition 2), operating temperatures T^r, T_{R1}, T_{R2}, and T^p should all be in the neighborhood of T^{eq} (see eqn (5-1)). Then based on Condition 1, a high T^{eq} tends to result in a high η^{s-e}. T^{eq} of the three reactions are $\mathrm{CaCO_3(895°C) > Mn_2O_3(821°C) > Ca(OH)_2(505°C)}$, which explains their ranks in terms of η^{s-e}.

(2) Reaction kinetics: TCES reactions should be fast to enable rapid heat absorbing from HTF and heat releasing to WF, as well as short reactor residence time (i.e., small reactors). The reaction rate depends on both the reaction rate constant and the thermodynamic driving force (i.e.,

$T_{R1} - T^{eq}$ for endothermic reaction and $T^{eq}-T_{R2}$ for exothermic reaction). To achieve the same reaction rate, reactions with larger rate constants need smaller $T_{R1}-T_{R2}$ and thus have higher η^{s-e} based on Condition 2. The ranking of the three reactions in terms of rate constant is $\mathrm{CaCO_3} > \mathrm{Ca(OH)_2} > \mathrm{Mn_2O_3}$. The detailed kinetic and reactor models are provided in **Appendix A3.1** and **A4.2**.

(3) DR1 vs IR1: Compared to directly irradiated R1 ($T^r = T_{R1}$), indirect irradiated R1 has one more heat transfer between HTF and R1 ($T^r = T_{HTF} > T_{R1}$), which may lead to a larger $T^r - T^p$. However, IR1 has the advantage, over DR1, that its HTF directly delivers heat to WF during the day, leading to a small $T^r - T^p$ (10°C) and high η^p. Thus, IR1 is better suitable for slow reactions (e.g., $\mathrm{Ca(OH)_2}$), whose efficiency is limited by large thermal dynamic driving force.

(4) CON vs FIX: For each strategy, the fractions of chemical and sensible energy storage in TCES are shown in **Figure 5-7**. Compared to continuous reactors, fixed-bed reactors have lower fraction of chemical energy storage because only a small fraction of the bed reaches the equilibrium temperature and reacts. Less chemical energy storage in FIX means T^p is closer to T_{R1}, resulting in a higher T^p and smaller $T^r - T^p$. However, the cyclic batch operation of fixed-bed reactors has a disadvantage that the bed and WF temperatures, as well as η^p, all decrease during discharging (see **Table 5-2**). In summary, FIX is more advantageous for slow reactions with large $T_{R1}-T_{R2}$ requirement so the elevation in T^p outweighs its decrease during discharging.

Table 5-2. Operating conditions and energy efficiencies of different strategies.

Storage system	T^r (°C)		T_{R2}	T^p (°C)		η^r	$\overline{\eta^p}$ *	η^{s-e}
	T_{HTF}	T_{R1}	(°C)	Day	Night			
Two-tank	565	-	-	565	565	0.92	0.41	0.197
$CaCO_3$ + DR1-CON-CL	-	921	884	880	880	0.85	0.51	0.226
$CaCO_3$ + IR1-CON-CL	990	912	884	980	879	0.83	0.52	0.225
$CaCO_3$ + IR1-FIX-CL	1100	Bed: 456-1097		1100	615-1100		0.54	0.219
$Ca(OH)_2$ + DR1-CON-CL	-	793	495	527	527	0.88	0.38	0.174
$Ca(OH)_2$ + IR1-CON-CL	940	878	495	930	536	0.84	0.44	0.192
$Ca(OH)_2$ + IR1-FIX-CL	650	Bed: 118-650		650	261-650		0.40	0.190
Mn_2O_3 + DR1-CON-OL	-	1088	789	919	919	0.79	0.52	0.210
Mn_2O_3 + IR1-CON-OL	1112	1072	745	1102	875	0.78	0.53	0.216
Mn_2O_3 + IR1-FIX-OL	1000	Bed: 552-1000		1000	769-1000		0.51	0.221

* $\overline{\eta^p}$ is the energy weighted average of daytime and nighttime power cycle efficiency.

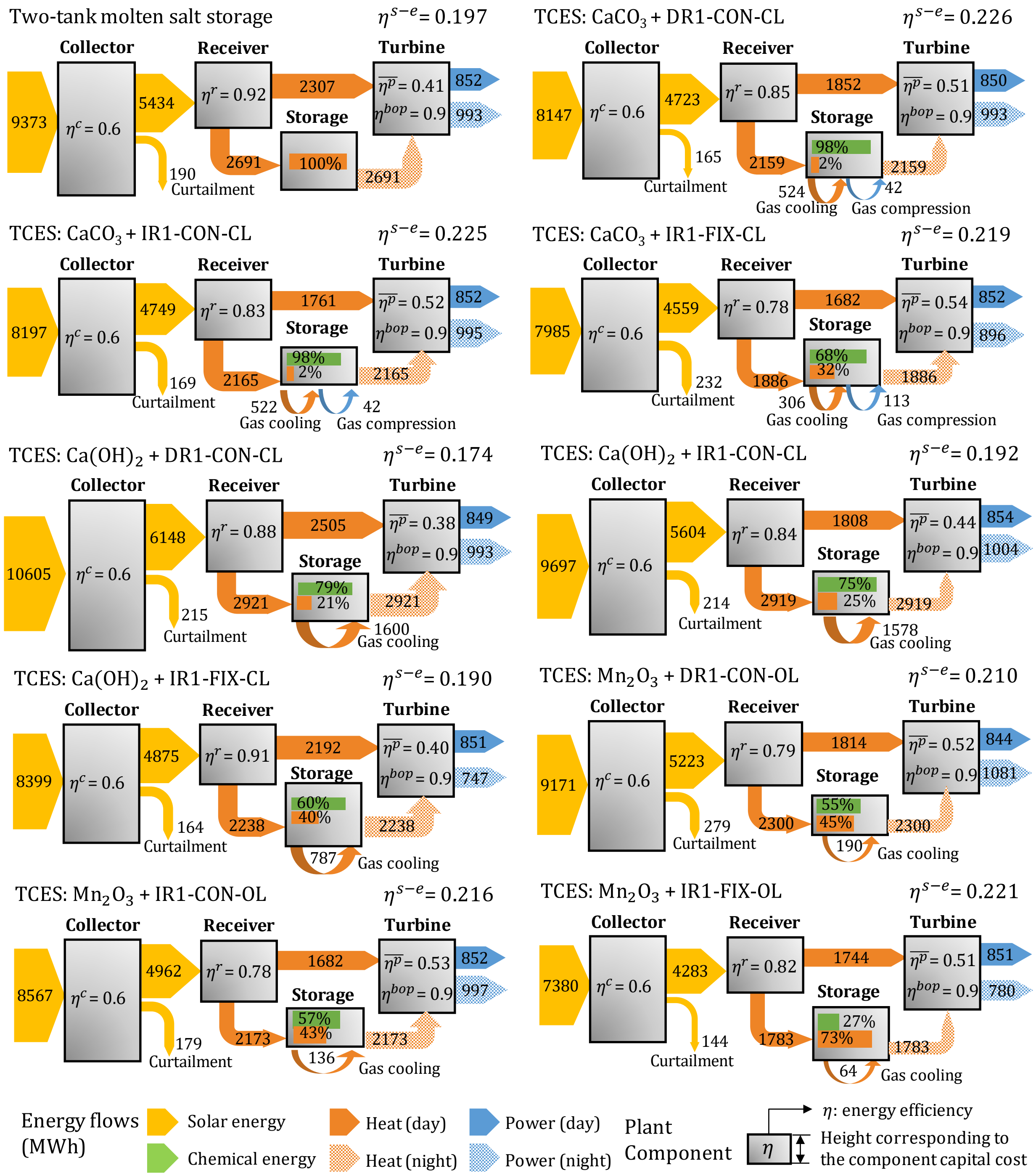

Figure 5-7. Daily energy flows in CSP plants (weighted average of six scenarios). The four plant components are shown as blocks with their energy efficiency and capital costs. A constant collector efficiency (η^c) of 0.6 is assumed. Assuming no heat loss to ambient and full gas cooling heat recovery, the storage efficiency is 100% for all strategies and thus not shown inside the storage block. Instead, the percentages of sensible and chemical energy storage are shown.

5.4.2 Economic analysis

Levelized cost of electricity (LCOE) is used as the primary economic metric and optimization objective for the design of all CSP plants with TCES. LCOE is defined as follows,

$$LCOE = (TIC \cdot CRF + OPEX)/(365 \cdot W^{ele}) \tag{5-2}$$

where *TIC*, the total installed cost, includes direct and indirect capital costs of the collector, receiver, turbine and all units in the TCES system; *CRF* is the capital recovery factor used to calculate the annual capital cost. Assuming a 9% interest rate and 30 years plant operation, *CRF* is 0.1; and *OPEX* is the annual operation and maintenance cost. The cost assumptions are given in **Table 5-3**.

Table 5-3. Major cost assumptions.

Item		Price
Equipment cost	Collector	$200\ \$/\mathrm{m}^2$
	Receiver	$175\ \$/\mathrm{kW_t}$
	Turbine	1200 \$/kW
	Sensible storage	$30\ \$/\mathrm{kWh_t}$
	Fluidized bed reactor	$5000\ \$/\mathrm{m}^3$
	Fixed bed reactor	$500\ \$/\mathrm{m}^3$
	Solid storage	$1800\ \$/\mathrm{m}^3$
	Water or liquid CO_2 storage	$100\ \$/\mathrm{m}^3$
	Heat exchanger	$100\ \$/\mathrm{m}^2$
	Conveyor	1000 \$/kW
	Compressor	1000 \$/kW
	Pump	200 \$/kW
Material cost	$CaCO_3$	100 \$/ton
	$Ca(OH)_2$	150 \$/ton
	Mn_2O_3	1000 \$/ton
Direct capital cost = Total equipment cost + Material cost + Contingency cost		
Contingency cost = 7% of total equipment cost		
Total installed cost (*TIC*) = Direct capital cost + Indirect capital cost		
Operation cost *(OPEX)*		
Fixed operation cost		65 \$/kW/y
Variable operation cost		3.5 \$/MWh

The optimal LCOEs of all cases are shown in **Figure 5-8**. Notably, seven out of the nine TCES systems lead to 0.1–1.5 ₵/kWh LCOE reductions compared to CSP plants with two-tank storage. CSP plants with $\mathrm{CaCO_3}$ and $\mathrm{Mn_2O_3}$ TCES systems have lower LCOE than those with $Ca(OH)_2$ systems. This is mainly because $\mathrm{CaCO_3}$ and $\mathrm{Mn_2O_3}$ TCES systems result in higher η^{s-e} (see **Table 5-2**) and thus require less input energy (i.e., smaller solar field and receiver) to produce the same amount of electricity.

The detailed cost distributions for the storage system are shown in **Figure 5-9**. The storage costs range from 21–42 $/kWh. Configuration IR1-FIX has significantly higher TCES cost than DR1-CON and IR1-CON because fixed-bed reactors are more expensive than continuous reactors due to: (1) large reactor volume because all solid reactants packed in the bed, and (2) large heat exchange area to ensure efficient heat transfer between fluids and the fixed bed (see **Chapter 4**).

For configurations employing continuous reactors, the main cost drivers are different for the three reactions. In $\mathrm{CaCO_3}$ TCES systems, the compressor for CO_2 storage and the turbine for electricity generation during CO_2 expansion account for 60% of the TCES cost since CO_2 is stored at 75 bar. In $Ca(OH)_2$ TCES systems, the sensible heat storage unit is the main cost driver because a large amount of heat needs to be stored during the cooling process of H_2O where phase change occurs. $\mathrm{Mn_2O_3}$ TCES systems with open-loop configurations, have lower costs associated with gas storage but higher solid storage costs. More solid reactants are needed in $\mathrm{Mn_2O_3}$ TCES because ΔH^{rxn} of the $\mathrm{Mn_2O_3}$ reaction (202 kJ/kg) is significantly lower than $Ca(OH)_2$ (1409 kJ/kg) and $\mathrm{CaCO_3}$ (1779 kJ/kg) reactions. In two-tank TES, storage material (molten salt) is the main cost driver, while in TCES systems, material costs are significantly lower, especially for $Ca(OH)_2$ and $\mathrm{CaCO_3}$ TCES, due to their low material price and high storage density.

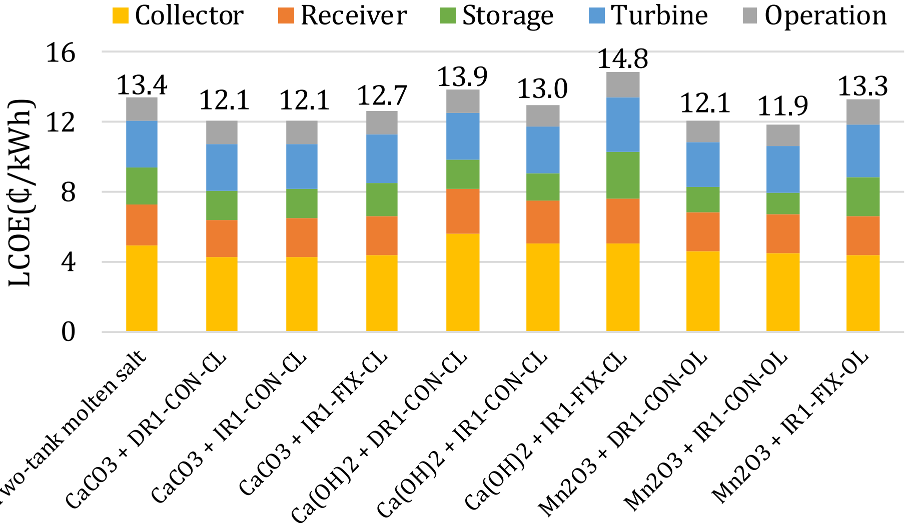

Figure 5-8. LCOE distribution of CSP plants with two-tank or thermochemical storage.

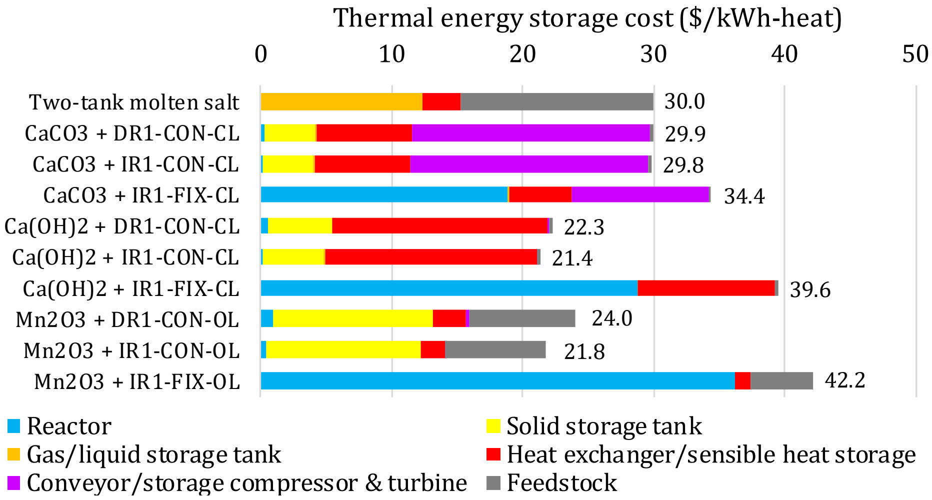

Figure 5-9. Cost distribution of thermal energy storage systems.

5.5 Discussion

5.5.1 Performance metrics

We summarize the key performance metrics of all storage strategies in **Figure 5-10**. Each strategy is shown as a sphere, centered at its values of η^{s-e} (x-axis) and LCOE (y-axis). Desirable storage systems (i.e., those with low LCOE and high η^{s-e}) will appear in the lower-right corner. The color of the sphere indicates the reaction type and its size is proportional to the total volume needed to store 1 kWh heat, including volumes of reactors, gas and solid storage vessels. A smaller sphere size means the storage system has higher volumetric energy storage density. **Figure 5-10** shows that all six $CaCO_3$ and Mn_2O_3 TCES strategies exhibit superiority over today's two-tank molten salt storage system. In particular, $CaCO_3$ +IR1/DR1-CON-OL and Mn_2O_3 +IR1-CON-OL are identified as the most promising strategies.

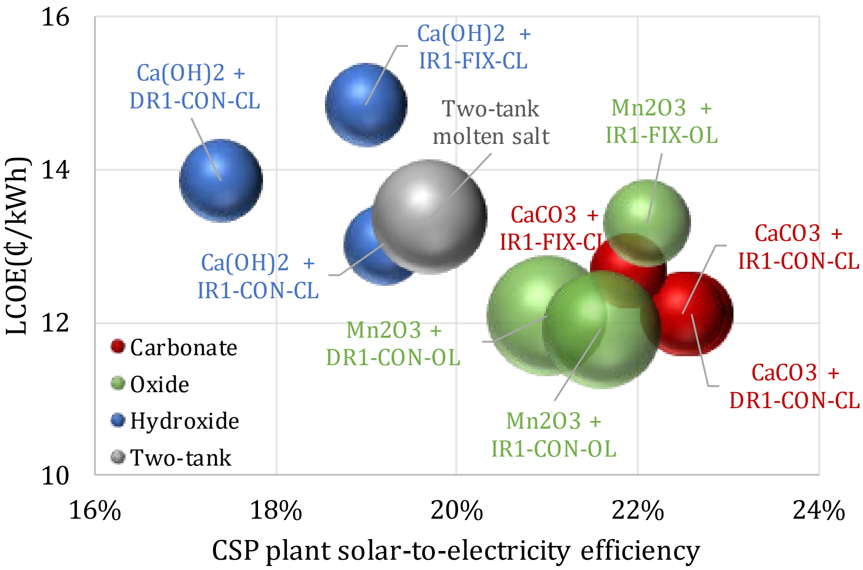

Figure 5-10. LCOE and η^{s-e} of CSP plants with two-tank storage or TCES. The sphere colors indicate the reaction type. The volume of the spheres represents the storage volume needed to store 1 kWh heat.

5.5.2 Reaction properties

We summarize the impacts of different reaction properties on storage costs and η^{s-e}. The properties are ranked in order of importance in **Table 5-4**. The most important property, T^{eq}, determines the operating range of key temperatures (i.e., $T^{r}, T_{R1}, T_{R2}, and\ T^{p}$) and thus η^{s-e} (see **Figure 5-5**). The properties of gas reactant C (e.g., boiling point, percentage in air) are also important since they have great impacts on the gas storage cost. In this study, redox TCES systems with open-loop configurations have the lowest gas storage cost. Hydroxide and carbonate TCES systems, which suffer from high sensible heat storage unit cost and high compression cost respectively, have the medium and highest gas storage costs.

Faster reactions can not only reduce reactor costs because of shorter reactor residence time, but also improve η^{s-e} due to smaller thermodynamic driving force (i.e., $T_{R1} - T^{eq}$ and $T^{eq} - T_{R2}$). Higher reaction enthalpy (ΔH^{rxn}) or solid heat capacity (Cp_A) means that more chemical or sensible heat can be stored using the same amount of storage materials, leading to reductions in storage materials and storage costs. In the meantime, increasing ΔH^{rxn} or decreasing Cp_A has a negative impact on η^{s-e} since T^p decreases as the fraction of chemical energy storage increases (see **Figure 5-6**). Material price has a limited effect on storage cost since feedstock cost is not the main cost driver (see **Figure 5-9**).

Finally, we use a decision matrix to evaluate the three reactions (see **Table 5-4**). We first assign weights to each reaction property based on its effects on costs and η^{s-e}. We then score each property from 1 (poor) to 3 (good) and calculate the weighted sum of scores for each reaction. As a result, $CaCO_3$ reaction achieves the highest score, followed by Mn_2O_3 and $Ca(OH)_2$ reactions. This result is consistent with our energetic and economic analyses (see **Figure 5-10**). This simple decision matrix can serve as an efficient tool for preliminary screening on TCES reactions. After several promising candidates are selected, system-level analyses can be further conducted to evaluate their detailed performance.

Table 5-4. Effects of reaction properties on CSP performance and decision matrix for three reactions.

TCES cost [a]	η^{s-e} [a]	Reaction properties	Weight	$CaCO_3$ [b]	$Ca(OH)_2$ [b]	Mn_2O_3 [b]
0	$+++$	Equilibrium temperature (T^{eq})	5	3	1	2
$++$	0	Gas C type (boiling point)	4	1	2	3
$+$	$++$	Kinetics (rate constant)	2	3	2	1
$++$	$-$	Reaction enthalpy (ΔH^{rxn})	1	3	2	1
$+$	$+$	Solid heat capacity (Cp_A)	1	2	3	1
$-$	0	Material price	0.5	3	2	1
		Total weighted score		31.5	23	26.5

a. $+$ suggests that increasing the specific reaction property is beneficial to the process performance (i.e., reduction in cost or increase in energy efficiency); $-$ suggests that increasing this reaction property is detrimental to the process performance (i.e., increase in cost or decrease in energy efficiency); and 0 suggests that the reaction property has no significant effect on the performance.

b. Each reaction is scored for each reaction property from 1 (poor) to 3 (good)

5.5.3 Process configurations

Finally, we summarize four general findings for the selection of TCES process configurations:

(1) Configuration IR1-CON leads to the lowest LCOE for all three reactions. IR1-CON has better economic performance than DR1-CON and IR1-FIX for two reasons. First, HTF directly exchanges heat with WF during the day, which reduces $T^r - T^p$ and enables high η^{s-e}. Second, only one continuous reactor is needed (i.e., R1 and R2 take place alternately in the same equipment), resulting in low reactor costs.

(2) The superiority of IR1 over DR1 decreases if the reaction has fast kinetics (i.e., small $T^r - T^p$) or high T^{eq} (i.e., high T^p). As illustrated in this study, the difference in performance between DR1-CON and IR1-CON is significant for $Ca(OH)_2$ reaction, which has slow kinetics and low T^{eq}, but is not obvious for Mn_2O_3 and $CaCO_3$ reactions.

(3) Compared to continuous reactors, fixed-bed reactors are significantly more expensive due to their large volume and heat exchange areas. Fixed beds will be more attractive if the reactor costs can be reduced by advances in microchannel heat exchanger/reactor technologies.

(4) For redox reactions, open-loop configurations are better than closed-loop ones by eliminating the gas storage tanks.

5.6 Conclusion

In this work, we provided a system-level analysis for nine solid-gas TCES strategies, which are the combinations of three chemistries (carbonate, hydroxide, and redox reactions) and six process configurations. The performance of these strategies was evaluated using a proposed process model, which optimizes the design of CSP-TCES systems under seasonal variability.

Results show that six out of the nine strategies have both higher η^{s-e} and lower LCOE than two-tank storage. In particular, $\mathrm{CaCO_3}$+IR1/DR1-CON-CL and $\mathrm{Mn_2O_3}$+IR1-CON-OL are identified as the most promising strategies. We also analyzed the impacts of six reaction properties on system performance. Based on the importance of these properties, a decision matrix was built for preliminary screening on reaction candidates. Finally, we identified IR1-CON-OL as the best process configuration and summarized several matching rules between reactions and configurations.

By proposing various TCES process configurations and strategies, evaluating their system performance, and providing general insights on strategy selection, we hope that our study will help accelerate the TCES development and solar power deployment.

Chapter 6

Conclusions and Future work

In this work, we developed optimization models for the design and analysis of CSP plants with fluid-phase and solid-gas TCES systems to provide guidance for future TCES development.

Specifically, we first developed a general process for CSP plants employing fluid-phase TCES systems, formulated an optimization-based model of the process, and used this model to study ammonia and methane TCES systems. We identified pressure vessels for gas storage as the main cost driver and gas compression as the main energy driver.

Next, we developed an optimization-based framework for process synthesis under variability in two frequencies. The proposed multimode stochastic programming approach yields significantly better solutions than deterministic approaches, and leads to computationally more efficient models than conventional stochastic programming approaches.

We then developed models to simultaneously optimize the design and operation of CSP with solid-gas TCES systems. For fixed-bed reactors, we conducted numerical simulations at various operating conditions and built efficient surrogate models. Finally, we provided a system-level analysis for nine solid-gas TCES strategies, which are the combinations of three chemistries (carbonate, hydroxide, and redox reactions) and six process configurations. Results show that six out of the nine strategies have both higher η^{s-e} and lower LCOE than two-tank storage. We also analyzed the impacts of key reaction properties and process parameters on system performance.

Potential future directions of this work are as follows:

1. CSP electricity market participation.

In this study, we use levelized cost of electricity (LCOE) as the economic metric, which neglects the time-varying value of electricity. LCOE may undervalue dynamic flexibility provided by thermal energy storage, which is the competitive advantage of CSP technologies.[198] Thus, it is worth exploring co-optimizing the design and market participation of a CSP system, and use revenue or net present value for economic assessments. Unfortunately, considering participation in the electricity market, especially the real-time market with 5 and 15-min intervals, together with variability in solar irradiance will result in large scale mixed-integer nonlinear optimization problems, which are computationally challenging to solve with existing tools. This challenge may be addressed by (1) constructing smaller representative weather-market data sets and formulating the problem using the multimode stochastic programming approach proposed in **Chapter 3**, (2) model simplifications, such as the surrogate models we develop for fixed-bed reactors in **Chapter 4**, and (3) exploiting problem structure and developing decomposition methods.

2. Systematic screening of potential reactions for TCES

In this study, we have used the proposed process model to assess the system performance of five representative TCES reactions (two in fluid-phase and three in solid-gas phase). In the future, we can use the general process model for a more extensive screening on a wide range of potential reactions. Currently, close to 1000 reactions have been identified as candidates and are listed in the online available VIENNA TCES-database.[199] Furthermore, by changing reaction properties from parameters to variables (with carefully designed bounds), we can solve an optimization problem to obtain an ideal combination of properties. Given the desired properties, new reaction materials can be synthesized through inverse design.

Appendix

A1 Explanations to Chapter 2

A1.1 Process model of CSP with fluid-phase TCES

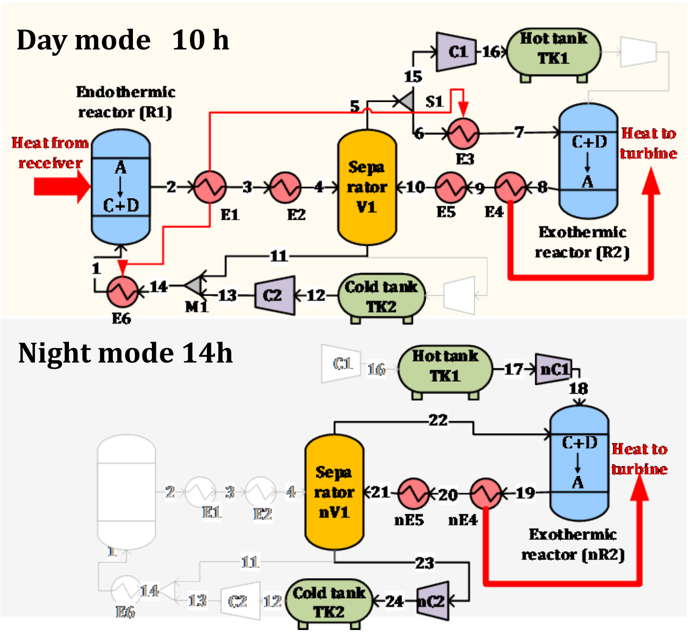

R1	Endothemic reactor
R2/nR2	Exothermic reactor
TK1	Hot storage tank
TK2	Cold storage tank
V1/nV1	Separator
C1/nC1	TK1 compressor
C2/nC2	TK2 compressor
E1	R1 cooler
E2	Separation cooler 1
E3/E6	R2/R1 preheater
E4/nE4	Steam preheater
E5/nE5	Separation cooler 2
S1	Storage splitter
M1	Mixer for R1

Figure A1-1. Process flowsheet of TCES systems with separation

Sets

$i \in \mathbf{I}$	Units
$j \in \mathbf{J}$	Streams
$k \in \mathbf{K}$	Components

Subsets

$\mathbf{I}^{\mathbf{R}}$	Reaction units {R1, R2, nR2}
$\mathbf{I}^{\mathbf{SEP}}$	Separation units {V1, nV1}
$\mathbf{I}^{\mathbf{TK}}$	Storage units {TK1, TK2}
$\mathbf{I}^{\mathbf{E}}$	Heat exchangers {E1, E2, E3, E4, E5, E6, nE4, nE5}
$\mathbf{I}^{\mathbf{C}}$	Compressor {C1, C2, nC1, nC2}
$\mathbf{J}_{\mathbf{i}}^{\mathbf{IN}}$	Inlet streams of unit i

$\mathbf{J_i^{OUT}}$	Outlet streams of unit i

Parameters

CRF	Capital recovery factor
Cp_k	Specific heat capacity of component k (J/mol-K)
DNI^{ref}	Reference direct normal irradiance (W/m^2)
h^{avg}	Average heat transfer coefficient (W/m^2-K)
MAT	Minimum approach temperature (K)
P^{rate}	CSP plant rated capacity (MW)
P^{atm}	Atmosphere pressure (bar)
R	Gas constant (J/mol·K)
ΔH^0	Reaction enthalpy at reference temperature T^0 (kJ/mol)
ΔS^0	Reaction entropy at reference temperature T^0 (J/mol-K)
$\mathrm{d}\Delta H$	Rate of reaction enthalpy changing with temperature (kJ/mol-K)
$\mathrm{d}\Delta S$	Rate of reaction entropy changing with temperature (J/mol-K^2)
T^0	Reference temperature (K)
t^{day}	Daytime operation time (h)
t^{sto}	Storage time (h)
$z_k(P)$	Compressibility of component k at pressure P
η^c	Collector efficiency
η^{comp}	Compressor motor efficiency
η^{para}	plant parasitic efficiency
λ^c	Collector price (\$/m^2 mirror aperture)
λ^r	Receiver price ($\$/kW_{thermal}$)
λ^p	Power block price ($\$/kW$)
λ^{tk}	Storage tank price ($\$/m^3$)
λ^{hx}	Heat exchanger price ($\$/m^2$)
λ^{rxn}	Reactor price ($\$/m^3$)
λ^{comp}	Compressor price ($\$/kW$)
λ^{sep}	Separation price ($\$/(\frac{mol}{s})$)
λ_k^{sm}	Storage media price of component k ($\$/ton$)
λ^{cu}	Cooling utility price (\$/kW-year)
λ^{om}	Operation and maintenance (\$/kW-year)

v_k	Stoichiometric coefficient of component *k* in the reversible reaction
τ^{rxn}	Reactor holding time (s)
ω_k	Molecular weight of component *k (g/mol)*

Variables

AREA	Solar field area (m^2)
CAPEX	Plant total capital cost ($)
C^{cu}	Cooling utility cost ($/year)
C^{tk}	Storage tank cost ($)
C^{hx}	Heat exchanger cost ($)
C^{rxn}	Reactor cost ($)
C^{comp}	Compressor cost ($)
C^{sep}	Separation cost ($)
C^{sto}	TCES system cost ($)
C^{sm}	TCES storage media cost ($)
F_j^T	Total molar flow rate in stream *j* (mol/s)
$F_{j,k}$	Molar flow rate of component *k* in stream *j* (mol/s)
LCOE	Levelized cost of electricity (ℂ/kWh)
OPEX	Operation cost per year ($/year)
P	Process pressure (bar)
P_i^H	Maximum storage pressure (bar), $i \in \mathbf{I^{TK}}$
P_i^L	Minimum storage pressure (bar), $i \in \mathbf{I^{TK}}$
PWR_i	Rated power of the compressor for storage tank i (MW) , $i \in \mathbf{I^{TK}}$
Q_i	Heat duty of unit *i* (kW)
T_j	Temperature of stream *j* (K)
T_i	Temperature of unit i (K) defined as its outlet stream T ($\mathrm{T_i} = T_j,\ \ j = \mathbf{J_i^{OUT}}$)
$\triangle \mathrm{T_{i/i'}}$	Arithmetic mean temperature difference (K) of matched heat exchangers i and i’
ΔH_i	Reaction enthalpy at the temperature of reactor i (kJ/mol), $i \in \mathbf{I^R}$
ΔS_i	Reaction entropy at the temperature of reactor i (J/mol-K), $i \in \mathbf{I^R}$
V_i	Volume of storage tank (m^3), $i \in \mathbf{I^{TK}}$
W^{comp}	Total electricity consumed by compressor per day (MWh/day)
W^{ele}	Net electricity generation per day (MWh/day)
$\overline{Z}_J$	Average compressibility of stream j

$\zeta_{j,k}$	Split fraction of component k in the outlet stream j of the separation unit
η^{r}	Receiver efficiency
η^{sto}	Storage system round-trip efficiency
$\eta^{p,day}, \eta^{p,night}, \eta^{p}$	Day, night and overall turbine efficiency
η^{s-e}	Overall solar to electricity efficiency
ξ_j^{spl}	Split fraction for outlet stream of splitter S1

Cost data

Table A1-1. Comparison of computational statistics of different approaches

Item		Price	Item		Price	Item		Price
Collector	λ^{c}	250 $\$/m^2$	Reactor	λ^{rxn}	$6500\$/m^3$	Ammonia	λ^{sm}	320 $\$/ton$
Receiver	λ^{r}	200 $\$/kW_t$	Separation	λ^{sep}	$200\$/(\frac{mol}{s})$	Methane		180 $\$/ton$
Turbine	λ^{p}	$1200\$/kW$	Heat exchanger	λ^{hx}	$50\$/m^3$	Carbone dioxide		40 $\$/ton$
Cooling	λ^{cu}	$20\$/kW$yr	Pressure vessel	λ^{tk}	$5700\$/m^3$	Compressor	λ^{comp}	1000 $\$/kW$
O&M	λ^{om}	65 $\$/kW$yr	Underground storage		$50\$/m^3$			

Model Equations

Total molar flow rate
$$F_j^T = \sum_{k \in \mathbf{K}} F_{j,k} \qquad j \in \mathbf{J} \tag{A1-1}$$

Mass balance
$$F_{j,k} = F_{j',k} \cdot \xi_j^{spl} \quad i = S1, j \in \mathbf{J_i^{OUT}}, j' \in \mathbf{J_i^{IN}}, k \in \mathbf{K} \tag{A1-2}$$

Mass balance
$$F_{j,k} = \sum_{j' \in \mathbf{J_i^{in}}} F_{j',k} \quad i = M1, j \in \mathbf{J_i^{OUT}}, k \in \mathbf{K} \tag{A1-3}$$

Mass balance
$$F_{j,k} = F_{j',k} \quad i \in \mathbf{I^E} \cup \mathbf{I^C}, j \in \mathbf{J_i^{OUT}}, j' \in \mathbf{J_i^{IN}}, k \in \mathbf{K} \tag{A1-4}$$

Mass balance
$$F_{j,k} = F_{j',k} \cdot \quad i \in \mathbf{I^{SEP}}, j \in \mathbf{J_i^{OUT}}, j' \in \mathbf{J_i^{IN}}, k \in \mathbf{K} \tag{A1-5}$$

Mass balance
$$F_{j',k} \cdot t^{day} = F_{j,k} \cdot t^{sto} \qquad i \in \mathbf{I^{STO}}, j \in \mathbf{J_i^{OUT}}, j' \in \mathbf{J_i^{IN}}, k \in \mathbf{K} \tag{A1-6}$$

Mass balance
$$\begin{gathered} (F_{j,\boldsymbol{A}} - F_{j',\boldsymbol{A}}) \cdot v_k = (F_{j,\boldsymbol{k}} - F_{j',\boldsymbol{k}}) \cdot v_A \\ i \in \mathbf{I^R}, j \in \mathbf{J_i^{OUT}}, j' \in \mathbf{J_i^{IN}}, k = \mathrm{B, C, D} \end{gathered} \tag{A1-7}$$

Reaction enthalpy

$$\Delta H_i = \Delta H^0 + (T_i - T^0) \cdot \mathrm{d}\Delta H \quad i \in \mathbf{I^R} \tag{A1-8}$$

Reaction entropy

$$\Delta S_i = \Delta S^0 + (T_i - T^0) \cdot \mathrm{d}\Delta H \quad i \in \mathbf{I^R} \tag{A1-9}$$

Reaction equilibrium

$$-RT \sum_{k \in \mathbf{K}} v_k \left[\ln\left(F_{j,k}\right) - \ln\left(F_j^T\right) + \ln\left(\frac{P}{P_{atm}}\right) \right] = \Delta H_i - T_i \Delta S_i \qquad i \in \mathbf{I^R}, j \in \mathbf{J_i^{OUT}} \tag{A1-10}$$

Unit heat duty

$$Q_i = \sum_{j \in \mathbf{J_i^{OUT}}} T_j \cdot \left(\sum_{k \in \mathbf{K}} F_{j,k} \cdot Cp_k \right) - \sum_{,j' \in \mathbf{J_i^{IN}}} T_{j'} \cdot \left(\sum_{k \in \mathbf{K}} F_{j',k} \cdot Cp_k \right) \qquad i \in \mathbf{I} \backslash \mathbf{I^R} \tag{A1-11}$$

Unit heat duty

$$Q_i = \Delta H_i \cdot \left(F_{j',A} - F_{j,A}\right) + \left(T_j - T_{j'}\right) \cdot \left(\sum_k F_{j',k} \cdot Cp_k \right) \qquad i \in \mathbf{I^R}, j \in \mathbf{J_i^{OUT}}, j' \in \mathbf{J_i^{IN}} \tag{A1-12}$$

Constant T units

$$T_{j,k} = T_{j',k} \quad i \in \mathbf{I^{STO}} \cup \{S1, M1\}, j \in \mathbf{J_i^{OUT}}, j' \in \mathbf{J_i^{IN}} \tag{A1-13}$$

No heat duty units

$$Q_i = 0 \quad i \in \mathbf{I^{SEP}} \cup \{S1, M1\} \tag{A1-14}$$

Heat integration

$$-\mathrm{Q_{E1}} = Q_{E3} + Q_{E6} \tag{A1-15}$$

Minimum approach temperature

$$\begin{gathered} \mathrm{T_2} \geq T_7 + MAT;\ \mathrm{T_3} \geq T_6 + MAT; \quad \text{(E1-E3)} \\ \mathrm{T_2} \geq T_1 + MAT;\ \mathrm{T_3} \geq T_{14} + MAT; \quad \text{(E1-E6)} \end{gathered} \tag{A1-16}$$

Mean Temperature Difference

$$\begin{gathered} \triangle T_{E1/E3} = (T_2 - T_7 + T_3 - T_6)/2 \\ \triangle T_{E1/E6} = (T_2 - T_1 + T_3 - T_{14})/2 \end{gathered} \tag{A1-17}$$

Storage tank size

$$V_i^{tank} \cdot \frac{P_i^H - P_i^L}{R \cdot T} = \overline{Z}_J \cdot F_{j'}^T \cdot t^{day} \quad i \in \mathbf{I^{STO}}, j' \in \mathbf{J_i^{IN}} \tag{A1-18}$$

Charging power

$$PWR_i \geq \overline{Z}_J \cdot F_{j'}^T \cdot T \cdot [\left(\frac{P_i^H}{P}\right)^{1.3} - 1]/\eta^{comp} \quad i \in \mathbf{I^{STO}}, j' \in \mathbf{J_i^{IN}} \tag{A1-19}$$

Discharging power

$$PWR_i \geq \overline{Z}_J \cdot F_j^T \cdot T \cdot [\left(\frac{P}{P_i^L}\right)^{1.3} - 1]/\eta^{comp} \quad i \in \mathbf{I^{STO}}, j \in \mathbf{J_i^{OUT}}$$ (A1-20)

Daily electricity for charging

$$W_i^{in} = \overline{Z}_J \cdot \{\frac{\sum_k (F_{j\prime,k} Cp_k) \cdot V_i^{tank} \cdot P}{1.3} \cdot [\left(\frac{P_i^H}{P}\right)^{1.3} - 1] - \overline{Z}_J \cdot$$

$$\sum_k (F_{j\prime,k} Cp_k) \cdot V_i^{tank} \cdot (P_i^H - P)\}/(F_{j\prime}^T \cdot R \cdot \eta^{comp})$$ (A1-21)

$$i \in \mathbf{I^{STO}}, j' \in \mathbf{J_i^{IN}}$$

Daily electricity for discharging

$$W_i^{out} = \overline{Z}_J \cdot \{\frac{\sum_k (F_{j,k} Cp_k) \cdot V_i^{tank} \cdot P}{0.7} [1 - \left(\frac{P_i^L}{P}\right)^{0.7}] - \overline{Z}_J \cdot \sum_k F_{j,k} Cp_k) \cdot$$

$$V_i^{tank} \cdot (P - P_i^L)\}/(F_j^T \cdot R \cdot \eta^{comp}) \quad i \in \mathbf{I^{STO}}, j \in \mathbf{J_i^{OUT}}$$ (A1-22)

Total daily electricity consumption

$$W^{comp} = \sum_{i \in \mathbf{I^{STO}}} (W_i^{in} + W_i^{out})$$ (A1-23)

Compression T

$$T_{j,k} = T_{j\prime,k} \quad i = \mathbf{I^C}, j \in \mathbf{J_i^{OUT}}, j' \in \mathbf{J_i^{IN}}$$ (A1-24)

Power block efficiency

$$\eta^{p,day} = 1 - \sqrt{330/T_{R2}}, \eta^{p,night} = 1 - \sqrt{330/T_{nR2}}$$ (A1-25)

Output in the day

$$-(Q_{R2} + Q_{E4}) \cdot \eta^{p,day} \cdot \eta^{\mathrm{para}} = P^{rate}$$ (A1-26)

Output at night

$$-(Q_{nR2} + Q_{nE4}) \cdot \eta^{p,night} \cdot \eta^{\mathrm{para}} = P^{rate}$$ (A1-27)

Solar field area

$$AREA = Q_{R1}/(DNI^{ref} \cdot \eta^{\mathrm{c}} \cdot \eta^{\mathrm{r}})$$ (A1-28)

Receiver efficiency

$$\eta^{\mathrm{r}} = -0.02T^{*3} - 0.08T^{*2} - 0.18T^{*} + 0.78$$

$$T^{*} = (T_{R1} - 1150)/245$$ (A1-29)

Average power block efficiency

$$\eta^p = \frac{Q_{r2} \cdot t^{day} \cdot \eta^{p,day} + Q_{nr2} \cdot t^{sto} \cdot \eta^{p,night}}{Q_{r2} \cdot t^{day} + Q_{nr2} \cdot t^{sto}}$$ (A1-30)

TCES efficiency
$$\eta^{sto} = \frac{Q_{E4} \cdot t^{day} + Q_{nE4} \cdot t^{sto} - \dfrac{W^{comp}}{\eta^{para} \cdot \eta^{p}}}{Q_{R1} \cdot t^{day}} \tag{A1-31}$$

Overall efficiency
$$\eta^{s-e} = \eta^{c} \cdot \eta^{r} \cdot \eta^{sto} \cdot \eta^{p} \cdot \eta^{para} \tag{A1-32}$$

Compressor cost
$$C^{comp} = \lambda^{comp} \cdot \sum_{i \in \mathbf{I}^{\mathbf{STO}}} PWR_i \tag{A1-33}$$

Separation cost
$$C^{sep} \geq \lambda^{sep} \cdot \sum_{j' \in \mathbf{J}_{\mathbf{i}}^{\mathbf{in}}} F_{j'}^{T} \qquad i = V1, nV1 \tag{A1-34}$$

Heat exchanger cost
$$C^{hx} = \lambda^{hx} \sum_{i=\mathrm{E3,E6}} \frac{Q_i}{\Delta T_i \cdot \mathrm{h}^{\mathrm{avg}}} \tag{A1-35}$$

Reactor cost (R2)
$$C^{rxn} \geq \lambda^{rxn} F_j^{T} R T_i \tau^{rxn} / P \qquad i = R2, nR2;\ j \in \mathbf{J}_{\mathbf{i}}^{\mathbf{OUT}} \tag{A1-36}$$

Storage tank cost
$$C^{tk} = \textstyle\sum_{i \in \mathbf{I}^{\mathbf{STO}}} \lambda_i^{tk} \cdot \left(P_i^{H}/200\right)^{0.44} \cdot V_i^{tank} \text{, aboveground storage}$$
$$C^{tk} = \textstyle\sum_{i \in \mathbf{I}^{\mathbf{STO}}} \lambda_i^{under} \cdot V_i^{tank} \text{, underground storage} \tag{A1-37}$$

Storage media cost
$$C^{sm} = t^{sto} \cdot \sum_{k} F_{17,k} \cdot \lambda_k^{sm} \cdot \omega_k \tag{A1-38}$$

Storage system cost
$$C^{sto} = C^{sm} + C^{tk} + C^{rxn} + C^{hx} + C^{comp} + C^{sep} \tag{A1-39}$$

Capital cost
$$CAPEX = C^{sto} + \lambda^{sf} \cdot AREA + \lambda^{r} \cdot Q_{R1}/\mathrm{\eta}^{\mathrm{r}} + \lambda^{p} \cdot P^{rate}/\mathrm{\eta}^{\mathrm{para}} \tag{A1-40}$$

Cooling utility cost
$$C^{cu} = \lambda^{cu}\left[(Q_{E2} + Q_{E5}) \cdot t^{day} + Q_{nE5} \cdot t^{sto}\right]/24 \tag{A1-41}$$

Operation cost
$$OPEX = C^{cu} + P^{rate} \cdot \lambda^{om} \tag{A1-42}$$

Daily net electricity
$$W^{ele} = P^{rate} \cdot (t^{day} + t^{sto}) - W^{comp} \tag{A1-43}$$

LCOE calculation
$$LCOE = (CAPEX \cdot CFR + OPEX)/(365 \cdot W^{ele}) \tag{A1-44}$$

A1.2 Separation surrogate model

In the ammonia TCES system, a flash tank is used to separate unreacted ammonia from hydrogen and nitrogen (see **Figure 2-4**A). To model the flash tank, we derive the relation of ammonia liquid phase recovery (ζ_{NH_3}) by fitting the simulation data from ASPEN Plus.

Through ASPEN Plus simulation, 66 sample points are generated by varying the feed stream ammonia molar fraction ($\mathrm{x_{NH_3}}$) and flash tank temperature ($\mathrm{T_{flash}}$) between 0.1-0.6 and 10-60℃ respectively. Using the sample points, the function $\zeta_{NH_3} = f(\mathrm{x_{NH_3}}, \mathrm{T_{flash}})$ is fitted through polynomial regression in Matlab. Before fitting, variables are scaled and centered using standard normalization ($x^* = (x - \overline{x})/\sigma$). Different polynomial order combinations are tried to decide a relatively simple and accurate fitting. **Figure A1-2** shows the sample points and the fitting surface using the fitting function described as eqn (A1-45).

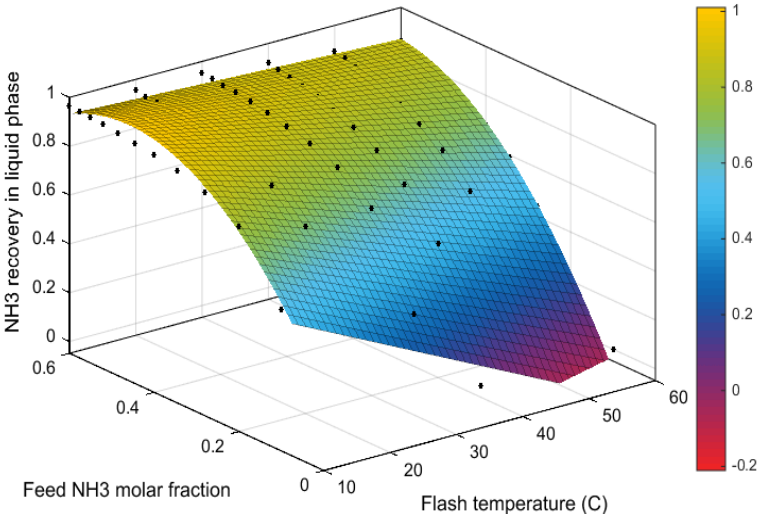

Figure A1-2. Sample points and fitting surface of ζ_{NH_3}

$$\zeta_{NH_3} = 0.84 - 0.095\, T^* + 0.15\, x^* + 0.06\, T^* x^* - 0.09\, {x^*}^2 \tag{A1-45}$$

A1.3 Optimization results: Case 1

Table A1-2. Stream temperature (T) and component molar flow rate (F)

Stream #	1	2	3	4	5	6	7	8	9	10	11	12
T(°C)	251	386	27	17	17	17	349	539	80	17	17	17
$F_{\mathrm{NH_3}}$(mol/s)	34445	21956	21956	21956	1777	836	836	3034	3034	3034	23214	11231
$F_{\mathrm{H_2}}$(mol/s)	392	19124	19124	19124	29319	13789	13789	10491	10491	10491	296	96
$F_{\mathrm{N_2}}$(mol/s)	196	6440	6440	6440	9894	4653	4653	3554	3554	3554	100	96

Stream #	13	14	15	16	17	18	19	20	21	22	23	24
T(°C)	17	17	17	17	17	17	399	80	17	17	17	17
$F_{\mathrm{NH_3}}$(mol/s)	11231	34445	941	941	672	672	8636	8636	8636	614	8022	8022
$F_{\mathrm{H_2}}$(mol/s)	96	392	15530	15530	11093	11093	6844	6844	6844	6775	68	68
$F_{\mathrm{N_2}}$(mol/s)	96	196	5241	5241	3743	3743	6844	6844	6844	6775	68	68

Table A1-3. Unit temperature, pressure, heat duty and work load (day and night mode)

Unit	R1	R2	TK1	TK2	V1	C1	C2	S1	M1
Temperature (°C)	386	539	17	17	1	17	1	17	17
Pressure (bar)	300	300	115-564	188-393	300	300-564	188-300	300	300
Heat duty (MW)	1005	0	0	0	0	0	0	0	0
Work (MWh/day)	0	0	0	0	0	192	32	0	0

Unit	E1	E2	E3	E4	E5	E6
Temperature (°C)	386-27	27-17	17-349	539-80	80-17	17-251
Pressure (bar)	300	300	300	300	300	300
Heat duty (MW)	-968	-25	216	-310	-43	753
Work (MWh/day）	0	0	0	0	0	0

Unit	nR2	nV1	nC1	nC2	nE4	nE5
Temperature (°C)	399	17	17	17	399-80	80-17
Pressure (bar)	300	300	115-300	300-393	300	300
Heat duty (MW)	0	0	0	0	-370	-72
Work (MWh/day）	0	0	140	34	0	0

A1.4 Geological map for underground storage

There are three types of underground storage facilities: depleted gas reservoirs, aquifers, and mined salt caverns. [93] **Figure A1-3** and **Figure A1-4** shows the potential geologic underground storage areas in the United States and around the word.

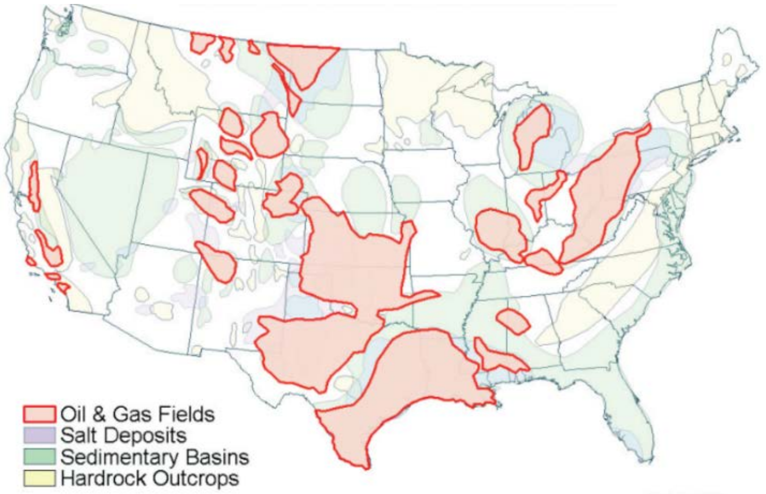

Figure A1-3. Potential geologic underground storage areas in the United States [200]

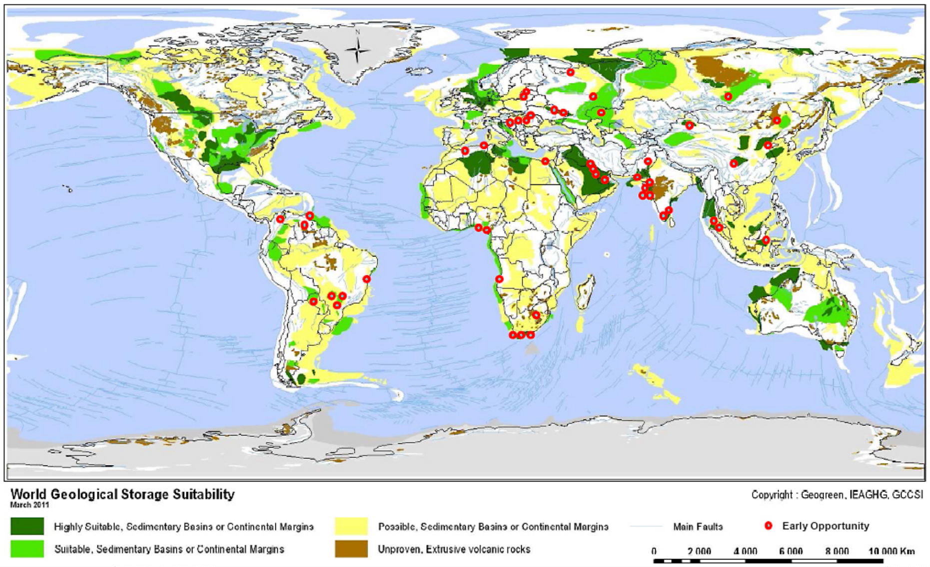

Figure A1-4. Safe locations for underground carbon dioxide storage [201]

A1.5 Temperature dependent heat capacity

Figure A1-5 shows how the heat capacities of NH_3, H_2 and N_2 change with temperature at 300 bar. We note that ammonia has a significant higher heat capacity between 80-300 ℃ due to the continuous phase change. To account for the latent heat, we divide the temperature into 3 stages: cold (10-80 ℃), warm (80-300 ℃) and hot (>300 ℃). For each component k, different average heat capacities are used for each temperature stage (denoted by Cp_k^{cold}, Cp_k^{warm} *and* Cp_k^{hot}).

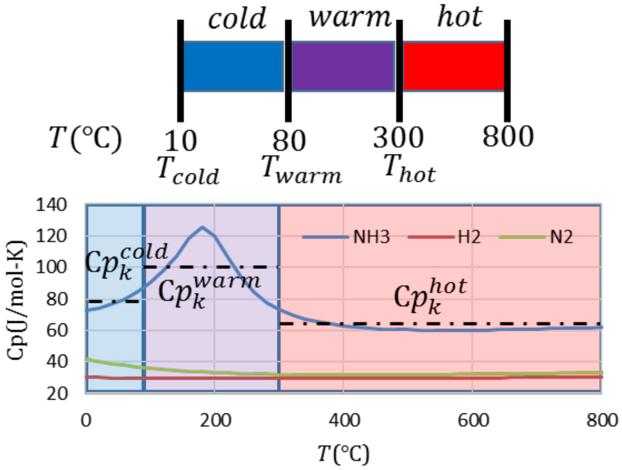

Figure A1-5. Heat capacities of NH_3, H_2 and N_2 at 300 bar

We then classify each process stream *j* into either cold stream ($\mathbf{J}^{cold}$), warm stream ($\mathbf{J}^{warm}$) or hot stream ($\mathbf{J}^{hot}$) based on the stream temperature range (see **Figure A1-6**). For a general unit *i*, the temperature stage of its inlet and outlet streams are known from the stream classification. Accordingly, the unit heat duty calculation equation is derived. **Figure A1-7** illustrates the heat duty calculation for a unit with cold inlet stream and hot outlet stream.

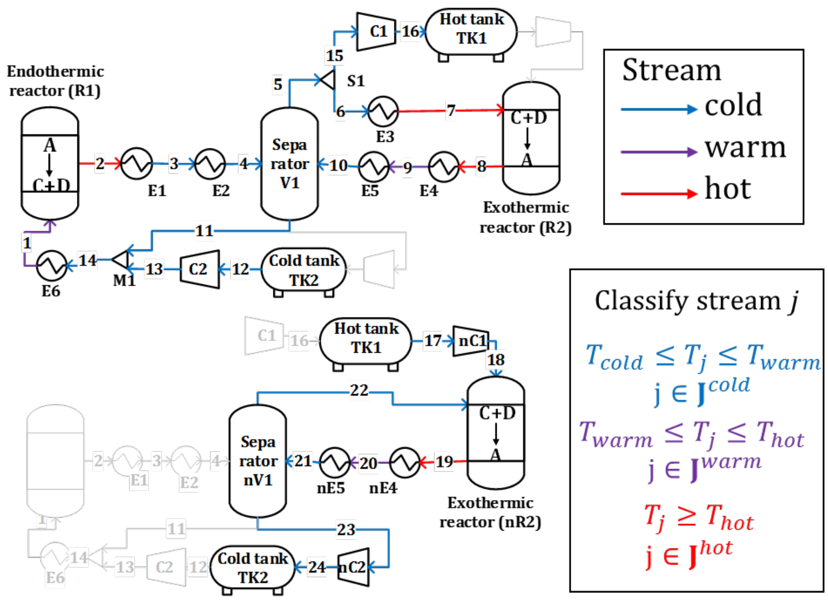

Figure A1-6. Classify process streams into cold, warm and hot stream.

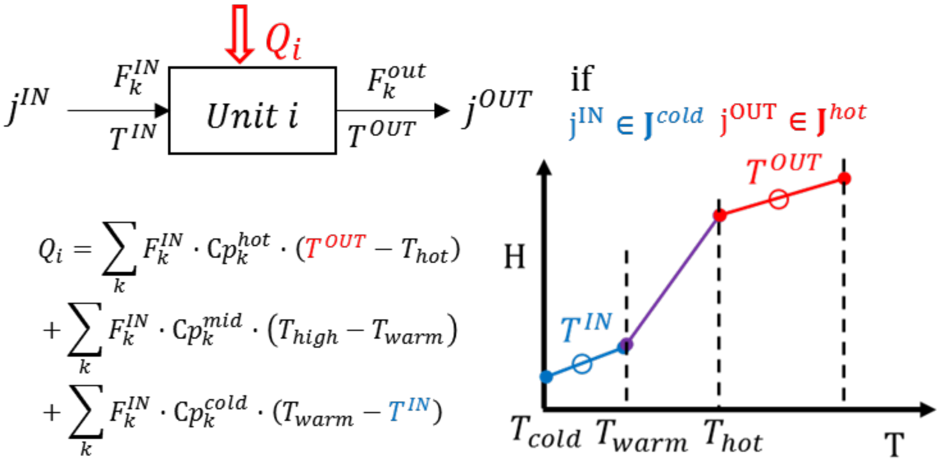

$$Q_i = \sum_k F_k^{IN} \cdot Cp_k^{hot} \cdot (T^{OUT} - T_{hot}) + \sum_k F_k^{IN} \cdot Cp_k^{mid} \cdot (T_{high} - T_{warm}) + \sum_k F_k^{IN} \cdot Cp_k^{cold} \cdot (T_{warm} - T^{IN})$$

Figure A1-7. An example of unit heat duty calculation.

A1.6 Compressibility factor

In our TCES systems, gas products are compressed and stored at high pressure (150-550 bar). To account for the real gas behavior, we introduce compressibility factors for the calculation of compression work and storage tank volumes. **Figure A1-8** shows the compressibility factors of all gas products at 100 °C (obtained from ASPEN PLUS property database using Schwartzentruber-

Renon equation-of-state). Based on these data, we can calculate the stream average compressibility factor as a function of stream pressure and composition.

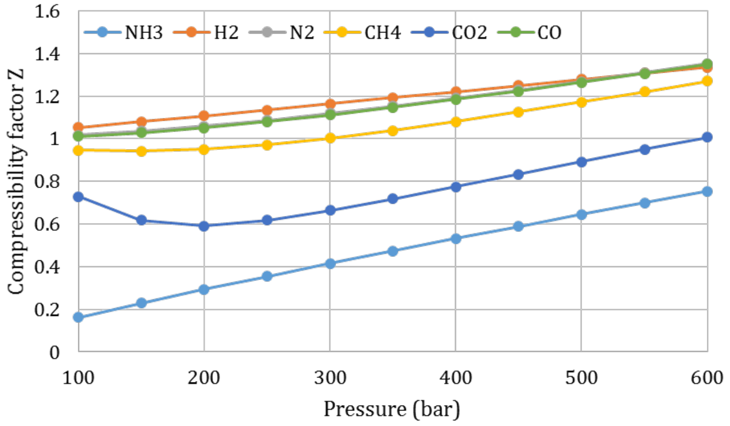

Figure A1-8. Compressibility factor of different components at 100 ℃

A2 Explanations to Chapter 3

A2.1 Optimization results: stochastic model

Table A2-1. Stream total molar flow rate $F_{j,s}^{T}$ (mol/s)

Scenario	1	2	3	4	5	6	7	8	9	10
1	3508	4368	1686	1347	1347	3508	2682	2682	2682	2682
2	11532	13507	3864	3266	3266	11532	9643	9643	9643	9643
3	13252	16002	3607	2955	2955	13252	12395	12395	12395	12395
4	13043	16490	3317	2600	2600	13043	13174	13174	13174	13174
5	11773	15374	3173	2424	2424	11773	12201	12201	12201	12201
6	6912	9958	2761	1917	1917	6912	7197	7197	7197	7197

Scenario	11	12	13	14	15	16	17	18	19	20
1	2160	2160	520	520	520	464	419	419	419	419
2	8266	8266	2667	2667	2667	2452	2286	2286	2286	2286
3	10297	10297	4900	4900	4900	4456	4071	4071	4071	4071
4	10444	10444	6343	6343	6343	5668	5028	5028	5028	5028
5	9349	9349	8134	8134	8134	7058	6233	6233	6233	6233
6	4996	4996	6193	6193	6193	5177	4299	4299	4299	4299

Table A2-2. Stream composition: mole fraction of methane $x_{CH_4,j,s}$

Scenario	1	2	3	4	5	6	7	8	9	10
1	0.494	0.299	0.299	0.499	0.499	0.494	0.299	0.299	0.299	0.299
2	0.489	0.345	0.345	0.499	0.499	0.489	0.345	0.345	0.345	0.345
3	0.489	0.319	0.319	0.499	0.499	0.489	0.319	0.319	0.319	0.319
4	0.49	0.283	0.283	0.499	0.499	0.49	0.283	0.283	0.283	0.283
5	0.497	0.263	0.263	0.499	0.499	0.497	0.263	0.263	0.263	0.263
6	0.499	0.194	0.194	0.499	0.499	0.499	0.194	0.194	0.194	0.194
Scenario	11	12	13	14	15	16	17	18	19	20
1	0.491	0.491	0.299	0.299	0.299	0.395	0.491	0.491	0.491	0.491
2	0.485	0.485	0.345	0.345	0.345	0.419	0.485	0.485	0.485	0.485
3	0.486	0.486	0.319	0.319	0.319	0.4	0.486	0.486	0.486	0.486
4	0.488	0.488	0.283	0.283	0.283	0.377	0.488	0.488	0.488	0.488
5	0.496	0.496	0.263	0.263	0.263	0.38	0.496	0.496	0.496	0.496
6	0.499	0.499	0.194	0.194	0.194	0.33	0.499	0.499	0.499	0.499

Table A2-3. Stream temperature $T_{j,s}$(℃)

Scenario	11	12	13	14	15	16	17	18	19	20
1	50	50	40	40	483	760	495	495	50	50
2	50	50	40	40	527	722	538	538	50	50
3	50	50	40	40	525	752	537	537	50	50
4	50	50	40	40	508	786	520	520	50	50
5	50	50	40	40	428	782	440	440	50	50
6	50	50	40	40	326	808	338	338	50	50
Scenario	1	2	3	4	5	6	7	8	9	10
1	556	881	881	338	50	50	881	60	40	40
2	599	827	827	338	50	50	827	60	40	40
3	670	858	858	338	50	50	858	60	40	40
4	722	898	898	338	50	50	898	60	40	40
5	736	920	920	338	50	50	920	60	40	40
6	734	1000	1000	338	50	50	1000	60	40	40

A2.2 Simplified CSP process model

This section provides the simplified CSP plant model used to study the accuracy of the proposed multimode stochastic programming approach in **Section 3.3**.

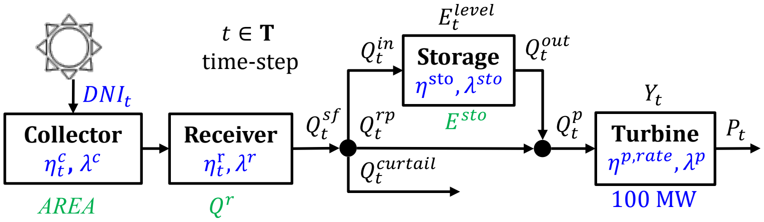

Figure A2-1. The simplified CSP process with main optimization variables (design: green, operation: black) and parameters (blue).

Set

$t \in \mathbf{T}$	Set of 8760 hourly time steps in the time horizon of a year

Parameters

CRF	Capital recovery factor
DNI_t	Solar direct normal irradiance (W/m^2)
$E^{sto,ref}$	Reference thermal energy storage capacity (kWh$_\mathrm{t}$)
$f^{indirect}$	Indirect cost factor
f^{cont}	Contingency cost factor
P^{rate}	CSP plant rated capacity (kW$_\mathrm{e}$)
P^{lo}	Minimum turbine operation level (kW$_\mathrm{e}$)
P^{up}	Maximum turbine operation level (kW$_\mathrm{e}$)
$Q^{r,ref}$	Reference size of receiver (kW$_\mathrm{t}$)
γ^r	Scaling factor of receiver
γ^{sto}	Scaling factor of storage system
η_t^c	Collector efficiency
η_t^r	Receiver efficiency
η^{sto}	Storage efficiency
$\eta^{p,rate}$	Turbine efficiency at rated power output level 100 MW
η^{para}	Plant parasitic efficiency
λ^c	Collector price (\$/m^2 mirror aperture)
λ^{ele}	Electricity power purchase agreement price (₵/kWh$_\mathrm{e}$)
λ^r	Receiver price at size $Q^{r,ref}$ (\$/kW$_\mathrm{t}$)
λ^{sto}	Two-tank storage system price at size $Q^{sto,ref}$ (\$/kWh$_\mathrm{t}$)
λ^p	Power block (turbine) price (\$/kW)
$\lambda^{startup}$	Cost for turbine start-up (\$/start_up)

$\lambda^{om,fix}$	Operation and maintenance, fix cost (\$/kW-year)
$\lambda^{om,vary}$	Operation and maintenance, varying cost (\$/kWh$_e$ electricity generated)

Nonnegative Continuous Variables

$AREA$	Solar field area (m^2)
$CAPEX$	Plant total capital cost (\$)
C^r	Receiver cost (\$)
C^{sto}	Storage system cost (\$)
$LCOE$	Levelized cost of electricity (ℂ/kWh$_e$)
$OPEX$	Operational cost (\$/year)
PFT	Net annual profit (\$/year)
P_t	Turbine output level (kW$_e$)
Q^r	Receiver size (kW$_t$)
Q_t^{sf}	Thermal power received by receiver (kW$_t$)
Q_t^{rp}	Thermal power directly delivered from receiver to the turbine (kW$_t$)
$Q_t^{curtail}$	Heat curtailed from receiver (kW$_t$)
Q_t^{in}	Thermal energy charging into storage system (kW$_t$)
Q_t^{out}	Thermal energy discharging out of storage system (kW$_t$)
Q_t^{p}	Thermal power delivered to the turbine (kW$_t$)
E^{sto}	Thermal energy storage capacity (kWh$_t$)
E_t^{level}	Storage level at time *t* (kWh$_t$)

Binary variables

Y_t	1 if the turbine is on at time *t*
$Y_t^{startup}$	1 if the turbine starts up at time *t*
Z_t^{in}	1 if energy is charging into storage system at time *t*
Z_t^{out}	1 if energy is discharging out of storage system at time *t*

Model Equations

Energy received

$$Q_t^{sf} = AREA \cdot DNI_t \cdot \eta_t^c \cdot \eta_t^r \quad t \in \mathbf{T} \tag{A2-1}$$

Receiver energy

$$Q_t^{sf} = Q_t^{in} + Q_t^{rp} + Q_t^{curtail} \quad t \in \mathbf{T} \tag{A2-2}$$

Storage level
$$E_t^{level} = E_{t-1}^{level} + Q_t^{in} - Q_t^{out} \quad t \in \mathbf{T} \tag{A2-3}$$

Storage capacity
$$E_t^{level} \leq E^{sto} \quad t \in \mathbf{T} \tag{A2-4}$$

Storage charging
$$Q_t^{in} \leq M \cdot Z_t^{in} \quad t \in \mathbf{T} \tag{A2-5}$$

Storage discharging
$$Q_t^{out} \leq M \cdot Z_t^{out} \quad t \in \mathbf{T} \tag{A2-6}$$

Charge/discharge
$$Z_t^{in} + Z_t^{out} \leq 1 \quad t \in \mathbf{T} \tag{A2-7}$$

Heat to turbine
$$Q_t^{p} = Q_t^{rp} + Q_t^{out} \cdot \eta^{sto} \quad t \in \mathbf{T} \tag{A2-8}$$

Turbine output level
$$Q_t^{p} \cdot \eta^{p,rate} \cdot \eta^{para} = \frac{18}{19} \cdot P_t + \frac{1}{19} P^{rate} \cdot Y_t \quad t \in \mathbf{T} \tag{A2-9}$$

Operation range
$$Y_t \cdot P^{lo} \leq P_t \leq Y_t \cdot P^{up} \quad t \in \mathbf{T} \tag{A2-10}$$

Turbine start-up
$$Y_t - Y_{t-1} \leq Y_t^{startup} \quad t \in \mathbf{T} \tag{A2-11}$$

Receiver cost*
$$C^{r} = \lambda^{r} \cdot Q^{r,ref} \cdot \left(\frac{Q^{r}}{Q^{r,ref}}\right)^{\gamma^{r}} \tag{A2-12}$$

Storage cost*
$$C^{sto} = \lambda^{sto} \cdot E^{sto,ref} \cdot \left(\frac{E^{sto}}{E^{sto,ref}}\right)^{\gamma^{sto}} \tag{A2-13}$$

Capital cost
$$CAPEX = \left(\lambda^{c} \cdot AREA + C^{r} + C^{sto} + \frac{\lambda^{p} \cdot P^{rate}}{\eta^{para}}\right) \cdot (1 + f^{indirect}) \cdot (1 + f^{cont}) \tag{A2-14}$$

Operation cost
$$OPEX = \lambda^{om,fix} \cdot P^{rate} + \lambda^{om,vary} \cdot \sum_{t} P_t + \lambda^{startup} \cdot \sum_{t} Y_t^{startup} \tag{A2-15}$$

Objective PFT
$$PFT = \lambda^{ele} \cdot \sum_{t} P_t - CAPEX \cdot CRF - OPEX \tag{A2-16}$$

* Receiver and storage costs are formulated using piecewise linear function in GAMS.

A3 Explanations to Chapter 4

A3.1 Numerical simulations of fixed-bed reactors

Initial and boundary conditions

The initial and boundary conditions for reactor simulations (see **Section 4.3.1**) during multi-cycle operation are provided in **Table A3-1**.

Table A3-1. Initial and boundary conditions of fixed-bed reactor simulations.

Cycle	Starting time Inlet Outlet	Energy balance for the fluids eqn (4-3)	Energy balance for the reactor bed eqn (4-4)	Rate of conversion in the reactor bed eqn (4-7)
1^{st} cycle charging	$t = 0$	$T_f = T_{WF}^{in}(z, t = 0)$	$T_{bed} = T_{WF}^{in}(z, t = 0)$	$X_{bed} = 0.001$
	$z = 0$	$T_f = T_{HTF}^{in}$	$T_{bed} = T_{HTF}^{in}$	
	$z = L_{bed}$	$\frac{\partial T_f}{\partial z} = 0$	$\frac{\partial T_{bed}}{\partial z} = 0$	
1^{st} cycle discharging	$t = t^c$	$T_f = T_f(z, t = t^c)$	$T_{bed} = T_{bed}(z, t = t^c)$	$X_{bed} = X_{bed}(z, t = t^c)$
	$z = L_{bed}$	$T_f = T_{WF}^{in}$	$\frac{\partial T_{bed}}{\partial z} = 0$	
	$z = 0$	$\frac{\partial T_f}{\partial z} = 0$	$\frac{\partial T_{bed}}{\partial z} = 0$	
k^{th} cycle charging (k $>$ 1)	$t = (k-1)t^c + (k-1)t^d$	$T_f = T_f(z, t = (k-1)t^c + (k-1)t^d)$	$T_{bed} = T_{bed}(z, t = (k-1)t^c + (k-1)t^d)$	$X_{bed} = X_{bed}(z, t = (k-1)t^c + (k-1)t^d)$
	$z = 0$	$T_f = T_{HTF}^{in}$	$\frac{\partial T_{bed}}{\partial z} = 0$	
	$z = L_{bed}$	$\frac{\partial T_f}{\partial z} = 0$	$\frac{\partial T_{bed}}{\partial z} = 0$	
k^{th} cycle discharging (k $>$ 1)	$t = kt^c + (k-1)t^d$	$T_f = T_f(z, t = kt^c + (k-1)t^d)$	$T_{bed} = T_{bed}(z, t = kt^c + (k-1)t^d)$	$X_{bed} = X_{bed}(z, t = kt^c + (k-1)t^d)$
	$z = L_{bed}$	$T_f = T_{WF}^{in}$	$\frac{\partial T_{bed}}{\partial z} = 0$	
	$z = 0$	$\frac{\partial T_f}{\partial z} = 0$	$\frac{\partial T_{bed}}{\partial z} = 0$	

Kinetic models

Table A3-2 shows the kinetic models used in reactor simulations.

For $6\mathrm{Mn_2O_3} \leftrightarrow 4\mathrm{Mn_3O_4} + \mathrm{O_2}$ and $\mathrm{CaCO_3} \leftrightarrow \mathrm{CaO} + \mathrm{CO_2}$ reactions, the kinetic model is in the form of

$$\frac{dX_{bed}}{dt} = k_0 \exp\left(-\frac{E_a}{R_{const}T_{bed}}\right) X_{bed}{}^{a}(1 - X_{bed})^{b} \left|1 - \frac{p_C}{p_C^{eq}}\right|^{s} \quad \text{(A3-1)}$$

For $\mathrm{Ca(OH)_2} \leftrightarrow \mathrm{CaO} + \mathrm{H_2O}$ reaction, the kinetic model is in the form of

$$\frac{dX_{bed}}{dt} = k_0 X_{bed}{}^{a}(1 - X_{bed})^{b} \left|1 - \frac{T_{bed}}{T_{bed}^{eq}}\right|^{s} \quad \text{(A3-2)}$$

Table A3-2. Kinetic models used in reactor numerical simulations.

Reaction	Charging Discharging	k_0 (s^{-1})	E_a (J/mol)	a	b	s	Reference
$\mathrm{Mn_2O_3}$	Reduction	8.2167×10^{9}	2.504×10^{5}	0.45633	1.4584	20	177
	Oxidation	-2.8089×10^{12}	2.997×10^{5}	1.0245	0.64231	1.3676	
$\mathrm{Ca(OH)_2}$	Dehydration	0.05		0	1	1	190
	Hydration	-0.2		1	0	1	
$\mathrm{CaCO_3}$	Calcination	1.12×10^{6}	1.50×10^{5}	0	1.5	1.86	191
	Carbonation	-5.53×10^{5}	1.59×10^{5}	1.5	0	1	192

Nondimensionalization

The dimensionless input variable κ is obtained from nondimensionalizing the governing equations of the reactor numerical model. Here we provide the procedure of nondimensionalization.

Firstly, the dimensionless time, coordinate, bed temperature and fluid temperature are defined as

$$t^* = \frac{t}{t^c} \quad \text{(A3-3)}$$

$$z^* = \frac{z}{L_{bed}} \quad \text{(A3-4)}$$

$$T_f^* = \frac{T_f - T_{WF}^{in}(t=0)}{T_{HTF}^{in} - T_{WF}^{in}(t=0)} \quad \text{(A3-5)}$$

$$T_{bed}^{*} = \frac{T_{bed} - T_{WF}^{in}(t=0)}{T_{HTF}^{in} - T_{WF}^{in}(t=0)} \tag{A3-6}$$

where $T_{WF}^{in}(t = 0)$ is the WF inlet temperature at the beginning of discharging, and T_{HTF}^{in} is the HTF inlet temperature.

The governing equation eqn (4-3) is then expressed in terms of dimensionless variables,

$$\frac{\partial T_f^*}{\partial t^*} + \frac{u_f t^c}{L_{bed}} \frac{\partial T_f^*}{\partial z^*} - \frac{t^c k_f}{\rho_f C_{p_f} {L_{bed}}^2} \frac{\partial^2 T_f^*}{\partial {z^*}^2} = \frac{4 t^c U}{d \rho_f C_{p_f}} \left(T_{bed}^* - T_f^*\right) \tag{A3-7}$$

From the coefficient of the second term on the left-hand side and the coefficient of the term on the right-hand side, we can derive κ that measures the ratio of heat transfer rate across tube wall to the heat advection rate along the tube:

$$\kappa = \frac{4U/d}{u_f \rho_f C p_f / L_{bed}} \tag{A3-8}$$

κ^c and κ^d are defined for charging (f =HTF) and discharging (f =WF) accordingly.

A3.2 Selection of HTF and WF inlet temperature

For each reaction, we run simulations with different T_{HTF}^{in} and T_{WF}^{in} and determine the appropriate fluid inlet temperature based on the corresponding reactor performance.

Mn_2O_3 TCES

In **Figure A3-1**, we compare the simulation results of Mn_2O_3 TCES reactor with $T_{HTF}^{in} = 1173$, 1273, 1373 K, $L_{bed} = 1.6$ m and $t^c = t^d = 6$ h. Both overall bed conversion (χ) and power generation effectiveness (γ) reach maximum when T_{HTF}^{in} is 1273 K, therefore we use this temperature as T_{HTF}^{in} for Mn_2O_3 TCES reactor in this study.

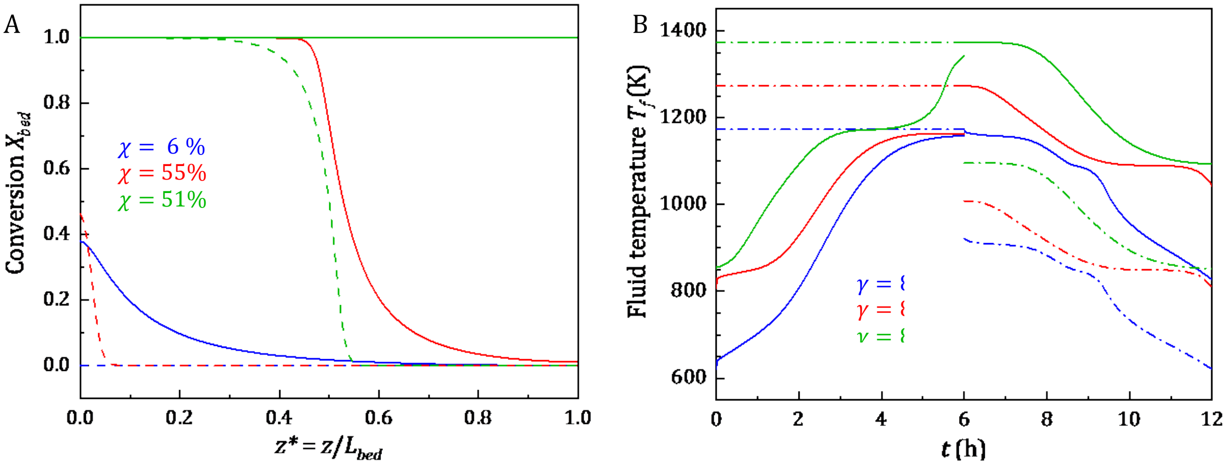

Figure A3-1. (A) Bed conversion and (B) fluid temperature of fixed-bed reactors with different HTF and WF inlet temperatures (blue: T_{HTF}^{in} = 1173 K, red: T_{HTF}^{in} = 1273 K, green: T_{HTF}^{in} = 1373 K) in Mn_2O_3 TCES. In A, conversions at the start of charging (t=0) are shown as dashed lines and at the end of charging (t=6 h) as solid lines. In B, fluid temperatures at the inlet are shown as dash-dotted lines and at the outlet as solid lines.

Ca(OH)₂ TCES

In **Figure A3-2**, we compare the simulation results of $Ca(OH)_2$ TCES reactor with $T_{HTF}^{in} = 873$, 923, 1023 K, $L_{bed} = 1.1$ m and $t^c = t^d = 6$ h. As T_{HTF}^{in} increases, χ increases monotonically but the power generation effectiveness γ increases to 77% at $T_{HTF}^{in} = 923$ K and starts to decrease. Considering the limited improvement of χ brought by the 100 K temperature increase, we choose 923 K as T_{HTF}^{in} for $Ca(OH)_2$ TCES reactor in this study.

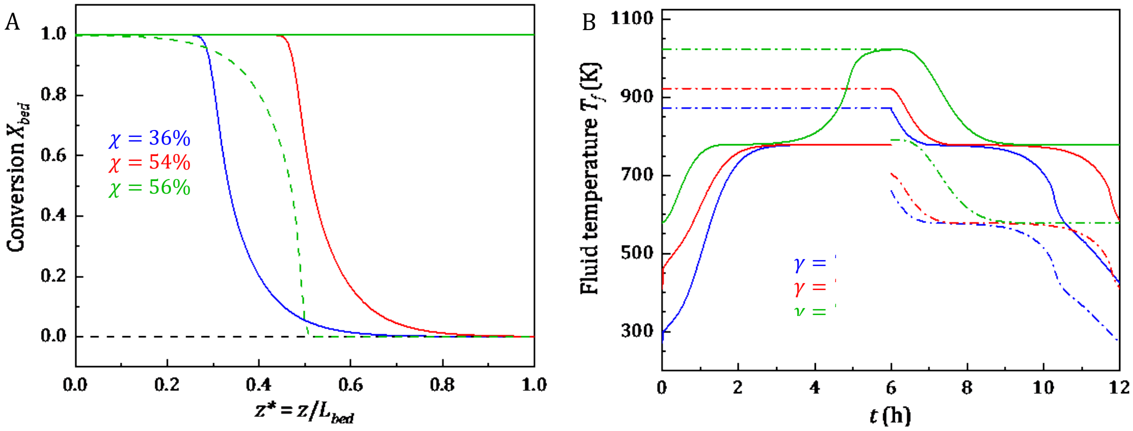

Figure A3-2. (A) Bed conversion and (B) fluid temperature of fixed-bed reactors with different HTF and WF inlet temperatures (blue: T_{HTF}^{in} = 873 K, red: T_{HTF}^{in} = 923 K, green: T_{HTF}^{in} = 1023 K) in $Ca(OH)_2$

TCES. In A, conversions at the start of charging (t=0) are shown as dashed lines and at the end of charging (t=6 h) as solid lines. In B, fluid temperatures at the inlet are shown as dash-dotted lines and at the outlet as solid lines. Note that the black dashed line in A denotes an overlap of lines in blue and red.

$CaCO_3$ TCES

In **Figure A3-3**, we compare the simulation results of $CaCO_3$ TCES reactor with $T_{HTF}^{in} = 1273$, 1323, 1373 K, $L_{bed} = 0.5$ m and $t^c = t^d = 6$ h. As T_{HTF}^{in} increases, both χ and power generation effectiveness γ increase. Increasing T_{HTF}^{in} above 1373 K may further improve χ and γ, but it would lower the receiver efficiency. As a result, we select $T_{HTF}^{in} = 1373$ K for $CaCO_3$ TCES reactor in this study.

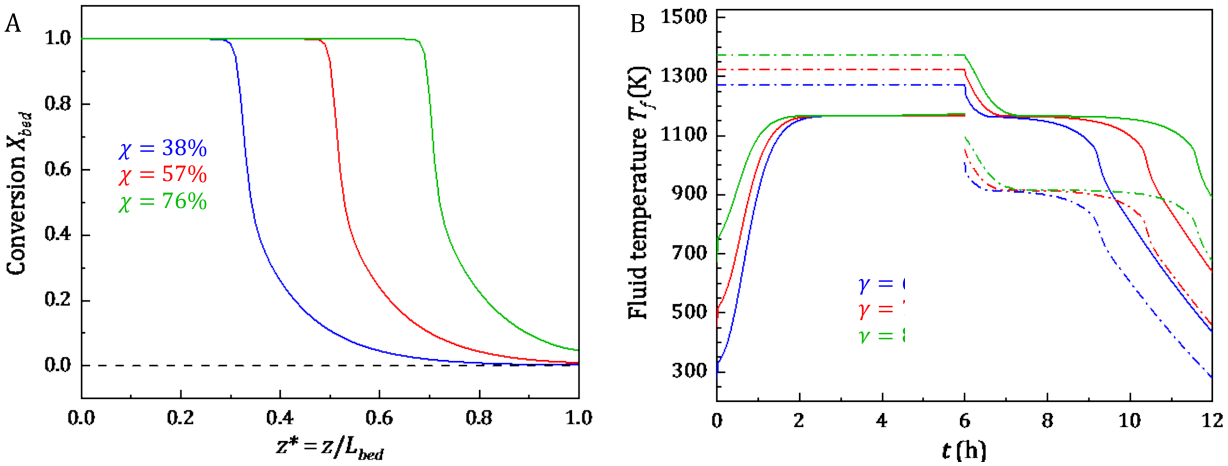

Figure A3-3. (A) Bed conversion and (B) fluid temperature of fixed-bed reactors with different HTF and WF inlet temperatures (blue: $T_{HTF}^{in} = 1273$ K, red: $T_{HTF}^{in} = 1323$ K, green: $T_{HTF}^{in} = 1373$ K) in $CaCO_3$ TCES. In A, conversions at the start of charging (t=0) are shown as dashed lines and at the end of charging (t=6 h) as solid lines. In B, fluid temperatures at the inlet are shown as dash-dotted lines and at the outlet as solid lines. Note that the black dashed line in A denotes an overlap of lines in blue, red, and green.

A3.3 Selection of tube diameter

To determine the optimal tube diameter (d), we run simulations of Mn_2O_3 TCES reactor at $\theta = 1$ with $d = 1$ mm, 2 mm, 4 mm, and 1 cm. The reactor performance of the four cases are compared in **Figure A3-4**. As d increases, both χ and γ decrease. Increasing d to 1 cm is notably detrimental to the reactor performance while reducing d from 2 mm to 1 mm brings marginal improvement. Hence, tube diameter of 2 mm is selected in our design.

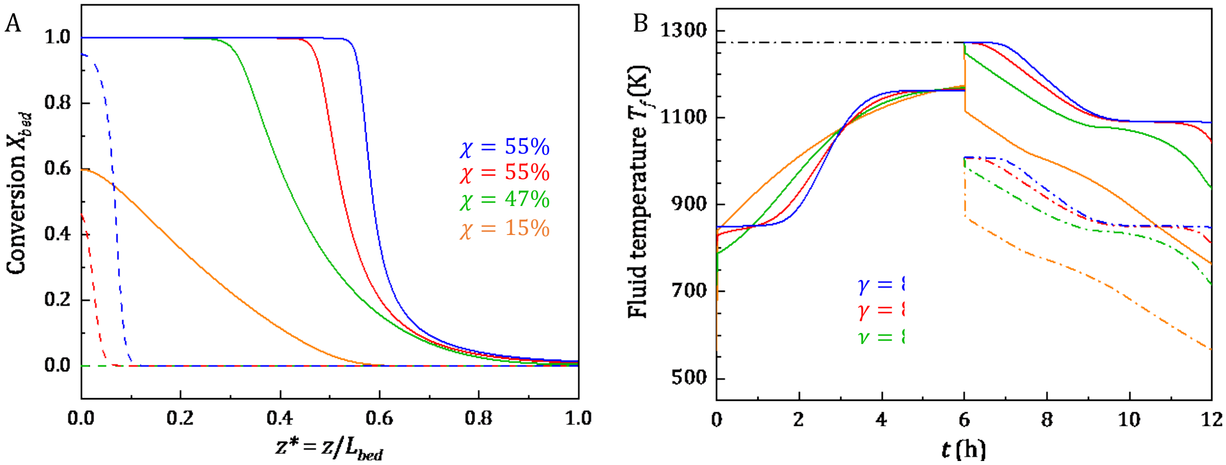

Figure A3-4. (A) Bed conversion and (B) fluid temperature of fixed-bed reactors with different tube diameters (blue: 0.001 m, red: 0.002 m, green: 0.004 m, orange: 0.010 m) in Mn_2O_3 TCES. In A, conversions at the start of charging (t=0) are shown as dashed lines and at the end of charging (t=6 h) as solid lines. In B, fluid temperatures at the inlet are shown as dash-dotted lines and at the outlet as solid lines. Note that the black dash-dotted line in B denotes an overlap of lines in blue, red, green and orange.

A4 Explanations to Chapter 5

A4.1 Reaction parameters

Table A4-1 lists reaction parameters used in this study, including the properties of s-CO_2 and reactants as well as the relations between equilibrium temperature T^{eq} and gas C pressure for each reaction.

Table A4-1. Reaction parameters used in this study.

HTF & WF: s-CO2 at 250 bar			
Heat capacity of fluid: Cp_{HTF} & Cp_{WF}	1.281 kJ/kg-K		
Thermal conductivity of fluid: k_{HTF} & k_{WF}	0.075 W/m-K		
Reactions & Reactants			
$\mathrm{A} \leftrightarrow \mathrm{B} + \mathrm{C}$	$6\mathrm{Mn_2O_3} \leftrightarrow 4\mathrm{Mn_3O_4} + \mathrm{O_2}$	$\mathrm{Ca(OH)_2} \leftrightarrow \mathrm{CaO} + \mathrm{H_2O}$	$\mathrm{CaCO_3} \leftrightarrow \mathrm{CaO} + \mathrm{CO_2}$
Molecular weight Mw_A, Mw_B, Mw_C (g/mol)	$158, 229, 32$	74, 56, 18	100, 56, 44
Solid density, ρ_A (kg/m^3)	4500	2200	2710
Solid density, ρ_B (kg/m^3)	4860	3340	3340
Gas density, ρ_C (kg/m^3)	0.35	0.28	0.48
Gas density at storage, ρ_C (kg/m^3)	/	997	764
Heat capacity, Cp_A (kJ/kg-K)	0.83	1.53	1.29
Heat capacity, Cp_B (kJ/kg-K)	0.82	0.95	0.95
Heat capacity, Cp_C (kJ/kg-K)	1.10	2.14	1.27
Reaction enthalpy ΔH^{rxn} (kJ/kg A)	202	1409	1779
Equilibrium pressure of gas C, p_C^{eq} (bar)	$\ln p_C^{eq} = -\frac{21650}{T^{eq}} + 18.231$	$\ln p_C^{eq} = -\frac{12845}{T^{eq}} + 16.508$	$\ln p_C^{eq} = -\frac{20474}{T^{eq}} + 17.538$
T^{eq}(K)@ 1bar	1094	778	1168
Cooling duty of C from T^{eq} to 298K (kJ/kg)	810	3395	971

A4.2 Continuous reactor model

The key units of a TCES system are two reactors: R1, where the heat from solar irradiation or heat transfer fluid (HTF) drives an endothermic reaction (v_AA (s) → v_BB (s) + v_CC (g)) and R2, where the reverse exothermic reaction takes place and heats up the power cycle working fluid (WF). **Figure A4-1** shows a simplified process flowsheet of TCES systems with continuous reactors.

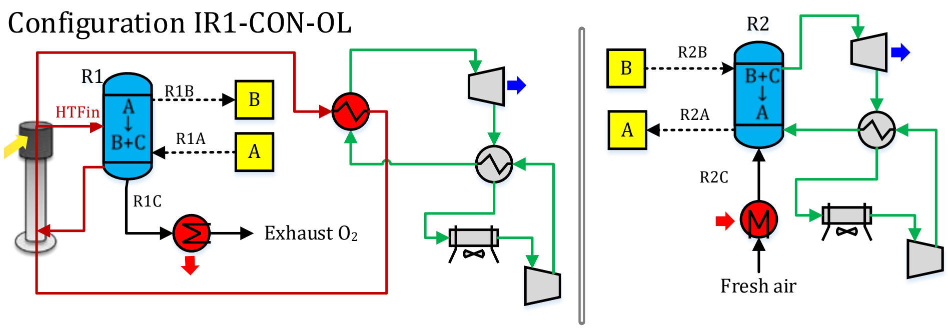

Figure A4-1. Process flowsheet of configuration IR1-CON-OL.

To model the continuous reactors, we first build the mass balances for reactors R1 and R2,

$$F_{R1B,s} = v_B/v_A \cdot F_{R1A,s} \quad s \in \mathbf{S} \tag{A4-1}$$

$$F_{R1C,s} = v_C/v_A \cdot F_{R1A,s} \quad s \in \mathbf{S} \tag{A4-2}$$

$$F_{R2B,s} = v_B/v_A \cdot F_{R2A,s} \quad s \in \mathbf{S} \tag{A4-3}$$

$$F_{R2C,s} = v_C/v_A \cdot F_{R2A,s} \quad s \in \mathbf{S} \tag{A4-4}$$

where $F_{j,s}$ is the molar flow rate of stream $j \in \mathbf{J}$ in scenario $s \in \mathbf{S}$, v_k is the stoichiometry of reactant $k \in \mathbf{K}$.

The heat duties of R1 and R2 $(Q_{R1,s}, Q_{R2,s})$ are equal to the enthalpy difference between its outlet and inlet stream, resulting from both component and temperature changes,

$$Q_{R1,s} = \Delta H^{rxn} \cdot Mw_A \cdot F_{R1A,s} + (T_{R1} - T_{R2}) \cdot Cp_A \cdot Mw_A \cdot F_{R1A,s} \quad s \in \mathbf{S} \tag{A4-5}$$

$$Q_{R2,s} = \Delta H^{rxn} \cdot Mw_A \cdot F_{R2A,s} + (T_{R1} - T_{R2}) \cdot Cp_B \cdot Mw_B \cdot F_{R2B,s} \quad s \in \mathbf{S} \tag{A4-6}$$

where ΔH^{rxn} is the reaction enthalpy, Cp_A is the heat capacity of A, and Mw_k is the molecular weight of reactant k (see **Table A4-1** for their values). T_{R1} and T_{R2} are the endothermic and exothermic reaction temperatures, which follow $T_{R1} > T^{eq} > T_{R2}$.

The endothermic and exothermic reaction rate, R_{R1} and R_{R2}, can be calculated based on the kinetics models given in **Table A3-2**,

$$R_{R1} = k_0\, exp\left(-\frac{E_a}{R_{const}T_{R1}}\right) 0.5^a(1-0.5)^b \left|1 - \frac{1}{p_{C,R1}^{eq}}\right|^s \tag{A4-7}$$

$$R_{R2} = k_0\, exp\left(-\frac{E_a}{R_{const}T_{R2}}\right) 0.5^a(1-0.5)^b \left|1 - \frac{1}{p_{C,R2}^{eq}}\right|^s \tag{A4-8}$$

where $p_{C,R1}^{eq}/p_{C,R2}^{eq}$ is the equilibrium pressure of gas C at T_{R1}/T_{R2} (see **Table A4-1**).

The reactor sizing equations ensure the reactor volume ($V^{reactor}$) is greater than the sizing requirement of R1 and R2 in any scenario. For process configurations with indirect R1, endothermic and exothermic reactions can take place alternately during the day and night in the same reactor (i.e., R1 and R2 share the same equipment).

$$V^{reactor} \geq Mw_A \cdot F_{R1A,s}/\rho_A\,/(1-\varepsilon_{bed})/R_{R1} \quad s \in \mathbf{S} \tag{A4-9}$$

$$V^{reactor} \geq Mw_B \cdot F_{R2B,s}/\rho_B\,/(1-\varepsilon_{bed})/R_{R2} \quad s \in \mathbf{S} \tag{A4-10}$$

where ρ_k is the solid density of reactant k (see **Table A4-1**), ε_{bed} is the reactor porosity 0.7.

For indirect R1, the endothermic reaction heat is provided by HTF,

$$Q_{R1,s} = (T_{HTFin} - T_{HTFout}) \cdot Cp_{HTF} \cdot Mw_{HTF} \cdot F_{HTFin,s} \quad s \in \mathbf{S} \tag{A4-11}$$

where T_{HTFin} and T_{HTFout} are HTF inlet and outlet temperatures at R1.

For indirect R2, the exothermic reaction heat is delivered to WF,

$$Q_{R2,s} = (T_{WFout} - T_{WFin}) \cdot Cp_{WF} \cdot Mw_{WF} \cdot F_{WFin,s} \quad s \in \mathbf{S} \tag{A4-12}$$

where T_{WFin} and T_{WFout} are WF inlet and outlet temperatures at R2.

In addition, we use constraints tailored to prevent the violation of the second law of thermodynamics during heat transfer between HTF-R1 (daytime) and R2-WF (nighttime),

$$T_{HTFin} - T_{R1} \geq \Delta T_{min} \tag{A4-13}$$

$$T_{HTFout} - T_{R2} \geq \Delta T_{min} \tag{A4-14}$$

$$T_{HTFout} - (T_{HTFin} - T_{HTFout}) \cdot \Delta H^{rxn} \cdot Mw_A \cdot F_{R1A,s}/Q_{R1,s} - T_{R1} \geq \Delta T_{min} \quad s \in \mathbf{S} \tag{A4-15}$$

$$T_{R1} - T_{WFout} \geq \Delta T_{min} \tag{A4-16}$$

$$T_{R2} - T_{WFin} \geq \Delta T_{min} \tag{A4-17}$$

$$T_{R2} - T_{WFin} - (T_{WFout} - T_{WFin}) \cdot \Delta H^{rxn} \cdot Mw_A \cdot F_{R2A,s}/Q_{R2,s} \geq \Delta T_{min} \quad s \in \mathbf{S} \tag{A4-18}$$

where the minimum approach temperature ΔT_{min} is 10 ℃ in this study.

A4.3 Process model of CSP with solid-gas TCES

In this section, we present the process model eqns (A4-1)-(A4-42) for CSP plants with solid-gas TCES systems in IR1-CON-OL configuration (see **Figure A4-1**).

Sets

$i \in \mathbf{I}$	Units
$j \in \mathbf{J}$	Streams
$k \in \{\mathrm{HTF}, \mathrm{WF}, \mathrm{A}, \mathrm{B}, \mathrm{C}\}$	Materials
$s \in \mathbf{S}$	Scenarios

Parameters

CRF	Capital recovery factor
Cp_k	Specific heat capacity
DNI_s	Solar direct normal irradiance
dP^{convey}	Conveyor unit power consumption
$f^{indirect}$	Indirect cost factor

f^{cont}	Contingency cost factor
ΔH^{rxn}	Reaction enthalpy
P^{rate}	CSP plant rated capacity
$Q^{r,ref}$	Reference size of receiver
T^{eq}	Reaction equilibrium temperature
ΔT_{min}	Minimum approach temperature during heat transfer
t_s^{day}	Duration of daytime in scenario *s*
t_s^{night}	Duration of nighttime in scenario *s*
β^r	Scaling factor of receiver
ε_{bed}	Bed porosity
ε_{tk}	Solid storage tank porosity
η^c	Collector efficiency
η^{bop}	Balance of plant efficiency (0.9, considering 10% parasitic load in the plant)
λ^c	Collector price
λ^{convey}	Conveyor price
λ^r	Receiver price at size $Q^{r,ref}$
λ^p	Power block price
λ^{hx}	Fixed bed reactor cost
λ^{sm}	Storage media price
$\lambda^{om,fix}$	Operation and maintenance, fixed cost
$\lambda^{om,vary}$	Operation and maintenance, variable cost
π_s	Occurrence frequency of scenario *s*
ρ_k	Density of material *k*

First stage variables

$AREA$	Heliostat (collector) area
$CAPEX$	Plant total capital cost
C^{convey}	Conveyor cost
C^{gas}	Reactant C gas storage cost
C^{TCES}	TCES system cost
$LCOE$	Levelized cost of electricity
m^{sm}	Storage media (A) weight
$OPEX$	Annual operational cost

Q^r	Receiver size
R_{R1}	Endothermic reaction rate
R_{R2}	Exothermic reaction rate
T_{R1}	Endothermic reaction temperature
T_{R2}	Exothermic reaction temperature
T_{HTF}^{in}	HTF inlet temperature at R1
T_{HTF}^{out}	HTF outlet temperature at R1
T_{WF}^{in}	WF inlet temperature at R2
T_{WF}^{out}	WF outlet temperature at R2
$V^{reactor}$	Reactor volume
W^{ele}	Annual Total electricity output
η^r	Receiver efficiency
$\eta^{p,day}/\eta^{p,night}$	Daytime/ nighttime power block efficiency

Second stage variables

$F_{j,s}$	Stream molar flowrate
W_s^{day}	Daytime power generated
W_s^{night}	Nighttime power generated
P_s^{convey}	Conveyor power
$Q_s^{curtail}$	Energy curtailed through heliostat defocus
$Q_{HTF,s}$	HTF thermal energy requirement during charging
t_s^c	Duration of daytime power generation (charging)
t_s^d	Duration of nighttime power generation (discharging)

Equations

Turbine efficiency day

$$\eta^{p,day} = -0.25\left(\frac{T_{HTFin} - \Delta T_{min}}{1000}\right)^2 + 0.87\left(\frac{T_{HTFin} - \Delta T_{min}}{1000}\right) - 0.15 \tag{A4-19}$$

Turbine efficiency night

$$\eta^{p,night} = -0.25\left(\frac{T_{WFout} - \Delta T_{min}}{1000}\right)^2 + 0.87\left(\frac{T_{WFout} - \Delta T_{min}}{1000}\right) - 0.15 \tag{A4-20}$$

Power cycle model	$T_{WFin} = 0.87 \cdot T_{WFout} - 98.3$	(A4-21)
Receiver efficiency	$\eta^r \ = 0.95 - [2.41\left(\frac{T_{HTFin}}{100}\right)^4 + \ 10(T_{HTFin} - 293)]/576000$	(A4-22)
Charging time	$t_s^c \leq t_s^{day} \ \ s \in \mathbf{S}$	(A4-23)
Discharging time	$t_s^d \leq t_s^{night} \ \ s \in \mathbf{S}$	(A4-24)
Mass balance tank A	$F_{R1A,s} \cdot t_s^c = F_{R2A,s} \cdot t_s^d \ \ s \in \mathbf{S}$	(A4-25)
Mass balance tank B	$F_{R1B,s} \cdot t_s^c = F_{R2B,s} \cdot t_s^d \ \ s \in \mathbf{S}$	(A4-26)
R2 heat duty	$Q_{R2,s} \cdot \eta^{p,night} \cdot \eta^{bop} = P^{rate} \ \ s \in \mathbf{S}$	(A4-27)
HTF heat duty	$Q_{HTF,s} = P^{rate}/\eta^p/\eta^{bop} + Q_{R1,s} \ \ s \in \mathbf{S}$	(A4-28)
Receiver size	$Q^r \cdot \eta^r \cdot t_s^{day} \geq Q_{HTF,s} \cdot t_s^c \ \ s \in \mathbf{S}$	(A4-29)
Plant energy balance	$AREA \cdot DNI_s \cdot \eta^c \cdot \eta^r \cdot t_s^{day} = Q_{HTF,s} \cdot t_s^c + Q_s^{curtail} \ s \in \mathbf{S}$	(A4-30)
Conveyor power	$P_s^{convey} = Mw_A \cdot F_{R1A,s} \cdot dP^{convey} \ \ s \in \mathbf{S}$	(A4-31)
Conveyor cost	$C^{convey} \geq \lambda^{convey} P_s^{convey} \ \ s \in \mathbf{S}$	(A4-32)
Tank A volume	$V^{tkA} \geq Mw_A \cdot F_{R1A,s}/\rho_A \ /(1 - \varepsilon_{tk}) \cdot t_s^c \ \ s \in \mathbf{S}$	(A4-33)
Tank B volume	$V^{tkB} \geq Mw_B \cdot F_{R1B,s}/\rho_B \ /(1 - \varepsilon_{tk}) \cdot t_s^c \ \ s \in \mathbf{S}$	(A4-34)
Storage media	$m^{sm} = Mw_A \cdot F_{R1A,s} \cdot t_s^c$	(A4-35)
TCES cost	$C^{TCES} = \lambda^{reactor} V^{reactor} + \lambda^{tk}(V^{tkA} + V^{tkB}) + C^{convey} + \lambda^{sm} m^{sm} + C^{gas} *$	(A4-36)

Capital cost

$$CAPEX = [\lambda^c \cdot AREA + \lambda^r \cdot Q^{r,ref} \cdot \left(\frac{Q^r}{Q^{r,ref}}\right)^{\beta^r} + C^{TCES} + \frac{\lambda^p \cdot P^{rate}}{\eta^{bop}}] \cdot (1 + f^{indirect}) \cdot (1 + f^{cont}) \tag{A4-37}$$

Operational cost

$$OPEX = \lambda^{om,fix} \cdot P^{rate} + \lambda^{om,vary} \cdot W_s^{ele} \tag{A4-38}$$

Total daytime power

$$W_s^{day} = (P^{rate} - P_s^{convey}) \cdot t_s^c \quad s \in \mathbf{S} \tag{A4-39}$$

Total nighttime power

$$W_s^{night} = P^{rate} \cdot t_s^d \quad s \in \mathbf{S} \tag{A4-40}$$

Annual power output

$$W^{ele} = 365 \sum_s \pi_s (W_s^{day} + W_s^{night}) \tag{A4-41}$$

Objective LCOE

$$LCOE = (CAPEX \cdot CRF + OPEX)/W^{ele} \tag{A4-42}$$

* For $\mathrm{Mn_2O_3}$ TCES, C^{gas} includes the cost of the sensible heat storage unit; For $\mathrm{Ca(OH)_2}$ TCES, C^{gas} includes the costs of the sensible heat storage unit and the water storage tank; For $\mathrm{CaCO_3}$ TCES, C^{gas} includes the costs of the sensible heat storage unit, the supercritical $\mathrm{CO_2}$ storage tank as well as the $\mathrm{CO_2}$ compressor and turbine.

Bibliography

1. World Energy Council. *Variable Renewables Integration In Electricity Systems: How To Get It Right*. *World Energy Perspectives* (2016).
2. Lewis, N. S. & Nocera, D. G. *Powering the planet: Chemical challenges in solar energy utilization*. (2006).
3. Henry, A. & Prasher, R. The prospect of high temperature solid state energy conversion to reduce the cost of concentrated solar power. *Energy Environ. Sci.* **7**, 1819 (2014).
4. Ghobeity, A. & Mitsos, A. Optimal Design and Operation of a Solar Energy Receiver and Storage. *J. Sol. Energy Eng.* **134**, 031005 (2012).
5. Feldman, D., Margolis, R., Denholm, P. & Stekli, J. *Exploring the Potential Competitiveness of Utility-Scale Photovoltaics plus Batteries with Concentrating Solar Power, 2015–2030*. (2016). doi:10.2172/1321487

6. Gençer, E. & Agrawal, R. Synthesis of efficient solar thermal power cycles for baseload power supply. *Energy Convers. Manag.* **133**, 486–497 (2017).
7. REN21. *Renewable 2018 global status report*. (2017).
8. IEA publications. *Energy Technology Perspectives 2017*. (2017). doi:10.1787/energy_tech-2017-en
9. Wood, T. & Blowers, D. *Sundown , sunrise How Australia can finally get solar power right*. (2015).
10. Weinstein, L. A. *et al.* Concentrating Solar Power. *Chem. Rev.* **115**, 12797–12838 (2015).
11. Stekli, J., Irwin, L. & Pitchumani, R. Technical Challenges and Opportunities for Concentrating Solar Power With Thermal Energy Storage. *J. Therm. Sci. Eng. Appl.* **5**, 021011 (2013).
12. Madaeni, S. H., Sioshansi, R. & Denholm, P. How Thermal Energy Storage Enhances the Economic Viability of Concentrating Solar Power. *Proc. IEEE* **100**, 335–347 (2012).
13. Feldman, D. *et al. Exploring the Potential Competitiveness of Utility-Scale Photovoltaics plus Batteries with Concentrating Solar Power , 2015 – 2030*. (2016).
14. Hinkely, J. *Trends in thermal storage (presented in 2016 SolarPACES). 2016 SolarPACES* (2016).
15. SolarReserve. *http://www.solarreserve.com/en/global-projects/csp/crescent-dunes (accessed Dec 11, 2016)*. (2016).
16. Nextera Energy. *Solar Electric Generating Systems*. (2016).
17. Mehos, M. *et al. Concentrating solar power: Gen3 demonstration roadmap*. (2017).
18. Wentworth, W. E. & Chen, E. Simple thermal decomposition reactions for storage of solar thermal energy. *Sol. Energy* **18**, 205–214 (1976).
19. Pardo, P. *et al.* A review on high temperature thermochemical heat energy storage. *Renew. Sustain. Energy Rev.* **32**, 591–610 (2014).
20. Garg, H. P., Mullick, S. C. & Bhargava, A. K. *Solar Thermal Energy Storage*. (Springer Netherlands, 1985). doi:10.1007/978-94-009-5301-7
21. Dunn, R., Lovegrove, K. & Burgess, G. A Review of Ammonia-Based Thermochemical Energy Storage for Concentrating Solar Power. *Proc. IEEE* **100**, 391–400 (2012).
22. Edwards, J. H. *et al.* The use of solar-based CO2/CH4 reforming for reducing greenhouse gas emissions during the generation of electricity and process heat. *Energy Convers. Manag.* **37**, 1339–1344 (1996).
23. Pan, Z. H. & Zhao, C. Y. Gas–solid thermochemical heat storage reactors for high-temperature applications. *Energy* **130**, 155–173 (2017).
24. André, L., Abanades, S. & Flamant, G. Screening of thermochemical systems based on solid-gas reversible reactions for high temperature solar thermal energy storage. *Renew. Sustain. Energy Rev.* **64**, 703–715 (2016).
25. Rhodes, N. R. *et al.* Solar Thermochemical Energy Storage Through Carbonation Cycles of

SrCO3/SrO Supported on SrZrO3. *ChemSusChem* **8**, 3793–3798 (2015).

26. Yu, F. C. & Fan, L. S. Kinetic study of high-pressure carbonation reaction of calcium-based sorbents in the calcium looping process (CLP). *Ind. Eng. Chem. Res.* **50**, 11528–11536 (2011).

27. Ortiz, C., Valverde, J. M., Chacartegui, R. & Perez-Maqueda, L. A. Carbonation of Limestone Derived CaO for Thermochemical Energy Storage: From Kinetics to Process Integration in Concentrating Solar Plants. *ACS Sustain. Chem. Eng.* **6**, 6404–6417 (2018).

28. Krohn, C. M. & Krohn, C. G. Development of porous solid reactant for thermal-energy storage and temperature upgrade using carbonation/decarbonation reaction. *Appl. Energy* **69**, 225–238 (2001).

29. Benitez-Guerrero, M., Valverde, J. M., Sanchez-Jimenez, P. E., Perejon, A. & Perez-Maqueda, L. A. Multicycle activity of natural CaCO3 minerals for thermochemical energy storage in Concentrated Solar Power plants. *Sol. Energy* **153**, 188–199 (2017).

30. Sánchez Jiménez, P. E. *et al.* High-performance and low-cost macroporous calcium oxide based materials for thermochemical energy storage in concentrated solar power plants. *Appl. Energy* **235**, 543–552 (2019).

31. Kato, Y., Yamada, M., Kanie, T. & Yoshizawa, Y. Calcium oxide/carbon dioxide reactivity in a packed bed reactor of a chemical heat pump for high-temperature gas reactors. *Nucl. Eng. Des.* **210**, 1–8 (2001).

32. Meier, A. *et al.* Design and experimental investigation of a horizontal rotary reactor for the solar thermal production of lime. *Energy* **29**, 811–821 (2004).

33. Abanades, S. & André, L. Design and demonstration of a high temperature solar-heated rotary tube reactor for continuous particles calcination. *Appl. Energy* **212**, 1310–1320 (2018).

34. Meier, A., Bonaldi, E., Cella, G. M., Lipinski, W. & Wuillemin, D. Solar chemical reactor technology for industrial production of lime. *Sol. Energy* **80**, 1355–1362 (2006).

35. Nikulshina, V., Gebald, C. & Steinfeld, A. CO2 capture from atmospheric air via consecutive CaO-carbonation and CaCO3-calcination cycles in a fluidized-bed solar reactor. *Chem. Eng. J.* **146**, 244–248 (2009).

36. Steinfeld, A., Imhof, A. & Mischler, D. Experimental Investigation of an Atmospheric-Open Cyclone Solar Reactor for Solid-Gas Thermochemical Reactions. *J. Sol. Energy Eng.* **114**, 171 (1992).

37. Imhof, A. The cyclone reactor — an atmospheric open solar reactor. *Sol. Energy Mater.* **24**, 733–741 (1991).

38. Ortiz, C., Romano, M. C., Valverde, J. M., Binotti, M. & Chacartegui, R. Process integration of Calcium-Looping thermochemical energy storage system in concentrating solar power plants. *Energy* **155**, 535–551 (2018).

39. Karasavvas, E., Panopoulos, K. D., Papadopoulou, S. & Voutetakis, S. Design of an integrated CSP-calcium looping for uninterrupted power production through energy storage. *Chem. Eng. Trans.* **70**, 2131–2136 (2018).

40. Edwards, S. E. B. & Materić, V. Calcium looping in solar power generation plants. *Sol. Energy* **86**, 2494–2503 (2012).

41. Ortiz, C., Valverde, J. M., Chacartegui, R., Perez-Maqueda, L. A. & Giménez, P. The Calcium-Looping (CaCO3/CaO) process for thermochemical energy storage in Concentrating Solar Power plants. *Renew. Sustain. Energy Rev.* **113**, 109252 (2019).

42. Bayon, A. *et al.* Techno-economic assessment of solid–gas thermochemical energy storage systems for solar thermal power applications. *Energy* **149**, 473–484 (2018).

43. Schaube, F., Koch, L., Wörner, A. & Müller-Steinhagen, H. A thermodynamic and kinetic study of the de- and rehydration of Ca(OH)2 at high H2O partial pressures for thermo-chemical heat storage. *Thermochim. Acta* **538**, 9–20 (2012).

44. Criado, Y. A., Alonso, M. & Abanades, J. C. Kinetics of the CaO/Ca(OH)2 hydration/dehydration reaction for thermochemical energy storage applications. *Ind. Eng. Chem. Res.* **53**, 12594–12601 (2014).

45. Roßkopf, C. *et al.* Investigations of nano coated calcium hydroxide cycled in a thermochemical heat storage. *Energy Convers. Manag.* **97**, 94–102 (2015).

46. Criado, Y. A., Alonso, M. & Abanades, J. C. Enhancement of a CaO/Ca(OH)2based material for thermochemical energy storage. *Sol. Energy* **135**, 800–809 (2016).

47. Kiyabu, S., Lowe, J. S., Ahmed, A. & Siegel, D. J. Computational Screening of Hydration Reactions for Thermal Energy Storage: New Materials and Design Rules. *Chem. Mater.* **30**, 2006–2017 (2018).

48. Schaube, F., Kohzer, A., Schütz, J., Wörner, A. & Müller-Steinhagen, H. De- and rehydration of Ca(OH)2 in a reactor with direct heat transfer for thermo-chemical heat storage. Part A: Experimental results. *Chem. Eng. Res. Des.* **91**, 856–864 (2013).

49. Schmidt, M., Gutierrez, A. & Linder, M. Thermochemical energy storage with CaO/Ca(OH)2– Experimental investigation of the thermal capability at low vapor pressures in a lab scale reactor. *Appl. Energy* **188**, 672–681 (2017).

50. Yan, J. & Zhao, C. Y. Experimental study of CaO/Ca(OH)2 in a fixed-bed reactor for thermochemical heat storage. *Appl. Energy* **175**, 277–284 (2016).

51. Ranjha, Q. & Oztekin, A. Numerical analyses of three-dimensional fixed reaction bed for thermochemical energy storage. *Renew. Energy* **111**, 825–835 (2017).

52. Schmidt, M., Gollsch, M., Giger, F., Grün, M. & Linder, M. Development of a moving bed pilot plant for thermochemical energy storage with CaO/Ca(OH)2. in *SolarPACES 2015* **050041**, 050041 (2016).

53. Rougé, S., Criado, Y. A., Soriano, O. & Abanades, J. C. Continuous CaO/Ca(OH)2 fluidized bed reactor for energy storage: First experimental results and reactor model validation. *Ind. Eng. Chem. Res.* **56**, 844–852 (2017).

54. Angerer, M. *et al.* Design of a MW-scale thermo-chemical energy storage reactor. *Energy Reports* **4**, 507–519 (2018).

55. Flegkas, S., Birkelbach, F., Winter, F., Freiberger, N. & Werner, A. Fluidized bed reactors for solid-gas thermochemical energy storage concepts - Modelling and process limitations.

Energy **143**, 615–623 (2018).

56. Pardo, P., Anxionnaz-Minvielle, Z., Rougé, S., Cognet, P. & Cabassud, M. Ca(OH)2/CaO reversible reaction in a fluidized bed reactor for thermochemical heat storage. *Sol. Energy* **107**, 605–616 (2014).

57. Pelay, U., Luo, L., Fan, Y., Stitou, D. & Castelain, C. Integration of a thermochemical energy storage system in a Rankine cycle driven by concentrating solar power: Energy and exergy analyses. *Energy* **167**, 498–510 (2019).

58. Schmidt, M. & Linder, M. Power generation based on the Ca(OH)2/ CaO thermochemical storage system – Experimental investigation of discharge operation modes in lab scale and corresponding conceptual process design. *Appl. Energy* **203**, 594–607 (2017).

59. Criado, Y. A., Alonso, M., Abanades, J. C. & Anxionnaz-Minvielle, Z. Conceptual process design of a CaO/Ca(OH) 2 thermochemical energy storage system using fluidized bed reactors. *Appl. Therm. Eng.* **73**, 1087–1094 (2014).

60. Brown, D. R., La Marche, J. L. & Spanner, G. E. Chemical Energy Storage System for Solar Electric Generating System (SEGS) Solar Thermal Power Plant. *J. Sol. Energy Eng.* **114**, 212 (1992).

61. Salas, D., Tapachès, E., Mazet, N. & Aussel, D. Economical optimization of thermochemical storage in concentrated solar power plants via pre-scenarios. *Energy Convers. Manag.* **174**, 932–954 (2018).

62. Fahim, M. A. & Ford, J. D. Energy storage using the BaO2-BaO reaction cycle. *Chem. Eng. J.* **27**, 21–28 (1983).

63. Agrafiotis, C., Roeb, M., Schmücker, M. & Sattler, C. Exploitation of thermochemical cycles based on solid oxide redox systems for thermochemical storage of solar heat. Part 1: Testing of cobalt oxide-based powders. *Sol. Energy* **102**, 189–211 (2014).

64. Babiniec, S. M., Coker, E. N., Miller, J. E. & Ambrosini, A. Investigation of La Sr1−Co M1−O3− (M = Mn, Fe) perovskite materials as thermochemical energy storage media. *Sol. Energy* **118**, 451–459 (2015).

65. Albrecht, K. J., Jackson, G. S. & Braun, R. J. Thermodynamically consistent modeling of redox-stable perovskite oxides for thermochemical energy conversion and storage. *Appl. Energy* **165**, 285–296 (2016).

66. Carrillo, A. J., Serrano, D. P., Pizarro, P. & Coronado, J. M. Thermochemical heat storage based on the Mn2O3/Mn3O4 redox couple: Influence of the initial particle size on the morphological evolution and cyclability. *J. Mater. Chem. A* **2**, 19435–19443 (2014).

67. Block, T., Knoblauch, N. & Schmücker, M. The cobalt-oxide/iron-oxide binary system for use as high temperature thermochemical energy storage material. *Thermochim. Acta* **577**, 25–32 (2014).

68. Preisner, N. C., Block, T., Linder, M. & Leion, H. Stabilizing Particles of Manganese-iron Oxide with Additives for Thermochemical Energy Storage. *Energy Technology* **6**, 2154–2165 (2018).

69. Wong, B. *Thermochemical Heat Storage for Concentrated Solar Power: Phase II Final*

Report. (2011).

70. Agrafiotis, C., Roeb, M., Schmücker, M. & Sattler, C. Exploitation of thermochemical cycles based on solid oxide redox systems for thermochemical storage of solar heat. Part 2: Redox oxide-coated porous ceramic structures as integrated thermochemical reactors/heat exchangers. *Sol. Energy* **114**, 440–458 (2015).

71. Karagiannakis, G., Pagkoura, C., Halevas, E., Baltzopoulou, P. & Konstandopoulos, A. G. Cobalt/cobaltous oxide based honeycombs for thermochemical heat storage in future concentrated solar power installations: Multi-cyclic assessment and semi-quantitative heat effects estimations. *Sol. Energy* **133**, 394–407 (2016).

72. Tescari, S. *et al.* Experimental evaluation of a pilot-scale thermochemical storage system for a concentrated solar power plant. *Appl. Energy* **189**, 66–75 (2017).

73. Neises, M. *et al.* Solar-heated rotary kiln for thermochemical energy storage. *Sol. Energy* **86**, 3040–3048 (2012).

74. Tescari, S. *et al.* Thermal model for the optimization of a solar rotary kiln to be used as high temperature thermochemical reactor. *Sol. Energy* **95**, 279–289 (2013).

75. Babiniec, S. M. *et al.* Considerations for the Design of a High-Temperature Particle Reoxidation Reactor for Extraction of Heat in Thermochemical Energy Storage Systems. in *Volume 1: Biofuels, Hydrogen, Syngas, and Alternate Fuels; CHP and Hybrid Power and Energy Systems; Concentrating Solar Power; Energy Storage; Environmental, Economic, and Policy Considerations of Advanced Energy Systems; Geothermal, Ocean, and Emerging E* V001T04A021 (ASME, 2016). doi:10.1115/ES2016-59646

76. Albrecht, K. J., Jackson, G. S. & Braun, R. J. Evaluating thermodynamic performance limits of thermochemical energy storage subsystems using reactive perovskite oxide particles for concentrating solar power. *Sol. Energy* **167**, 179–193 (2018).

77. Muroyama, A. P., Schrader, A. J. & Loutzenhiser, P. G. Solar electricity via an Air Brayton cycle with an integrated two-step thermochemical cycle for heat storage based on Co3O4/CoO redox reactions II: Kinetic analyses. *Sol. Energy* **122**, 409–418 (2015).

78. Miller, J. E. *et al.* High Performance Reduction/Oxidation Metal Oxides for Thermochemical Energy Storage (PROMOTES). in *Volume 1: Biofuels, Hydrogen, Syngas, and Alternate Fuels; CHP and Hybrid Power and Energy Systems; Concentrating Solar Power; Energy Storage; Environmental, Economic, and Policy Considerations of Advanced Energy Systems; Geothermal, Ocean, and Emerging E* V001T04A024 (ASME, 2016). doi:10.1115/ES2016-59660

79. Olajire, A. A. A review of mineral carbonation technology in sequestration of CO2. *J. Pet. Sci. Eng.* **109**, 364–392 (2013).

80. Hanak, D. P., Biliyok, C. & Manovic, V. Calcium looping with inherent energy storage for decarbonisation of coal-fired power plant. *Energy Environ. Sci.* **9**, 971–983 (2016).

81. Criado, Y. A., Arias, B. & Abanades, J. C. Calcium looping CO2 capture system for back-up power plants. *Energy Environ. Sci.* **10**, 1994–2004 (2017).

82. Edwards, J. H. *et al.* The use of solar-based CO2/CH4 reforming for reducing greenhouse gas emissions during the generation of electricity and process heat. *Energy Convers. Manag.*

37, 1339–1344 (1996).

83. Rhodes, N. R. *et al.* Solar Thermochemical Energy Storage Through Carbonation Cycles of SrCO3/SrO Supported on SrZrO3. *ChemSusChem* **8**, 3793–3798 (2015).

84. Pardo, P. *et al.* A review on high temperature thermochemical heat energy storage. *Renew. Sustain. Energy Rev.* **32**, 591–610 (2014).

85. Alonso, E. & Romero, M. Review of experimental investigation on directly irradiated particles solar reactors. *Renew. Sustain. Energy Rev.* **41**, 53–67 (2015).

86. Pan, Z. H. & Zhao, C. Y. Gas–solid thermochemical heat storage reactors for high-temperature applications. *Energy* **130**, 155–173 (2017).

87. Schaube, F., Wörner, A. & Tamme, R. High Temperature Thermochemical Heat Storage for Concentrated Solar Power Using Gas–Solid Reactions. *J. Sol. Energy Eng.* **133**, 031006 (2011).

88. Zsembinszki, G. *et al.* Review of Reactors with Potential Use in Thermochemical Energy Storage in Concentrated Solar Power Plants. *Energies* **11**, 2358 (2018).

89. Turchi, C. S. & Heath, G. A. *Molten Salt Power Tower Cost Model for the System Advisor Model (SAM)*. (2013).

90. Henao, C. A. & Maravelias, C. T. Surrogate-based superstructure optimization framework. *AIChE J.* **57**, 1216–1232 (2011).

91. Apt, J., Newcomer, A., Lave, L. B., Douglas, S. & Dunn, L. M. *An Engineering-Economic Analysis of Syngas Storage*. *U.S. Department of Energy's National Energy Technology Laboratory* (2008).

92. Amos, W. A. *Costs of storing and transporting hydrogen*. (1998).

93. Federal energy regulatory commission. *Current state of and issues concerning underground natural gas storage*. (2004). doi:AD04-11-000

94. Lord, A. S., Kobos, P. H., Klise, G. T. & Borns, D. J. *A Life Cycle Cost Analysis Framework for Geological Storage of Hydrogen: A User's Tool*. *Analysis* (2011). doi:SAND2011-6221

95. U.S. Department of Energy. *SunShot Vision Study*. (2012).

96. Ho, C. K. & Iverson, B. D. Review of high-temperature central receiver designs for concentrating solar power. *Renew. Sustain. Energy Rev.* **29**, 835–846 (2014).

97. Grossmann, I. E., Halemane, K. P. & Swaney, R. E. Optimization strategies for flexible chemical processes. *Comput. Chem. Eng.* **7**, 439–462 (1983).

98. Floudas, C. A. & Grossmann, I. E. Synthesis of flexible heat exchanger networks with uncertain flowrates and temperatures. *Comput. Chem. Eng.* **11**, 319–336 (1987).

99. Papalexandri, K. P. & Pistikopoulos, E. N. Synthesis and Retrofit Design of Operable Heat Exchanger Networks. 1. Flexibility and Structural Controllability Aspects. *Ind. Eng. Chem. Res.* **33**, 1718–1737 (1994).

100. Paules IV, G. E. & Floudas, C. A. Synthesis of flexible distillation sequences for multiperiod operation. *Comput. Chem. Eng.* **12**, 267–280 (1988).

101. Paules, G. E. & Floudas, C. A. Stochastic programming in process synthesis: A two-stage model with MINLP recourse for multiperiod heat-integrated distillation sequences. *Comput. Chem. Eng.* **16**, 189–210 (1992).

102. Fazlollahi, S., Becker, G. & Maréchal, F. O. Multi-objectives, multi-period optimization of district energy systems: II—Daily thermal storage. *Comput. Chem. Eng.* **71**, 648–662 (2014).

103. Iyer, R. R. & Grossmann, I. E. Synthesis and operational planning of utility systems for multiperiod operation. *Comput. Chem. Eng.* **22**, 979–993 (1998).

104. Sabev Varbanov, P. *et al.* Design of Integrated Solar Thermal Energy System for Multi-Period Process Heat Demand. *Chem. Eng. Trans.* **52**, (2016).

105. Chen, Y., Adams, T. A. & Barton, P. I. Optimal Design and Operation of Flexible Energy Polygeneration Systems. *Ind. Eng. Chem. Res.* **50**, 4553–4566 (2011).

106. Aviso, K. B. *et al.* A P-graph model for multi-period optimization of sustainable energy systems. *J. Clean. Prod.* **161**, 1338–1351 (2017).

107. Heckl, I., Halász, L., Szlama, A., Cabezas, H. & Friedler, F. Process synthesis involving multi-period operations by the P-graph framework. *Comput. Chem. Eng.* **83**, 157–164 (2015).

108. Rooney, W. C. & Biegler, L. T. Optimal process design with model parameter uncertainty and process variability. *AIChE J.* **49**, 438–449 (2003).

109. Martín, M. Methodology for solar and wind energy chemical storage facilities design under uncertainty: Methanol production from CO2and hydrogen. *Comput. Chem. Eng.* **92**, 43–54 (2016).

110. Petruschke, P. *et al.* A hybrid approach for the efficient synthesis of renewable energy systems. *Appl. Energy* **135**, 625–633 (2014).

111. Slocum, A. H. *et al.* Concentrated solar power on demand. *Sol. Energy* **85**, 1519–1529 (2011).

112. Agrawal, R. & Mallapragada, D. S. Chemical engineering in a solar energy-driven sustainable future. *AIChE J.* **56**, 2762–2768 (2010).

113. Tora, E. A. & El-Halwagi, M. M. Optimal design and integration of solar systems and fossil fuels for sustainable and stable power outlet. *Clean Technol. Environ. Policy* **11**, 401–407 (2009).

114. Rudd, D. F., Powers, G. J. & Siirola, J. J. *Process synthesis*. (Prentice-Hall, 1973).

115. Nishida, N., Stephanopoulos, G. & Westerberg, A. W. A review of process synthesis. *AIChE J.* **27**, 321–351 (1981).

116. Westerberg, A. W. A retrospective on design and process synthesis. *Comput. Chem. Eng.* **28**, 447–458 (2004).

117. Furman, K. C. & Sahinidis, N. V. Computational complexity of heat exchanger network synthesis. *Comput. Chem. Eng.* **25**, 1371–1390 (2001).

118. Morar, M. & Agachi, P. S. Review: Important contributions in development and

improvement of the heat integration techniques. *Comput. Chem. Eng.* **34**, 1171–1179 (2010).

119. Klemeš, J. J. & Kravanja, Z. Forty years of Heat Integration: Pinch Analysis (PA) and Mathematical Programming (MP). *Curr. Opin. Chem. Eng.* **2**, 461–474 (2013).

120. Skiborowski, M., Harwardt, A. & Marquardt, W. Conceptual Design of Distillation-Based Hybrid Separation Processes. *Annu. Rev. Chem. Biomol. Eng.* **4**, 45–68 (2013).

121. Cremaschi, S. A perspective on process synthesis: Challenges and prospects. *Comput. Chem. Eng.* **81**, 130–137 (2015).

122. Feinberg, M. Toward a Theory of Process Synthesis. *Ind. Eng. Chem. Res.* **41**, 3751–3761 (2002).

123. Jeżowski, J. Review of Water Network Design Methods with Literature Annotations. *Ind. Eng. Chem. Res.* **49**, 4475–4516 (2010).

124. Biegler, L. T., Grossmann, I. E. & Westerberg, A. W. *Systematic methods for chemical process design*. (Prentice Hall, Old Tappan, NJ (United States), 1997).

125. Kocis, G. R. & Grossmann, I. E. A modelling and decomposition strategy for the minlp optimization of process flowsheets. *Comput. Chem. Eng.* **13**, 797–819 (1989).

126. Friedler, F., Tarján, K., Huang, Y. W. & Fan, L. T. Graph-theoretic approach to process synthesis: axioms and theorems. *Chem. Eng. Sci.* **47**, 1973–1988 (1992).

127. Wu, W., Henao, C. A. & Maravelias, C. T. A superstructure representation, generation, and modeling framework for chemical process synthesis. *AIChE J.* **62**, 3199–3214 (2016).

128. Henao, C. A. & Maravelias, C. T. Surrogate-based superstructure optimization framework. *AIChE J.* **57**, 1216–1232 (2011).

129. Kravanja, Z. & Grossmann, I. E. Multilevel-hierarchical MINLP synthesis of process flowsheets. *Comput. Chem. Eng.* **21**, S421–S426 (1997).

130. Daichendt, M. M. & Grossmann, I. E. Integration of hierarchical decomposition and mathematical programming for the synthesis of process flowsheets. *Comput. Chem. Eng.* **22**, 147–175 (1998).

131. Bedenik, N. I., Pahor, B. & Kravanja, Z. An integrated strategy for the hierarchical multilevel MINLP synthesis of overall process flowsheets using the combined synthesis/analysis approach. in *Computers and Chemical Engineering* **28**, 693–706 (2004).

132. Swaney, R. E. & Grossmann, I. E. An Index for Operational Flexibility in Chemical Process Design. Part 2: Computational Algorithms. *AIChE J.* **31**, 631–641 (1985).

133. Pistikopoulos, E. N. & Grossmann, I. E. Optimal retrofit design for improving process flexibility in nonlinear systems-II. Optimal level of flexibility. *Comput. Chem. Eng.* **13**, 1087–1096 (1989).

134. Pistikopoulos, E. N. & Ierapetritou, M. G. Novel approach for optimal process design under uncertainty. *Comput. Chem. Eng.* **19**, 1089–1110 (1995).

135. Bansal, V., Perkins, J. D. & Pistikopoulos, E. N. Flexibility analysis and design of dynamic processes with stochastic parameters. *Comput. Chem. Eng.* **22**, S817–S820 (1998).

136. Floudas, C. A., Gümüş, Z. H. & Ierapetritou, M. G. Global optimization in design under

uncertainty: Feasibility test and flexibility index problems. *Ind. Eng. Chem. Res.* **40**, 4267–4282 (2001).

137. Sahinidis, N. V. Optimization under uncertainty: State-of-the-art and opportunities. *Comput. Chem. Eng.* **28**, 971–983 (2004).
138. Acevedot, J. & Pistikopoulos, E. N. Stochastic optimization based algorithms for process synthesis under uncertainty. *Comput. chem. Engng* **22**, 647–671 (1998).
139. Ahmed, S., King, A. J. & Parija, G. A Multi-Stage Stochastic Integer Programming Approach for Capacity Expansion under Uncertainty. *J. Glob. Optim.* **26**, 3–24 (2003).
140. Subrahmanyam, S., Pekny, J. F. & Reklaitiso, G. V. Design of Batch Chemical Plants under Market Uncertainty. *Znd. Eng. Chem. Res* **33**, 2688–2701 (1994).
141. Suh, M. & Lee, T. Robust Optimization Method for the Economic Term in Chemical Process Design and Planning. *Ind. Eng. Chem. Res.* **40**, 5950–5959 (2001).
142. Kasivisvanathan, H., Ubando, A. T., Ng, D. K. S. & Tan, R. R. Robust Optimization for Process Synthesis and Design of Multifunctional Energy Systems with Uncertainties. *Ind. Eng. Chem. Res.* **53**, 3196–3209 (2014).
143. Tay, D. H. S., Ng, D. K. S. & Tan, R. R. Robust optimization approach for synthesis of integrated biorefineries with supply and demand uncertainties. *Environ. Prog. Sustain. Energy* **32**, 384–389 (2013).
144. Ning, C. & You, F. Data-driven adaptive nested robust optimization: General modeling framework and efficient computational algorithm for decision making under uncertainty. *AIChE J.* **63**, 3790–3817 (2017).
145. Birge, J. R. & Louveaux, F. *Introduction to Stochastic Programming*. (Springer New York, 2011). doi:10.1007/978-1-4614-0237-4
146. Begg, S. H., Welsh, M. B. & Bratvold, R. B. Uncertainty vs. Variability: What’s the Difference and Why is it Important? *SPE Hydrocarb. Econ. Eval. Symp.* 19–20 (2014). doi:10.2118/169850-MS
147. Tawarmalani, M. & Sahinidis, N. V. A polyhedral branch-and-cut approach to global optimization. *Math. Program.* **103**, 225–249 (2005).
148. Achterberg, T. SCIP: solving constraint integer programs. *Math. Program. Comput.* **1**, 1–41 (2009).
149. Misener, R. & Floudas, C. A. ANTIGONE: Algorithms for coNTinuous / Integer Global Optimization of Nonlinear Equations. *J. Glob. Optim.* **59**, 503–526 (2014).
150. Floudas, C. A. & Gounaris, C. E. A review of recent advances in global optimization. *J Glob Optim* **45**, 3–38 (2009).
151. Pardalos, P. M., Romeijn, H. E. & Tuy, H. Recent developments and trends in global optimization. *J. Comput. Appl. Math.* **124**, 209–228 (2000).
152. Puranik, Y. & Sahinidis, N. V. Domain reduction techniques for global NLP and MINLP optimization. *Constraints* **22**, 338–376 (2017).
153. Velez, S., Sundaramoorthy, A. & Maravelias, C. T. Valid Inequalities Based on Demand

Propagation for Chemical Production Scheduling MIP Models. *AIChE J.* **59**, 872–887 (2013).

154. Merchan, A. F. & Maravelias, C. T. Preprocessing and tightening methods for time-indexed MIP chemical production scheduling models. *Comput. Chem. Eng.* **84**, 516–535 (2016).
155. Kong, L., Sen, S. M., Henao, C. A., Dumesic, J. A. & Maravelias, C. T. A superstructure-based framework for simultaneous process synthesis, heat integration, and utility plant design. *Comput. Chem. Eng.* **91**, 68–84 (2016).
156. Ruszczyfiski, A. Decomposition methods in stochastic programming. *Math. Program.* **79**, 333–353 (1997).
157. Wets, R. Stochastic programming: solution techniques and approximation. *Math. Program. state art (Bonn, 1982)* **2**, 566–603 (1983).
158. Fisher, M. L. The Lagrangian Relaxation Method for Solving Integer Programming Problems. *Manage. Sci.* **27**, 1–18 (1981).
159. Carøe, C. C. & Schultz, R. Dual decomposition in stochastic integer programming. *Oper. Res. Lett.* **24**, 37–45 (1999).
160. Van Slyke, R. M. & Wets, R. L -Shaped Linear Programs with Applications to Optimal Control and Stochastic Programming. *SIAM J. Appl. Math.* **17**, 638–663 (1969).
161. Geoffrion, A. M. Generalized Benders decomposition. *J. Optim. Theory Appl.* **10**, 237–260 (1972).
162. Li, X., Tomasgard, A. & Barton, P. I. Nonconvex Generalized Benders Decomposition for Stochastic Separable Mixed-Integer Nonlinear Programs. *J. Optim. Theory Appl.* **151**, 425–454 (2011).
163. Birge, J. R. Decomposition and Partitioning Methods for Multistage Stochastic Linear Programs. *Oper. Res.* **33**, 989–1007 (1985).
164. von Storch, H. & Zwiers, F. W. *Statistical Analysis in Climate Research*. (Cambridge: Cambridge University Press, 2003).
165. Brockwell, P. J. & Davis, R. A. *Time Series: Theory and Methods*. (Springer Science \& Business Media, 1991). doi:10.1007/978-1-4419-0320-4
166. Jenkins, G. M. & Watts, D. G. *Spectral Analysis and Its Applications*. *Spectral Analysis and Its Applications (San Francisco: Holden-Day)* (Holden-Day, 1968).
167. Koopmans, L. H. Digital Filters. in *The Spectral Analysis of Time Series* 165–209 (Academic Press, 1995). doi:10.1016/B978-012419251-5/50008-9
168. Peng, X., Root, T. W. & Maravelias, C. T. Storing Solar Energy with Chemistry: The Role of Thermochemical Storage in Concentrating Solar Power. *Green Chem.* 2427–2438 (2017). doi:10.1039/C7GC00023E
169. National Renewable Energy Laboratory. National Solar Radiation Data Base. (2017). Available at: http://rredc.nrel.gov/solar/old_data/nsrdb/. (Accessed: 26th November 2017)
170. Wagner, M. J. Simulation and Predictive Performance Modeling of Utility-Scale Central Receiver System Power Plants by. (University of Wisconsin-Madison, 2008).

171. Montes, M. J., Abánades, A., Martínez-Val, J. M. & Valdés, M. Solar multiple optimization for a solar-only thermal power plant, using oil as heat transfer fluid in the parabolic trough collectors. *Sol. Energy* **83**, 2165–2176 (2009).

172. Burgaleta, J. I., Ternero, A., Vindel, D., Salbidegoitia, I. & Azcarrraga, G. Gemasolar, key points for the operation of the plant. in *Proceedings of SolarPACES* 1–11 (2012).

173. National Renewable Energy Laboratory. System Advisor Model Version 2017.9.5. (2017).

174. Linder, M., Roßkopf, C., Schmidt, M. & Wörner, A. Thermochemical Energy Storage in kW-scale based on CaO/Ca(OH)2. *Energy Procedia* **49**, 888–897 (2014).

175. Angerer, M. *et al.* Design of a MW-scale thermo-chemical energy storage reactor. *Energy Reports* **4**, 507–519 (2018).

176. Wheeler, V. M. *et al.* Modelling of solar thermochemical reaction systems. (2017). doi:10.1016/j.solener.2017.07.069

177. Ströhle, S., Haselbacher, A., Jovanovic, Z. R. & Steinfeld, A. The effect of the gas-solid contacting pattern in a high-temperature thermochemical energy storage on the performance of a concentrated solar power plant. *Energy Environ. Sci.* **9**, 1375–1389 (2016).

178. Lei, Q., Bader, R., Kreider, P., Lovegrove, K. & Lipiński, W. Thermodynamic analysis of a combined-cycle solar thermal power plant with manganese oxide-based thermochemical energy storage. in *E3S Web of Conferences* (eds. Kaźmierczak, B., Kutyłowska, M., Piekarska, K., Jouhara, H. & Danielewicz, J.) **22**, 00102 (EDP Sciences, 2017).

179. Alovisio, A., Chacartegui, R., Ortiz, C., Valverde, J. M. & Verda, V. Optimizing the CSP-Calcium Looping integration for Thermochemical Energy Storage. *Energy Convers. Manag.* **136**, 85–98 (2017).

180. Chacartegui, R. *et al.* Thermochemical energy storage of concentrated solar power by integration of the calcium looping process and a CO2 power cycle. *Appl. Energy* **173**, 589–605 (2016).

181. Tapachès, E. *et al.* The value of thermochemical storage for concentrated solar power plants: Economic and technical conditions of power plants profitability on spot markets. (2018). doi:10.1016/j.enconman.2018.11.082

182. Binotti, M., Astolfi, M., Campanari, S., Manzolini, G. & Silva, P. Preliminary assessment of sCO2 cycles for power generation in CSP solar tower plants. *Appl. Energy* **204**, 1007–1017 (2017).

183. Ho, C. K., Carlson, M., Garg, P. & Kumar, P. Technoeconomic Analysis of Alternative Solarized s-CO 2 Brayton Cycle Configurations. *J. Sol. Energy Eng.* **138**, 051008 (2016).

184. Neises, T. & Turchi, C. Supercritical carbon dioxide power cycle design and configuration optimization to minimize levelized cost of energy of molten salt power towers operating at 650 °C. *Sol. Energy* **181**, 27–36 (2019).

185. Nakaso, K., Aoki, T. & Fukai, J. Effects of Fin Configuration on Heat Transfer Rate in Packed Bed Reactors for Improvement of Their Thermal Characteristics. in 975–981 (2011). doi:10.1115/ihtc14-23175

186. Schmidt, P., Bouché, M., Linder, M. & Wörner, A. Pilot Plant Development of High

Temperature Thermochemical Heat Storage. in (2012).

187. Schmidt, M., Szczukowski, C., Roßkopf, C., Linder, M. & Wörner, A. Experimental results of a 10 kW high temperature thermochemical storage reactor based on calcium hydroxide. *Appl. Therm. Eng.* **62**, 553–559 (2014).

188. Kee, R. J. *et al.* The design, fabrication, and evaluation of a ceramic counter-flow microchannel heat exchanger. *Appl. Therm. Eng.* **31**, 2004–2012 (2011).

189. McDonald, C. F. Recuperator considerations for future higher efficiency microturbines. *Appl. Therm. Eng.* **23**, 1463–1487 (2003).

190. Shao, H. *et al.* Non-equilibrium thermo-chemical heat storage in porous media: Part 2 – A 1D computational model for a calcium hydroxide reaction system. *Energy* **60**, 271–282 (2013).

191. Li, Z.-S. & Cai, N.-S. Modeling of Multiple Cycles for Sorption-Enhanced Steam Methane Reforming and Sorbent Regeneration in Fixed Bed Reactor. (2007). doi:10.1021/ef070112c

192. Fan, F., Li, Z. S. & Cai, N. S. Experiment and modeling of CO2 capture from flue gses at high temperature in a fluidized bed reactor with ca-based sorbents. *Energy and Fuels* **23**, 207–216 (2009).

193. Sanchez, F., Budinger, M. & Hazyuk, I. Dimensional analysis and surrogate models for the thermal modeling of Multiphysics systems. *Appl. Therm. Eng.* **110**, 758–771 (2017).

194. National Renewable Energy Laboratory. National Solar Radiation Data Base. Available at: http://rredc.nrel.gov/solar/old_data/nsrdb/1961-1990/. (Accessed: 29th August 2017)

195. Peng, X., Root, T. W. & Maravelias, C. T. Storing solar energy with chemistry: the role of thermochemical storage in concentrating solar power. *Green Chem.* **19**, 2427–2438 (2017).

196. Peng, X., Root, T. W. & Maravelias, C. T. Optimization-based Process Synthesis under Seasonal and Daily Variability: Application to Concentrating Solar Power. *AIChE J.* **00**, 1–16 (2018).

197. Sahinidis, N. V. BARON user manual v. 17.8.9. (2017). Available at: http://www.minlp.com/downloads/docs/baron manual.pdf. (Accessed: 23rd August 2017)

198. Dowling, A. W., Zheng, T. & Zavala, V. M. Economic assessment of concentrated solar power technologies: A review. *Renew. Sustain. Energy Rev.* **72**, 1019–1032 (2017).

199. Deutsch, M. *et al.* Systematic search algorithm for potential thermochemical energy storage systems. *Appl. Energy* **183**, 113–120 (2016).

200. Lord, A. S. *Overview of geologic storage of natural gas with an emphasis on assessing the feasibility of storing hydrogen.* (2009). doi:10.2172/975258

201. Co-Firing EPA-Outlawed Coal Power Plants with Carbon Capture. (2016). Available at: http://stoppingclimatechange.com/co-firing.htm. (Accessed: 29th December 2016)